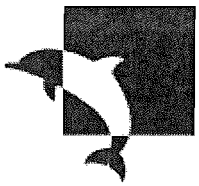

University of Southampton

VIBRATION OF STRUCTURES MADE OF CELLULAR MATERIAL

Sourish Banerjee

A thesis submitted for the partial fulfillment of

Doctor of Philosophy

in the

Faculty of Engineering and Applied Science

School of Engineering Sciences

November, 2004

UNIVERSITY OF SOUTHAMPTON

ABSTRACT

FACULTY OF ENGINEERING AND APPLIED SCIENCE
SCHOOL OF ENGINEERING SCIENCES

DOCTOR OF PHILOSOPHY

VIBRATION OF STRUCTURES MADE OF CELLULAR MATERIAL

BY SOURISH BANERJEE

The main objective of this dissertation is to study the dynamics of structures made of cellular material. The validity of the effective medium theories is examined numerically when applied to statics and dynamics of beams. It is found that structures made of cellular material do approximately behave as continua for low mode numbers.

The vibration frequencies of beams made of a variety of microstructures are computed numerically and the change in modal spacing is studied systematically. To compare and contrast the situation with that of continuum, a problem of porosity filled solid with the same external dimensions as those of the cellular beam is undertaken. With the increase in the mode number, a progressive departure in the trend is observed. This trend for cellular beams is strongly dependent on the microstructure and is a result of various types of local resonances in the cell walls.

A method to reduce the computation involved in the vibration calculations in cellular structures is proposed. Continuum-based assumed modes are used as the basis of the method. It is found that a direct use of the assumed modes in the approximation yields inaccurate results. The source of this error is identified. A sensitivity analysis is presented to show that the small components of modal contribution associated with the exceptionally high frequency modes are responsible for the poor performance of the assumed modes method. The method is improved by pre-conditioning the assumed modes by the use of inverse power iterations. Two examples, a cantilever beam and an L-beam, are presented to demonstrate the working of the method. Further, a reduced order model is developed to estimate the frequency response. The effect of damping is included in the response calculations. The proposed method is shown to result in substantial computation saving for free vibration as well as forced response calculations while the accuracy is not compromised seriously.

The effective elastic modulii of metal foam are experimentally determined. The hypothesis of the effective medium theory is then tested by a mode by mode comparison of the effective Young's modulus with that of a continuum.

The general conclusion that cellular solids cease to behave as continua at moderately high mode numbers may have important implications to the dynamics of structures made of such material at high frequencies.

कर्मण्येवाधिकारस्ते मा फलेषु कदाचन।
मा कर्मफलहेतुर्भूर्मा ते सङ्गोऽस्त्वकर्मणि॥

Thy right is to work only
But never its fruits
Let not the fruit of action be thy motive
Nor let the attachment be to inaction.

— Sloka from Bhagavad Gita

Education is the manifestation of the perfection already in man.

— Swami Vivekananda

Contents

Abstract ii

List of Figures vii

List of Tables xv

Declaration of Authorship xvii

Acknowledgments xviii

Nomenclature xix

Chapter 1 Introduction 1

§1.1 Background 1

§1.2 Review of the past works 1

§1.2.1 In-plane behaviour of two dimensional cellular materials 2

§1.2.2 Out-of-plane behaviour of cellular materials 9

§1.2.3 Mechanical behaviour of three dimensional cellular materials . . . 10

§1.2.4 Effects of imperfections in cellular materials 14

§1.2.5 Nonlinear Elastic Behaviour 15

§1.2.6 Dynamics of cellular materials 16

§1.3 Objectives and scope of the present work 16

§1.4 Outline of this dissertation 17

Chapter 2 Applicability of the effective medium theory to statics and dynamics of cellular beams 19

§2.1 Introduction 19

§2.2 Calculation of response of cellular structures using the finite element method 20

§2.2.1 Free vibration calculations for cellular structures 21
§2.3 Effective elasticity of hexagonal and triangular lattices 22
§2.4 Results and discussions 27
§2.4.1 Transverse bending of beams having regular hexagonal cells 28
§2.4.2 Energy distribution 31
§2.4.3 Statics of beams made of hexagonal cells exhibiting orthotropy . . 33
§2.4.4 Static deflection of cellular beams having triangular cells 33
§2.4.5 Free vibration of beams made of regular hexagonal cells 35
§2.4.6 Vibration of hexagonal cells exhibiting overall orthotropy 43
§2.4.7 Vibration of beams made of triangular cells 47
§2.4.8 A method for approximately calculating the fundamental frequency 47
§2.5 Conclusions 49

Chapter 3 Statistical analysis of modal spacing and progressive departure from the continuum behaviour **51**
§3.1 Introduction 51
§3.2 Numerical experiments using the finite element method 52
§3.3 Results and discussions 53
§3.3.1 Modal distribution for beams made of triangular cells 53
§3.3.2 Modal distribution for beams made of square cells 59
§3.3.3 Modal distribution for beams made of hexagonal cells 62
§3.3.4 Modal distribution for beams made of irregular cells 65
§3.4 Conclusions 71

Chapter 4 Efficient free vibration calculations of cellular structures using continuum modes **73**
§4.1 Introduction 73
§4.2 The proposed approximation for cellular structures based on continuum modes 75
§4.3 Rayleigh's variational method and pre-conditioning of the trial modes . . 78
§4.4 Numerical examples and discussions 81
§4.4.1 Example 1: the cantilever beam 82
§4.4.2 Example 2: the L-beam 86
§4.5 Conclusions 93

Chapter 5 Frequency response calculations of cellular structures using continuum modes **94**

§5.1 Introduction 94

§5.2 Development of the reduced order model using the continuum modes . . . 95

§5.2.1 Proportional Damping 98

§5.3 A numerical example and discussions 99

§5.3.1 Undamped response 99

§5.3.2 Damped response 104

§5.4 Conclusions 107

Chapter 6 Experimental determination of the effective modulii of metallic foams and their dependence on mode number **110**

§6.1 Introduction 110

§6.2 The experimental procedure 111

§6.3 Results and discussions 114

§6.3.1 Extraction of elastic modulii from experimentally measured natural frequency data 117

§6.3.2 Degradation of the effective elastic modulii of metallic foams with mode number 123

§6.4 Conclusions 127

Chapter 7 Conclusions and future work **130**

§7.1 Concluding remarks 130

§7.2 Future work 133

List of Figures

1.1 Periodic structures made of hexagonal, inverted hexagonal, triangular and square cells. 3

1.2 Geometry of a hexagonal cell in two different orientations. The parameters h, l, θ and t are shown. 4

1.3 Schematic of irregular structure of a planar honeycomb. Note the absence of any periodicity. 7

2.1 Two length scales of the structures made of cells. The length scale l_c is associated with the average cell size and, the length, l_s, is associated with the overall dimensions. 23

2.2 A lattice of regular hexagons. The length of the beam runs horizontally whereas the thickness runs vertically. This geometry is referred to as orientation 1 in the text. 25

2.3 Another orientations of the hexagons in the lattice– orientation 2. Note that the hexagons are rotated by a right angle with respect to the orientation shown in figure 2.2. The length of the beam runs horizontally as before. 25

2.4 A beam made of equilateral triangles. Henceforth, this orientation is referred to as orientation 1. 27

2.5 Another beam made of equilateral triangles, with the triangles are now oriented at a right angle with respect to the previous orientation. This orientation is referred to as orientation 2 in the text. 27

2.6 The displacement field of a cellular cantilever beam due to a vertical load acting at the free end. The deflected configuration resembles to that of a homogeneous beam. 30

2.7 The displacement field of a cellular rod subjected to a tensile force at the free end. 30
2.8 Distribution of the bending strain energy among the cell walls due to transverse bending of a cantilever beam subjected to tip load. The beam is made of regular hexagonal cells having orientation 1. The bending energy accounts for 99.99% of the total strain energy. 32
2.9 The displacement field of a cantilever beam made of triangles when a vertical load acts at the free end. The deflected configuration resembles to that of a homogeneous beam. 35
2.10 The first mode of vibration of the beam made of regular hexagonal cells. Note the resemblance in the displacement pattern with those commonly found in fixed-free continuum beams. 36
2.11 The second mode of vibration. Note the existence of a 'node' roughly where a node for a beam made up of continuum would be found. 37
2.12 The third mode of vibration. Again this mode resembles the third continuum mode of a beam. There are two 'nodes' at the macroscopic level. . 37
2.13 The fourth mode of vibration. This mode, unlike the previous three as in figures 2.10 through to 2.12, shows axial mode of vibration at the macroscopic level. 38
2.14 The fifth mode of vibration. There are three nodes as expected. The distance between two nodes now approaches the depth, but still the overall beam-like behaviour is remarkable. 39
2.15 The sixth mode of vibration. This mode is the fifth in the series of flexural modes. It has four nodes as expected. 39
2.16 The seventh mode of vibration. It is the second mode in the axial vibration series. 40
2.17 The eighth mode of vibration. This mode is the sixth in the series of flexural modes. There are five nodes as expected. 40
2.18 The ninth mode of vibration. It is the seventh mode in bending series. Note the presence of six nodes. 41
2.19 The tenth mode of vibration. It is the the third mode in axial vibration series. 41

2.20 Comparison of the natural frequencies of the cellular beams as calculated by the finite element analysis with those from the effective medium theories. The top half and the bottom half show the frequencies associated with the flexural and the axial modes respectively. The beams are made of regular hexagonal cells ($h/l = 1$ and $\theta = 30^o$) of orientation 1 and 2 (see figures 2.2 and 2.3). The value of t/l is 0.05. 42

2.21 A cellular beam made of non-uniform hexagonal cells ($h/l = 1.5$ and $\theta = 45^o$) having orientation 1. The beam runs horizontally as before. . . . 43

2.22 A cellular beam made of non-uniform hexagonal cells ($h/l = 0.5$ and $\theta = 60^o$) having orientation 2. 44

2.23 Comparison of the natural frequencies of orthotropic cellular beam as calculated by the finite element analysis and the isotropic effective medium theory. The beam is made of non-uniform hexagonal cells ($h/l = 1.5$ and $\theta = 45^o$) of orientation 1 (see figure 2.21). Value of t/l is 0.05. Frequencies corresponding to both the axial and the bending modes are presented. . . 45

2.24 Comparison of the natural frequencies of an orthotropic cellular beam as calculated by the finite element analysis and the isotropic effective medium theory. The beam is made of non-uniform hexagonal cells ($h/l = 0.5$ and $\theta = 60^o$) having orientation 2 (see figure 2.22). The value of t/l is 0.05. Frequencies associated with the flexural and the axial modes are presented. 46

2.25 The natural frequencies of beams made of triangular cells (cell orientations 1 and 2) compared with those of an effective medium. The top half and the bottom half show the frequencies associated with the flexural and the axial modes respectively. The value of t/l is 0.05. 48

3.1 Comparisons of the natural frequencies of a beam made of triangular cells with those of an equivalent continuum. The first few frequencies of the cellular beam are very close to those of the continuum. Later, the frequency curve of cellular beam becomes close to the horizontal indicating small increase in frequency per mode i.e. very high modal density. 54

3.2 The top figure is the modal density plot of a beam made of triangular cells, whereas the bottom figure is the that for a continuum. Note that for triangular cells, 592 modes appear between 8 kHz and 10 kHz. This shows a sudden decrease in the modal separation. In contrast, the continuum has only 13 modes in the same frequency band. 55
3.3 The natural frequency vs mode number plot for various thicknesses of the cell wall of the beam made of triangular cells. The plot indicates that at the lower mode number, modes are independent of thickness (hence stretching dominated) whereas the high mode number modes have frequency $\approx$ thickness (hence cell wall bending dominated). 58
3.4 Model of an isolated cell wall. The end connections with its neighbours are replaced by vertical k_v, horizontal k_h and torsional springs k_{theta}. . . . 59
3.5 A cellular beam made of square cells. 59
3.6 Comparisons of the natural frequencies of structure made of square cells with those of continuum whose properties are chosen to match the fundamental frequency. 61
3.7 A portion of the cellular beam showing thickness-shear mode of vibration. This is the overall 62nd mode. 62
3.8 A portion of the cellular beam showing thickness-shear mode coupled with axial mode. This is the overall 163rd mode. 63
3.9 Comparisons of the modal density plot for the square cells and the continuum for the first 800 modes. A sudden increase in the modal density is observed in the case of the square cells in the regime of cell wall resonance. 64
3.10 Comparisons of the natural frequencies of a beam made of hexagonal cells with those of continuum whose properties are chosen to match the fundamental frequency. 65
3.11 Modal density plot for beams made of hexagonal cells and continuum whose properties are matched to give the same fundamental frequency as the cellular beam. 961 modes are present in the case of the hexagonal cells in contrast with 476 modes for the continuum. 66
3.12 A cellular beam. The microstructure is composed of irregular cells. 66
3.13 The distribution of length of the cell walls of the beam shown in figure 3.12. 67

3.14 Histogram of thickness/length (t/l) ratio for the cell walls for the beam shown in figure 3.12. The distribution indicates that only about 10% cell walls have t/l ratio greater than 1/10 whereas 2.5% cell walls have t/l ratio greater than 1/5. Therefore, most of the cell walls (about 90%) have t/l ratio less than 1/10. 68

3.15 Comparison of the natural frequencies against the mode number for a beam made of irregular cells with those of a continuum whose properties are matched to give the same fundamental frequency. 69

3.16 Modal density plot for the beam made of irregular cells (top figure) and the beam made of continuum whose fundamental frequency is matched with that of a beam having irregular cells (bottom figure). The first 800 modes are considered. 70

3.17 Comparisons of the frequencies against the mode numbers for four topologies: triangular, square, hexagonal and irregular cells are considered. The first 800 modes are shown. 71

4.1 MAC plot correlating the continuum assumed modes and the finite element modes. The dark blocks on the diagonal indicate good correlation for the first few modes; yet the predicted frequencies based on these assumed modes are very inaccurate. 84

4.2 MAC plot representing correlation between the two sets of eigenvectors as calculated by the finite element and the reduced order model. The dark blocks on the diagonal show excellent correlation up to the eighth mode. The correlation for the ninth mode is not so good, whereas the tenth mode shows poor correlation. 84

4.3 The straight line correlation plot for the first (top left), eighth (top right), ninth (bottom left) and the tenth (bottom right) mode respectively. Note the degradation in the correlation with the mode number. 85

4.4 The first five mode shapes of the cantilever beam shown in figure 3.12. The deflected shape of the first mode resembles the first flexural mode of a solid fixed-free beam. The second, the third and the fifth modes resemble the second, third and the fourth flexural modes of a cantilever respectively. In contrast, the fourth mode is primarily an axial mode. . . . 87

4.5 An L-beam composed of irregular cells. Note that the left-most and the bottom-most boundary are fixed. 88

4.6 MAC plot representing correlation between the modes calculated by the finite element and the approximate method of the L-beam structure. The dark blocks on the diagonal show excellent correlation up to the eighth mode. The ninth and the tenth modes show poor correlation. 89
4.7 The first mode of free vibration of the L-beam. 90
4.8 The second mode of vibration. This mode is also a flexural mode, similar to the first mode, but the phase of vibration in the two limbs of the structure is opposite of the mode presented in figure 4.7. 91
4.9 The third mode of vibration. The horizontal arm is in stretching-compression mode of vibration whereas the vertical arm is in flexural vibration. 91
4.10 The fourth mode of vibration. This mode is similar to the third mode, the difference being that the vertical arm is in stretching-compression mode of vibration in this mode. The horizontal arm is in flexural mode of vibration. 92
4.11 The fifth mode of vibration. It is primarily a bending mode with each arm corresponding to the second mode of vibration for a fixed-pinned beam. 92

5.1 Driving point receptance as calculated from the finite element analysis using the full scale model compared with that of the reduced order model. Response is calculated due to a harmonic vertical load acting at a boundary node. Note that the peak associated with the first *axial* mode between the third and the fourth peaks is missing. The agreement is excellent up to the ninth mode. Anti-resonances are observed between any two resonance peaks as expected. 101
5.2 Undamped driving point response when a harmonic axial load acts at a boundary node. The response is evaluated from the full scale model as well as the reduced order model. Sharp resonance peaks are observed at the frequencies corresponding to the axial modes. The first axial mode missing in figure 5.1 is prominent now. 101
5.3 Undamped transfer receptance for the full scale model and the reduced order model due to a vertical load applied at the right hand boundary node. Note the absence of the anti-resonances between the resonance peaks in many cases. This a characteristic of transfer receptance. 102
5.4 Undamped transfer receptance plotted on the lines of figure 5.3. The driving direction is axial now. 103

5.5 FDAC plot representing correlation between the response vectors as calculated by the finite element simulations and the reduced model. The dark blocks on the diagonal show excellent correlation up to the ninth mode. 104
5.6 Driving point receptance due to a vertical load acting at a boundary node. Damping is included in the model. The response curves have the similar features as was observed in figure 5.1, with the difference is that the resonance peaks are now reduced due to damping. 105
5.7 A plot of the damping ratio (ζ_r) against mode number. The ratios estimated on the basis of the reduced model are very accurate except for the last mode. 106
5.8 Driving point receptance due to harmonic axial load when damping is included in the model. 107
5.9 Comparison of the transfer receptance when the load is vertical. Damping is included in the model. 108
5.10 FDAC plot representing correlation between the damped response vectors. The dark blocks on the diagonal show excellent correlation up to the ninth mode. 109

6.1 The experimental set-up. The beam is suspended horizontally using two cords, which simulate the free-free boundary condition. The data-logger and the visual display unit (laptop) are also shown. 113
6.2 The positions 1 and 2 of the excitation. Position 1 is suitable for exciting the flexural modes while position 2 is suitable for torsional modes. 114
6.3 A macrograph of a sample of Alulight foam. 115
6.4 A typical experimental impulse and the magnitude of its FFT are shown. 115
6.5 The magnitude and the phase of the accelerance FRF for the driving point excitation at position 1. The resonances and the anti-resonances are observed. The noise before the first resonance peak is mainly due to the soft suspension. 118
6.6 Driving point FRF when the beam is excited at position 2 instead of 1. The torsional modes which were not clear in the previous figure are distinct now. The first five peaks are found to be at 973 Hz, 1708 Hz, 2511 Hz, 3407 Hz and 4260 Hz respectively. 119

6.7 Fifteen driving point FRFs for the axial excitation, superimposed on each other. 120
6.8 The average FRF of the fifteen FRFs for the axial excitation shown in figure 6.7. Six resonance peaks associated with the axial modes are pronounced now. 121
6.9 An average FRF for the axial excitation of a solid aluminium rectangular bar. The sample has the same external dimensions as those of the metal foam sample. 122
6.10 The top figure shows the bending frequencies of two Alulight samples (about both the axes) and aluminium plotted against the mode number. The frequencies are normalised with respect to the fundamental frequency of the respective series. 126
6.11 Comparisons of the torsional frequencies and the shear modulus with mode number for the Alulight foam and the solid. The solid shows little stiffening, whereas the two foam samples show reduction in the shear modulus. 127
6.12 The plot of the frequency ratio and the the Young's modulus for the axial modes. 128

List of Tables

2.1 Data of a beam made of regular hexagonal cells having orientation 1. . . . 29

2.2 Geometric data of a beam made of regular hexagonal cells having orientation 2. . . . 29

2.3 The ratio E_b^*/E_1^* and E_b^*/E_2^* for beams made of hexagonal cells exhibiting orthotropy. . . . 33

2.4 Geometric data of the beam made of triangular cells having orientation 1. 34

2.5 Geometric data of the beam made of triangular cells having orientation 2. 34

2.6 Comparison of the position of the nodes between the cellular beam and a solid beam. . . . 38

2.7 Geometric data of the beam made of non-uniform hexagonal cells of orientation 1. . . . 44

2.8 Geometric data of the beam made of non-uniform hexagonal cells of orientation 2. . . . 44

3.1 Geometric data for the beam made of equilateral triangles having orientation 1 (see figure 2.4). . . . 53

3.2 Geometric data for the beam shown in figure 3.5. . . . 60

3.3 The geometric data for the beam made of regular hexagonal cells. . . . 63

3.4 Geometric data for the beam shown in figure 3.12. . . . 68

4.1 Comparison between the natural frequencies as calculated from the full model (equation 2.11) and the approximation based on pre-conditioned continuum modes for the cellular beam in figure 3.12. . . . 82

4.2 Comparison of the floating point operations for the full-scale problem (equation 2.11) and the approximation using the pre-conditioned continuum modes for both the models. Note that calculations of eigenvalues and eigenvectors for the reduced model include all the stages starting from the generation of the pre-conditioned assumed modes up to the prediction of the approximate frequencies and modes. 86
4.3 Geometric data for the L-beam shown in figure 4.5. 88
4.4 Comparison of the natural frequencies as calculated from the full model (equation 2.11) and the approximation using the pre-conditioned continuum modes for the L-beam shown in figure 4.5. 89

6.1 Geometric data for the two samples of rectangular bars made of Alulight. 116
6.2 Comparisons of the experimental results with theoretical predictions. . . . 123

Acknowledgments

First of all, I wish to express to my indebtedness to Dr. Atul Bhaskar, my supervisor, for his inspiring guidance and encouragement. His profound knowledge and clarity of thoughts has given me intellectual nourishment.

I am also grateful to our group head Prof. Andy Keane for the facilities he has provided for research. I also thank to Dr. Prashant B. Nair for useful discussions.

I thank Mr. Brian Newell and Mr. Andy Giles for their assistance in the dynamics laboratory.

I wish to thank to the Engineering & Physical Sciences Research Council (EPSRC) and the University of Southampton for providing financial support for carrying out this work.

I would like to thank all my colleagues David Stinchcombe, Dr. Andras Sobester, Alexander Forrester, Tom Etheridge, Tony Scurr, Dr. Neil Bressloff, Dr. Chen Hock Tan, Dr. Yong Zhang, Dr. Wenbin Song, A. Paventhan, Manoj Kumar, Susanta Ghosh, Avijit Rao, Sachin Sachdeva, Phani Chinchapatnam, Nicci Hoyle, Tom Barrett, ... who created a wonderful atmosphere in the workplace. I would also thank all my friends Dr. Collin Sones, Dr. Ajay Nayak, Partha Sarathi Dutta, Dr. Jayanta Sahu, Dr. Anand Thite, ... for their good wishes and encouragement. I wish to take this opportunity to express love and gratitude to my parents for their inspiration. Finally, special thanks to my wife Suparna for her understanding and inspired motivation.

Nomenclature

E^*	Effective Young's modulus of the cellular solid
G^*	Effective shear modulus of the cellular solid
ν^*	Effective Poisson's ratio of the cellular solid
ρ^*	Density of the cellular solid
E_s	Young's Modulus of the material of the cell wall
ρ_s	Density of the material of the cell wall
ν_s	Poisson's ratio of the cell wall material
E	Young's Modulus of the effective medium
ρ	Density of the effective medium
L	Lagrangian of a system, length of a sample
B	Width of a sample, perpendicular to the plane
D	Overall depth of a sample
I	Second moment of the area
I_p	Polar moment of inertia of the cross-section
s	Slenderness ratio
r	Radius of gyration
k_1	Shear factor
J	Torsional constant
l	Length of a cell wall
h	Height of a cell wall in a hexagonal cell
t	Thickness of a cell wall, time
V, $V(t)$	Potential energy of the structure
$T(t)$	Kinetic energy of the structure
$\mathbf{K}$, $\overline{\mathbf{K}}$	Stiffness matrix for the full model and the reduced model respectively

$\mathbf{M}$, $\overline{\mathbf{M}}$	Inertia matrix for the full model and the reduced model respectively
$\mathbf{C}$, $\overline{\mathbf{C}}$	Damping matrix for the full model and the reduced model respectively
$\mathbf{H}(\omega)$, $\overline{\mathbf{H}}(\omega)$	Frequency response function for the full model and the reduced model respectively
$\mathbf{f}$, $\overline{\mathbf{f}}$	Force vector for the full model and the reduced model respectively
P	Concentrated load
$\mathbf{q}$, $\mathbf{a}$	Generalised co-ordinates vector for the full model and the reduced model
$\mathbf{u}_i$, $\boldsymbol{\psi}_i$	i-th eigenvector for the full model and the reduced model respectively
λ_i, μ_i	i-th eigenvalue for the full model and the reduced model respectively
ω_r	r-th natural frequency for the full model
$\boldsymbol{\phi}$	Response vector
$\mathcal{F}$	Rayleigh's dissipation function
$\overline{\mathbf{Q}}$	Vector of generalised viscous damping force for the reduced model
ζ_i, $\overline{\zeta}_i$	i-th Damping ratio for the full model and the reduced model respectively
α, β	Damping coefficient
N, p	Number of degrees-of-freedom for the full model and the reduced model respectively
$\mathbf{T}$	Transformation matrix
$\mathbf{U}$	Modal matrix
$\mathbf{W}$	MAC matrix
$\mathbf{F}$	FDAC matrix
$\varphi(x)$	Transverse displacement field
v_x, v_y, θ	Axial and transverse displacement and, rotation of a node
v_x^b, $v_x^{tension}$	Two components of axial displacement, due to bending and tension/compression
σ	Relative sensitivity
R, g	Rayleigh's quotient
ϵ	Infinitesimally small number
δ_{rs}	Kronecker Delta
i, r, s	Subscripts for denoting indices
j	Subscript, $\sqrt{-1}$
b_i, c_i	Modal contribution associated with i-th mode
d_i, e_i	Co-efficients of the frequency equation of a shear beam
C_1, C_2, n	Constants

Chapter 1

Introduction

§1.1 Background

A large number of engineering materials can be successfully modelled as homogeneous continua. Conventionally manufactured metals, plastics and ceramics are examples of such materials. Most composites made out of these can also be treated as homogeneous (but not necessarily isotropic) matter at the macroscopic scale. As opposed to these, natural materials such as wood, cork, bone and tissues possess intrinsic porosity due to the presence of cells. These cells appear at length scales much greater than the atomic length scales but significantly smaller that the natural length scale of the bulk. We will refer to this intermediate length scale as mesoscopic. Porous internal structure leads to higher stiffness to weight ratio at the bulk level. This property is exploited in designing many processed materials such as metal and polymeric foams as well as honeycombs.

Cellular materials are increasingly being used in the industry. Foams and honeycombs are frequently used as the core material for sandwich constructions. Polymeric foams are commonly used in the packaging industry. They are also used for sound and shock absorption. Porous ceramics are used in catalytic converters. Besides these, many aeronautical, marine and automotive applications demand high stiffness to weight ratio and high strength to weight ratio where cellular materials are potentially applicable.

§1.2 Review of the past works

Characterisation of mechanical and thermal properties of cellular solids has attracted attention of many researchers in the past. A review of the relevant literature is presented here.

Investigation of the mechanical behaviour of cellular materials started in the middle of the 20th century. Research was initially motivated by the need to understand the mechanical properties of polymeric and plastic foams. Kelsey et al. [60] were probably the earliest contributors in this field. In 1958, they analysed the shear behaviour of an aluminium honeycomb sheet used as a core of aeronautical sandwich panels.

The existing literature in the area of mechanics of cellular materials is primarily devoted to the response under static loading. Elastic behaviour, plastic behaviour, buckling, fracture, and failure have been studied. A main objective of the study of static behaviour of foams is to investigate the deformation mechanism of the cell walls and, to develop relationship between the effective elastic parameters of the cellular solid and (i) the geometry (shape and size) and topology of the cells, (ii) the elastic properties of the cell wall material. Due to the difference in the mechanism of deformation at the cell level, the mechanical behaviour of honeycombs can be subdivided into the *in-plane* and the *out-of-plane* (normal to the plane of the cells) behaviour. Discussions on these two classes of problems will be presented separately. The in-plane behaviour of two dimensional cellular materials is described next. This is followed by discussions on three dimensional microstructured materials in section 1.2.2.

§1.2.1 In-plane behaviour of two dimensional cellular materials

Periodic foams made of parallel arrays of simple unit cells are reviewed in this section. The mode of deformation of the cell walls primarily depends on the topology. Hence, the macroscopic mechanical behaviour varies accordingly. Structures made of hexagonal cells (see top left of figure 1.1) are taken up first. They are commonly found, for instance, in synthetic honeycombs, cork, many woods etc. Christensen [11] showed that among the different cell types, regular hexagons (hexagons with all equal sides) possess the minimum surface area for the same amount of material. This is observed during the artificial production of foams in liquid state initially, where regular hexagon is the natural morphology because it minimises the surface energy.

Microstructures made of hexagonal cells

Lattices made of hexagons that possess two-fold rotational symmetry as well as two planes of mirror symmetry are considered here. Such lattices come back to the original orientation twice during a rotation of 360^o about an axis perpendicular to the plane of lattice (see figure 1.1). Due to this symmetry, the material made of such lattices is

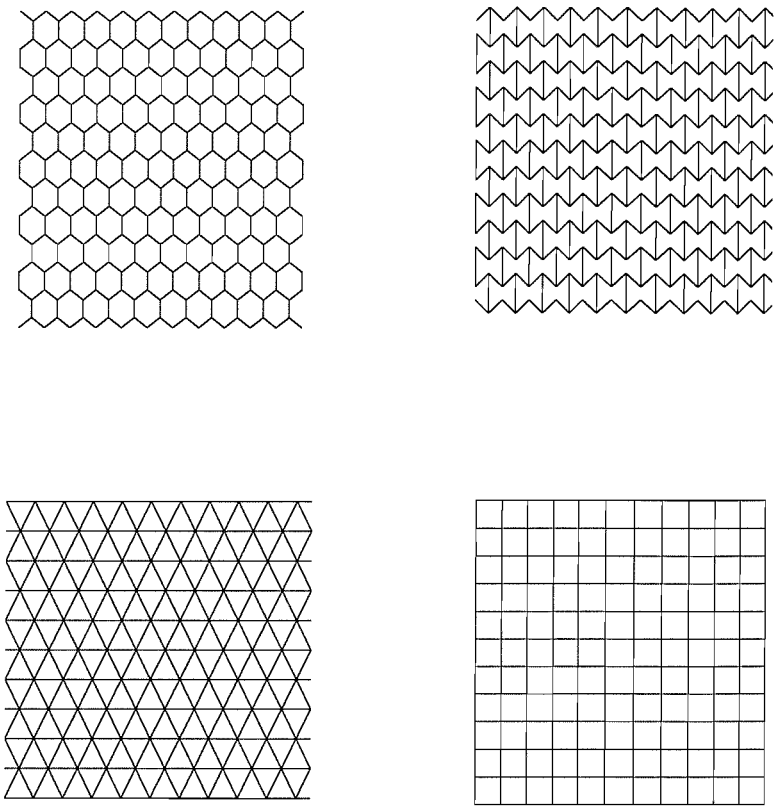

Figure 1.1: Periodic structures made of hexagonal, inverted hexagonal, triangular and square cells.

orthotropic. As a result, the number of elastic constants required to describe the in-plane mechanical behaviour are five: two values of Young's modulii, E_1^* and E_2^* in the directions 1 and 2 respectively, two Poisson's ratios ν_{12}^* and ν_{21}^* and one shear modulus G^*. Only four of these five constants are independent due to the reciprocal relationship $E_1^*\nu_{21}^* = E_2^*\nu_{12}^*$.

Abd El-Sayed et al. [1] first analysed the in-plane statics of solids made of hexagonal cells. They identified *cell wall bending* as the dominant mechanism of deformation for the tension-compression at the bulk level, and calculated the effective elastic modulii using the energy method of Castigliano. Further, they developed expressions for plastic collapse stress considering plastic bending of the cell walls. Gibson et al. [33] were the first to give a comprehensive account of the in-plane elastic behaviour of foams having hexagonal cells. They considered hexagonal cell as a *unit cell* for their analysis. Typical *regular* hexagons are shown in figure 1.2. Here, h is the height of the vertical cell walls, l is the length of the inclined cell walls, and t is the thickness of the cell wall. When $h = l$ and $\theta = 30^o$, the hexagon is regular. When $h \neq 1$ and/or $\theta \neq 30^o$, but two fold mirror

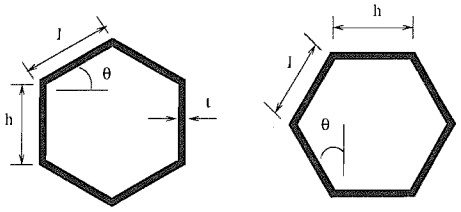

Figure 1.2: Geometry of a hexagonal cell in two different orientations. The parameters h, l, θ and t are shown.

symmetry and two fold rotational symmetry are present, the hexagons will be referred as non-uniform hexagons in this dissertation. Gibson et al. [33] concluded that the geometrical parameters: the aspect ratio h/l, the cell angle θ, and, the density parameter t/l affect the linear elastic behaviour. Macroscopic uni-axial tension-compression and shear behaviour were then deduced by analysing cell walls as beams using the Euler-Bernoulli beam theory. Only bending mode of deformation of the cell walls was included in their analysis, valid for low density foams.

Gibson et al. [33] developed closed-form expressions for E^* and G^* as functions of the geometrical parameters, h/l and θ, t/l and the modulus of elasticity of the cell wall material E_s. They found that the effective Poisson's ratio ν^* is a function of the geometry of the cell only, i.e. h/l and θ. Regular hexagonal cells (equal edge lengths) possess six-fold rotational symmetry. Therefore, periodic structures made of regular hexagons are in-plane isotropic. Gibson's expressions [33] when specialised for regular hexagons ($h/l = 1$ and $\theta = 30^o$), show that $E_1^* = E_2^*$ and $\nu_{12}^* = \nu_{21}^* = 1$. Further, the effective shear modulus G^* satisfies the relationship for an isotropic continuum $G^* = E^*/2(1+\nu^*)$. Gibson et al. [33] also studied the elastic collapse behaviour considering elastic buckling of the cell walls. They conducted experiments with silicone rubber honeycombs and showed that their experimental results generally agree with their analytical predictions.

The cells of the radial section of cork and the axial section of balsa wood, can be idealised as being hexagonal. Hence, Gibson et al. [35] and Easterling et al. [26] used the above-mentioned results for hexagonal cells [33] to analyse the elastic properties of cork and wood respectively. Kahle and Woodhouse [58] also used the same results to describe the elastic properties of softwood for assessing its suitability for musical instruments.

With the increase in volume fraction i.e. with greater thickness of the cell walls, contributions from the stretching and the shear deformation of the cell walls increase. Elastic analysis including all the deformations can be found in the text by Gibson and Ashby [34] and in the work of Masters et al. [71]. Both analyses are extensions of the

earlier beam analysis used by Gibson et al. [33].

Warren and Kraynik [103] included the bending as well as the stretching deformation of the cell walls, and analysed the kinematics of three cell walls connected at a node using the symmetry of regular hexagons. They expressed the elastic constants as a function of the area fraction. For low area fraction, their expression of the Young's modulus for regular hexagonal cells matches closely with that given by Gibson et al. [33]. Warren and Kraynik also studied the effect of non-uniform thickness of the cell walls, and showed that the Young's modulus is practically insensitive to such variations. They also showed that a material made of cells having six-fold rotational symmetry is transversely isotropic.

The micropolar theory describes solids with a microstructure as a micropolar or cosserat continuum. Micro-rotation of the nodes produced by the couple-stresses is considered as an independent variable for such continuum. This concept was introduced by Voigt [100] and the Cosserat brothers [16] in an attempt to generalise the mechanics of continua. Later, Eringen [27] developed the mechanics of micropolar continuum. Bazant and Christensen [7] developed finite-difference equations for the struts connected at nodes and calculated the effective elastic modulii of such a continuum. Wang and Stronge [101] used micropolar theory to analyse the stress field of elastic solids made of regular hexagonal cells. They considered a diamond-shaped cell as a unit cell to represent the micropolar continuum. Their expression of the Young's modulus agrees with that given by Gibson et al. [33].

The effect of bi-axial loading has also been studied [34]. When a structure made of hexagonal cells is subjected to bi-axial loading, the bending moments at the joints tend to reduce the effect due to loading in two orthogonal directions, for example, tension in both directions. The bending moments can be zero for certain combination of loadings. Under such loading conditions, stretching-compression is the dominant mechanism of deformation of the cell walls instead of bending as in the case of the uni-axial loading.

Cellular solids that possess cells with re-entrant corners such as inverted hexagonal cells (see top right figure in 1.1) exhibit an interesting behaviour. Due to the peculiar cell shape, when the structure is under overall stretching mode of deformation, it also elongates in the orthogonal direction instead of shrinking. Therefore, such solids exhibit negative Poisson's ratio. Lakes [63] first reported the fabrication of three dimensional re-entrant foams. Evans [24] named this class of solids as *auxetic*. Overacker et al. [77] showed the variation of the negative Poisson's ratio with certain directions of loading with respect to the microstructure. Scarpa et al. [86] studied the effect of uni-axial

loading on solids made of inverted hexagons using finite element as well as experimental methods. They showed that their results match closely with the values calculated using the expressions of Gibson et al. [33].

Microstructures composed of triangular cells

Ceramic honeycombs made of triangular cells have an important use in the automotive catalytic converters. Gulati [44] first analysed the static behaviour of lattices made of equilateral triangles (see bottom left figure in 1.1). He developed expressions for the effective elastic constants using an energy approach (Castigliano's theorem) and stated that such a solid is anisotropic in the plane. Hunt [56] analysed triangular networks analytically as well as experimentally, and showed that they are in-plane isotropic. He assumed that the joints of the triangular cells are pinned. Both Gulati's and Hunt's expressions contain a linear (t/l) dependence of the Young's modulus (l and t are the length and the thickness of a typical cell wall respectively), in contrast to the hexagonal cells where it is proportional to $(t/l)^3$. The $(t/l)^3$ proportionality is a consequence of the cell wall bending being the dominant mode of deformation in hexagonal lattices.

Deshpande et al. [21] showed that stretching-compression is the primary mode of deformation in the cell walls in a triangular network because of their connectivity at each node is 6. The stretching mode of deformation gives higher Young's modulus. Hence, solids made of triangular cells are stiffer than those made of hexagonal cells with the same area fraction. The Poisson's ratio of triangular foam is $1/3$, in contrast with the value of 1 for foams made of regular hexagons. Christensen [11] developed expressions for the shear and the bulk modulii of such solids. He showed that for the bulk modulus calculations, stretching-compression of cell walls is the dominant mode of deformation for triangular as well as hexagonal lattices.

Microstructures made of square cells

When structures made of square cells (see bottom right figure in 1.1), are subjected to loading in two orthogonal directions intrinsic to the lattice, stretching or compression of the cell walls is the only mechanism of deformation [34]. For loading in the diagonal direction, cell walls flex and the lattice shows a behaviour similar to that made of hexagonal cells. Therefore, macroscopically the structure is stiffer when loaded in the two cell wall directions rather than the diagonal direction. Such solids are anisotropic. Further due to the symmetries of the lattice, one concludes that the said anisotropy must be

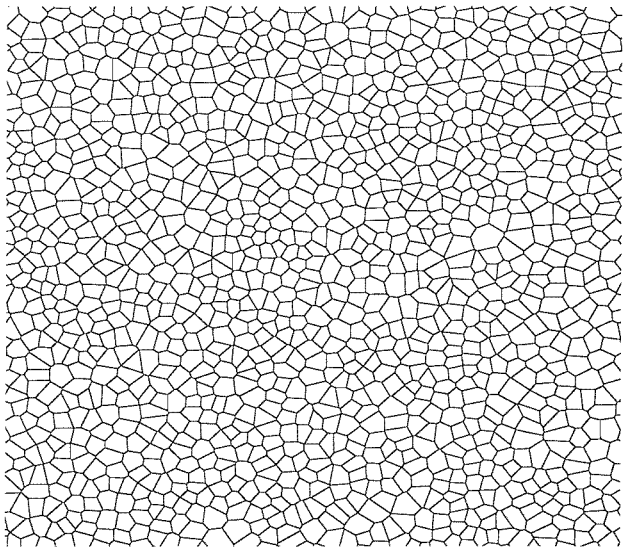

Figure 1.3: Schematic of irregular structure of a planar honeycomb. Note the absence of any periodicity.

orthotropy. Warren and Kraynik [103] also showed that structures made of square cells do not exhibit in-plane isotropy because of the square symmetry.

Other than these classical cell-shapes, star-shaped, circular, and elliptical cells have also been analysed. For example, elastic constants for solids made of star-shaped cells are found in Christensen's work [11]. Chung and Waas [15] analysed the in-plane elastic properties of solids made of hexagonally packed circular and elliptic cells using Castigliano's method. They showed that the material made of circular cells is isotropic, whereas that made of elliptical cells is orthotropic. Chung and Waas [15] also analysed experimentally the stress-strain behaviour and the collapse load of circular cell polycarbonate foams due to bi-axial loading.

Microstructures made of irregular cells

Natural as well as synthetic cellular solids are often non-periodic. Irregularity arises due to the variations in topology, cell wall thickness, and material properties of the cell wall. Figure 1.3 shows a hypothetical structure made of irregular cells. The *unit cell approach* is not suitable for modelling such geometries because of the absence of any periodicity.

The Voronoi diagram has been used by several researchers [89, 114] for filling a plane with irregular cells. For this purpose, a number of *nucleation points* are generated randomly. These points grow linearly in space simultaneously until any two boundaries meet. Thus, the whole area is divided into a number of cells such that any point within a

cell is closer to its nucleation point as compared to the nucleation points of its neighbours. Zhu et al. [114] studied the geometric properties of the Voronoi cells and presented their statistics.

Silva et al. [89] studied the effect of such irregular microstructure on their effective elastic properties. They modelled each cell wall as a beam and performed finite element analysis. Silva et al. concluded that on the average, the elastic properties of solids with irregular cells are close to those of regular hexagonal foams of the same area fraction. The variation reported was in the range of 4–9%.

Zhu et al. [114] proposed a factor for quantifying the irregularity of Voronoi cells. The factor was calculated based on the number of cells to be generated in a certain area such that any two nucleation points must be at a distance equal to or greater than a prescribed distance from each other. In another work [111], they used the same coefficient to study the effect of irregularity on the bulk elastic parameters. Their finite element results indicate that with the increase in irregularity, the Young's modulus and the shear modulus increase, whereas the bulk modulus decreases. The maximum deviation of the above-mentioned constants may be up to 20% as compared to those of regular hexagonal foams. However, they found that the irregular foams are nearly isotropic and the Poisson's ratio is very close to 1, as was observed by Silva et al. [89].

Simone and Gibson [91] studied the effect of the non-uniformity of the cell wall thickness on the Young's modulus for structures made of hexagons. Their numerical studies indicated that shifting material away from the cell edges into plateau borders at the vertices initially increases the modulus and peak stress of the cell walls. This happens due to the increase in the second moment of area at the ends of the cell walls where the bending moment is highest. When more material is removed, the increase in the second moment of area does not compensate for the reduction of the material from the cell wall and hence, the overall stiffness is reduced. They found that the effect of solid distribution (in the cell walls) on the elastic properties is not significant– this was also indicated earlier by Warren and Kraynik [103].

Silva et al. [89] scaled the Voronoi cells in a particular direction and thus introduced directionality to the models. They calculated the area fraction and the scaling factor of the Voronoi foam from its digital image using stereology. Their finite element calculations indicated that the Young's modulus is affected more by scaling than the Poisson's ratio. Scaling has minor effects on the shear modulus. Silva et al. concluded that on an average, for the same area fraction, the macroscopic elastic properties of solids with

irregular cells and hexagonal cells are the same even for the anisotropic case. Cowin [18] also studied similar effects on the elastic properties of porous materials. He defined the fabric ellipsoid as a measure of the local microstructural features and developed the so-called fabric tensor. Further, he developed a relationship between the effective elastic constants, the fabric tensor and the volume fraction of porous materials. His relationships require experimental determination of the unspecified scalar-valued functions of the volume fraction.

Homogenisation theory

The homogenisation theory has been applied for evaluating the effective properties of random heterogeneous media in which the macroscopic length scale is much larger than the length scale of the heterogeneity. Therefore, in such cases, the heterogeneous media can be assumed as a continuum at the macroscopic scale and its effective properties can be determined [96, 57].

Torquato et al. [96] viewed a piece of cellular solid as a two-phase composite (one phase being void), and applied the homogenisation theory of porous solids for deducing bounds on the effective elastic properties. Their calculations are based on the well-known Hashin-Shtrikman bounds [50]. They showed that for low area fraction, the upper bounds for the bulk modulus and the thermal conductivity of hexagonal, triangular or square foams match exactly with the theoretical results. Later, Hyun and Torquato [57] showed that for hexagonal as well as triangular cells, the three-point bounds [97] match better with the analytical results irrespective of the area fraction.

§1.2.2 Out-of-plane behaviour of cellular materials

When planar structures made of cells are subjected to out-of-plane loading, they become elongated, compressed or sheared. Stress distribution is now much more complicated because each cell face suffers a non-uniform deformation. Stretching-compression is the primary mode of deformation in this case rather than bending. Hence, structures are much stiffer in the transverse direction. As a result, they are used as core in sandwich panels which carry the major portion of shear and transverse loads.

Earlier, the work of Kelsey et al. [60] was mentioned as one of the pioneering contributions. They used the energy method of Castigliano for evaluating the lower and the upper bounds of the two shear modulii. They also validated their analysis experimentally. Similar analyses were carried out by Chang and Ebcioglu [9], and Penzien

and Didriksson [80]. Grediac [39] used the finite element method for studying the shear behaviour in core made of hexagonal cells. Scarpa et al. [86] performed similar analysis with auxetic core. Hohe et al. [52] used a homogenisation approach based on energy equivalence, and analysed cellular cores of various topologies [52, 53]. A review of the stress-strain relations and the nonlinear behaviour for two dimensional cellular cores can be found in the work of Hohe et al. [54].

§1.2.3 Mechanical behaviour of three dimensional cellular materials

Three dimensional foams are classified as *open cell* or *closed cell* foams depending upon their structure– a network of struts is known as an open cell, whereas that of plates is termed closed cell. Sometimes, foams are also found to have partially closed cells. The mechanical properties of the open cell foams and its closed cell counterpart are not the same given a volume fraction. This is due to the difference in the mechanism of deformation. For example, in the case of closed cell foams, the cell surfaces connecting the struts affect the mechanical behaviour considerably due to plate deformation mechanisms. In general, we have a much poorer understanding of closed cell foams compared to open cell foams. It was recognised by several authors [32, 62, 22, 79, 74, 36] that the most important property affecting the mechanical behaviour of foams is their volume fraction ρ^*/ρ_s, where ρ^* and ρ_s are the densities of the foam and the cell wall respectively.

The general form of the Young's modulus of a low density foam was first proposed by Egli [22],

$$\frac{E^*}{E_s} = C_1 \left(\frac{\rho^*}{\rho_s}\right)^n, \tag{1.1}$$

where, E^* is the equivalent Young's modulus of the foam, E_s is the Young's modulus of the cell wall material, and C_1 is a material-dependent constant. The value of n depends upon the mode of deformation of the cell wall [40, 31]. For example, $n = 1$ indicates stretching-compression of the cell wall is the only mode of deformation. $n = 3$ represents bending or twisting of the cell surfaces. When bending, twisting, and stretching govern the behaviour, the value of n lies in the range $1 \leq n \leq 3$. Due to the difference in the mechanism of deformation, reviews for the open cell and the closed cell foams will now be presented separately.

Open cell foams

Gent and Thomas [32] first analysed the linear elastic behaviour of open cell foams in 1959. They modelled foams as networks of randomly-oriented thin elastic threads

connected to rigid spherical joints. For small volume fraction, they calculated $E^*/E_s = \frac{1}{6}\rho^*/\rho_s$, and $\nu^* = \frac{1}{4}$ using an energy approach. They considered stretching-compression as the only mode of deformation of the cell rib. Later, Christensen [12] obtained the same results as Gent and Thomas [32]. Lederman [67] also used the energy method assuming extension of the cell edges, and found a linear relationship between the elastic parameters and the volume fraction of foams. His findings were similar to those of Gent and Thomas [32]. Kanakkant [59] showed that such foams are highly anisotropic and the tensile modulus differs significantly from the compressive modulus.

Ko [62] modelled the foam topology as a network of beams in hexagonal closed packing (HCP) and face-centered-cubic packing (FCC). He arbitrarily chose a principal direction of uni-axial strain and calculated the effective Young's modulus using three-dimensional beam analysis. He included both the stretching and the bending deformations in the analysis. Ko found a relationship similar to that of Gent and Thomas for HCP, but a different one for FCC as $E^*/E_s = \frac{7}{3}(\rho^*/\rho_s)^2$. His results indicate that the dominant deformation mechanism changes from being stretching for HCP to becoming bending for FCC. Patel and Finnie [79] assumed the unit cell as a pentagonal dodecahedron. Their theoretical analysis, considering bending as the only mechanism of deformation of the cell walls, yields $E^*/E_s = (\rho^*/\rho_s)^2$.

Menges and Knipschild [74] analysed an isolated joint consisting of four rods meeting at a tetrahedral angle using beam theory. They showed that the elastic modulus is proportional to $(\rho^*/\rho_s)^2$. Gibson and Ashby [36] assumed the foam as a network of struts interconnected in the form of a cube and used dimensional arguments. They considered cell wall bending as the dominant mechanism of deformation, and showed that the Young's modulus varies as $(\rho^*/\rho_s)^2$. Their unit cell oversimplifies a real foam. Warren and Kraynik [104] performed linear elastic analysis of open cell foams using an isolated tetrahedral joint. Extensive reviews of the experimental and theoretical work on the various mechanical properties– stiffness, strength, fatigue, failure and impact behaviour of the polymeric foams are discussed in the work of Progelhof and Throne [82] and Hilyard [51].

Many of the foam models described so far, consider tetrahedron as a unit cell. Later on, unit cells in the form of regular *tetrakaidecahedra*, containing 14 faces with 8 hexagons and 6 squares, became popular. This cell, having minimum surface area for a given volume, was proposed by Lord Kelvin [61]. This is a good choice as a unit cell because often such cells with minimum surface area are generated during the phase-separation

processes of foam production. Weaire and Phelan [108] later identified a cell which is lower in surface area than the Kelvin's cell. This cell form is a combination of two cell types, a 14 sided form with faces of pentagons and hexagons combined with the 12 sided regular dodecahedron. A comparison of the surface properties of different cells can be found in Christensen [11].

Dement'ev and Tarakanov [19] first modelled an open cell foam using regular tetrakaidecahedron. They analysed theoretically the compression of foams neglecting the strut-bending and showed $E^*/E_s = (1/9)\rho^*/\rho_s$. In another study [20], Dement'ev and Tarakanov considered bending and showed $E^*/E_s = (4\sqrt{2}/9)(\rho^*/\rho_s)^2$. Warren et al. [106] used analytical methods, whereas Zhu et al. [112] performed numerical calculations to study the elastic properties of the open cell foams having Kelvin cells. Both of these studies indicate that such foams are nearly isotropic. For uniform struts of square cross-section, Warren et al. [106] obtained the same result as Demet'ev and Tarakanov [19]. Li et al. [68] developed closed-form expressions of the elastic parameters analysing tetrakeidecahedron as a unit cell. They included all the three modes of deformation of the cell walls in their model with different shapes of the strut cross-section. Choi and Lakes [63] modelled three dimensional foam as an idealised 14-sided unit cell. They analysed the difference in the Young's modulus between conventional and re-entrant foams theoretically as well as experimentally. Christensen [11] showed that the bulk modulus of these foams is governed by the tension mechanism and the shear modulus by the bending/torsion mechanisms.

Closed cell foams

A closed cell foam can be viewed as the cell walls/surfaces connected to each other along the cell edges [12, 35]. Therefore, when a closed cell foam is subjected to load, the deformations are due to the stretching of the cell surfaces along with the bending of the cell edges. Simplified unit cell models are preferred by many researchers [12, 35, 41, 91] because of the complexity involved in analysing the mechanics of the cell surface and the cell edge together.

Christensen [12] analysed random closed cell foam assuming the cell surfaces as membranes. He developed expressions for the elastic constants of an isotropic closed cell foam as

$$\frac{E^*}{E_s} = \frac{2(7-\nu_s)}{3(1-\nu_s)(9+5\nu_s)}\frac{\rho^*}{\rho_s}, \quad \nu^* = \frac{1+5\nu_s}{9+5\nu_s} \tag{1.2}$$

where, ν^* is the Poisson's ratio of the foam and ν_s denotes the Poisson's ratio of the

cell wall material. Further, he showed that the Young's modulus of a closed cell foam is about three times greater than that of its open cell counterpart.

Gibson and Ashby [35] used a semi-empirical approach and proposed the following expressions for closed cell foams

$$\frac{E^*}{E_s} \approx V_c^2\left(\frac{\rho^*}{\rho_s}\right)^2 + (1-V_c)\frac{\rho^*}{\rho_s}, \quad \frac{G^*}{E_s} \approx \frac{3}{8}\left[V_c^2\left(\frac{\rho^*}{\rho_s}\right)^2 + (1-V_c)\frac{\rho^*}{\rho_s}\right], \quad \nu^* \approx \frac{1}{3}, \tag{1.3}$$

where, V_c is the fraction of the solid in the cell edges and $1-V_c$ is the remaining fraction in the cell-surfaces, and G^* is the shear modulus of the foam. If V_c is zero, then the above expression reduces to the expression of the elastic constants for an open cell foam. The expression needs the evaluation of V_c from the experiments which may be quite difficult in many practical situations.

If the foam is assumed to be a two-phase isotropic composite, then Hashin-Shtrikman bounds [50] dictate

$$\frac{E^*}{E_s} \leq \frac{\rho^*/\rho_s}{1+C_2(1-\rho^*/\rho_s)}, \quad \text{where} \quad C_2 = \frac{(1+\nu_s)(13-5\nu_s)}{2(7-5\nu_s)}, \quad \nu^* \leq 0.5. \tag{1.4}$$

Other than these theoretical studies, the elastic constants for foams were also evaluated numerically by analysing a unit cell model. BCC or FCC tetrakaidecahedral cells have been used in many studies [41, 91]. For example, Simone et al. [91] studied BCC tetrakaidecahedral cell by the finite element method using shell as well as continuum elements. For the loading in [100] direction, they proposed

$$\frac{E^*}{E_s} \approx 0.209\left(\frac{\rho^*}{\rho_s}\right)^2 + 0.315\frac{\rho^*}{\rho_s}, \tag{1.5}$$

applicable for $\rho^*/\rho_s \leq 0.2$. They observed in their numerical simulations that the Young's modulus differs by about 10%, when the loading direction is changed to [111] and [110] from the original [100] direction. An elaborate discussion of the different models of foams can be found in Gresnestedt's work [41].

Three dimensional foams made of irregular cells

Van der burg et al. [99] analysed the effect of irregularity in open cell foams by generating random Voronoi cells in three dimensions. Their finite element results showed that the Young's modulus increases with the non-uniformity of the cell size. Zhu et al. [113] found that for low density foams, the Young's modulus and the shear modulus increases with the irregularity, whereas the bulk modulus decreases, as is the case for two dimensional foams studied in [114]. Grenestedt et al. [42] created foams of irregular cells by perturbing

the nodes of a tetrakaidecahedral cell for studying similar effect. They found that the bulk modulus as well as the shear modulus are affected very little by cell shape variations. Roberts et al. [84] generated closed cell as well as open cell foams using the Voronoi tessellation and a Gaussian random model. Their conclusions regarding the effect of the cell shape were similar to those of Grenestedt et al. [42].

Simone and Gibson [91] studied the effect of solid distribution in foams. They found that for open cell foams, the Young's modulus is practically insensitive to non-uniformity of cell wall thickness– an observation made for planar case [91] too. Their numerical study on closed cell foams also showed that the elastic properties do not differ much with such variations.

For irregular honeycombs or foams, often simulation of the real microstructure becomes important. Hollister et al. [55] introduced digital imaging techniques to study the effect of microstructural morphology of bones in their finite element simulations. Garboczi et al. [31] developed an algorithm to calculate the elastic properties of random multi-phase materials. The algorithm treats each pixel of the digital image as a finite element.

A review of the mechanical problems of solid and liquid foams can be found in Weaire and Fortes [109]. Similarly, detailed discussion on the elasticity and failure strength of foams can be found in the work of Kraynik and Warren [107] and Gibson and Ashby [35]. Gibson's work [37] is a similar review on metallic foams.

§1.2.4 Effects of imperfections in cellular materials

Various defects, for instance, the absence of cell walls, the presence of holes, notches and cracks are quite common in practical foams. Prakash et al. [81] first studied the effect of local strengthening and weakening on the macroscopic response of structures. They used optical images of samples made of hexagonal cells. They filled up cells in arbitrary locations with paraffin wax and thus introduced a local stiffening effect. Removal of the cell walls was introduced for local softening effect. They studied qualitatively the effect of the defects on the deformation bands and the strain hardening.

The effect of defects has frequently been studied by several authors [90, 13, 45, 3] using the finite element method. Silva et al. [90] simulated the effect of missing cell walls on the compressive strength using the finite element method. They showed quantitatively that local defects cause a sharp decrease in the effective Young's modulus of solids made of hexagonal as well as irregular planar networks. For example, 10% reduction in

density due to defects caused a 60% reduction in strength of solids made of Voronoi cells. They found that localised strains frequently appear for irregular cells but relatively less so for periodic cells. When four or more adjacent cell walls are removed, a localized band of cells collapse in the defect zone, and the effective modulus and strength are reduced. The mechanical properties effectively degrade to zero when 35% of the cell walls were removed, because the whole solid is divided into two parts. Similar to the earlier results [81], they indicated that even those defects which have a negligible effect on density can alter the failure pattern as well as the effective properties significantly.

Chen et al. [13] studied the influence of several imperfections (waviness, non-uniform cell wall thickness etc.) on the yielding of irregular foams. Guo and Gibson [45] studied the effect of large circular cut-outs on the elasticity and plasticity. Chen et al. [14] extended the work of Guo and Gibson [45] by considering the effect of inclusions in addition to holes. They compared their finite element results with the Hashin-Shtrikman [50] bounds. They found that the strength of such materials is relatively unaffected with the presence of holes and inclusions. Andrews et al. [3] considered three types of defects– circular holes, sharp cracks, and notches in their numerical study.

Previously cited works in this section were confined to two dimensional cases. There are some attempts to study the influence of imperfections in three dimensional foams too. Simone and Gibson [92, 93] observed that the discrepancies are of an order of magnitude between their experimental results of real aluminium foams and the properties of an ideal foam using tetrakaidecahedral cell as a repeating cell [91]. This difference is attributed to the presence of curvature and corrugations of the cell faces in real foams. Grenestedt et al. [40] showed that if the wave amplitude of the cell surfaces is five times the cell wall thickness, the stiffness can be reduced by 40% as compared to those with flat faces.

§1.2.5 Nonlinear Elastic Behaviour

If the solid material is linearly elastic, under uni-axial loading all cellular structures behave linear elastically for small deformations. With the increase in load, the behaviour becomes nonlinear. When a critical stress is reached, the cells begin to collapse. The elastomeric materials fail by the elastic buckling of the cell walls. Since the buckling is elastic, the deformations are recoverable on unloading. Elastic-plastic honeycombs fail due to the formation of plastic hinges at the points of maximum bending moment of the bent members; elastic-brittle honeycombs fail by brittle fracture of the cell walls. In the last two cases, the deformations are not recoverable while unloading. Eventually,

at high strains, the cell walls collapse sufficiently such that opposing cell walls touch (or their broken fragments pack together) and further deformation compresses the cell wall material itself. This gives the final, steeply rising portion of the stress-strain curve known as *densification* [35]. Analysis of the nonlinear behaviour of honeycombs can be found in the text of Gibson and Ashby [35], works of Overacker et al. [78] and Chen et al. [13]. Nonlinear elastic behaviour of open cell foams was studied by Warren and Kraynik [105].

§1.2.6 Dynamics of cellular materials

While there are numerous studies on the statics of cellular solids, the dynamics of this class of materials appears to have received less attention. Wang and Stronge [102] studied elastic honeycombs made of hexagonal cells, under periodically fluctuating forces. They developed a relationship between the micro-inertia, excitation frequency and the cell wall geometry using the micropolar theory. Baker et al. [5] studied the effect of impact and energy absorption of two dimensional metallic foams. Very little literature is available on the dynamic analysis of sandwich structures with cellular cores. Scarpa et al. [87] analysed the characteristics of the vibration of sandwich plates made of auxetic materials. Their results indicate that using auxetic materials as a core significantly improves the bending stiffness for particular cell parameter ranges and thus, the dynamic performance of sandwich structure could be improved significantly. Nilsson et al. [75] studied the dynamics of sandwich beams with hexagonal foam as a core. They developed analytical expressions of predicting the natural frequencies of sandwich beams. Studies have been carried out by several researchers [48, 69, 6] to investigate the effect of the porosity on the nonlinear damping properties of aluminium foam.

§1.3 Objectives and scope of the present work

The present dissertation is concerned primarily with the dynamics of cellular structures. In the previous section, we observed that the published literature is devoted to analysing the elastic and plastic behaviour, failure, buckling, creep etc., whereas the understanding of dynamics is limited. Cellular structures are often subjected to dynamic forces in addition to the static loadings. As a result, there is a need to understand the dynamic behaviour for efficient design of such structures. The main motivation of the present work arises from this need.

Structures made of small cells are complex, hence, a field description using the theory

of elasticity is practically impossible. Therefore, a computational approach is more suitable for the analysis of such structures. In the present work, the finite element method is used as a computational tool for modelling of cells at the meso-scale. This method is perhaps the best choice in this context as it can include the detailed structural features along with the complex loading and boundary conditions. Further, with the finite element method, it is comparatively easy to vary the geometrical and material parameters of the microstructure in a controlled manner and perform the analyses, whereas it is practically impossible to control the parameters independently in the case of the laboratory experiments. These justify the choice of the finite element method for the present work. Analytical approaches are also used to some extent.

For the finite element analysis, cell walls are modelled as elastic beams. Therefore, the whole structure is represented by a network of elastic beams. Axial deformation of the beams is included in the model for the sake of generality. The analysis is linear. This study is limited to the elastic range of the cell wall material properties.

A systematic numerical study to understand the continuum behaviour and any departure therefrom is undertaken in this thesis. Modal characteristics of structures made of cellular material are compared and contrasted with those of structures made of continua.

The finite element models of cellular structures tend to be computationally demanding because of the large size of the models. The issue of computational economy and approximations is, therefore, addressed.

Experimental work to understand the modal behaviour of rectangular bars of aluminium foams is carried out. Axial, bending and torsional modes are studied and the effective elastic modulli are derived from the modal frequencies. Again, these observations are compared and contrasted with the modal characteristics of homogeneous solid of similar shape and size.

A chapter-wise outline of the dissertation is presented in the next section.

§1.4 Outline of this dissertation

Numerical experiments on cellular beams having hexagonal as well as triangular cells are considered in Chapter 2. The finite element calculations are performed to obtain the static response and to calculate the natural frequencies and the mode shapes as well. The accuracy of predictions using isotropic beam bending formula is tested for problems having directional preference in the cell geometry (hence exhibiting orthotropy). A Rayleigh's principle based method is then employed to compute the fundamental

frequency economically.

Guided by the results in Chapter 2 that the overall behaviour of cellular structures resembles that of a continuum at low mode numbers, the validity of this to moderately high mode numbers is examined in Chapter 3. The dependence of modal spacing and modal density on mode number is studied and compared with that of continuum. A variety of cell geometries are considered.

The problem of reducing the computation time for large scale models of cellular structures is addressed in Chapter 4. A method based on so-called *continuum modes* is proposed to reduce the order of the models of cellular structures for the low end of the spectrum. A direct application of the variational method based approximation leads to difficulties. The source of this difficulty is identified and a method based on inverse power iterations is employed to pre-condition the set of basis modes. A sensitivity analysis is presented to understand the surprisingly poor performance of the basis modes when pre-conditioning is not carried out. The accuracy and the computational expense are systematically studied on numerical models of two different model structures.

Encouraged by the results in Chapter 4, the method using the continuum modes as basis is employed for response calculations in Chapter 5. Damping is introduced in the model and comparisons are made between response calculated from the full scale model and that obtained from the proposed reduced order model.

The validity of the effective medium theory is examined experimentally in Chapter 6. The effective elastic modulii (the Young's modulus and the Poisson's ratio) are determined for samples of metallic foam. The dependence of the Young's modulus on mode number is studied.

Conclusions and the future work are presented in Chapter 7.

Chapter 2

Applicability of the effective medium theory to statics and dynamics of cellular beams

§2.1 Introduction

Equivalent medium theories have been proposed for cellular material when the strain field is uniform. The simplest case of this is the uni-axial tension. However, the applicability of such theories to non-uniform strain fields has not been explored in the past. From this point of view, the beam bending problem affords a simple practical situation where the strain field at the bulk level is non-uniform. This is a consequence of the Kirchoff's hypothesis for thin beams that plane sections remain plane and perpendicular to the neutral axis. With the motivation to test the validity of the effective medium theories for the beam bending problem, numerical experiments on the statics and the dynamics of cellular beams are presented in this chapter.

It is proposed here that the transverse bending of cellular beams is guided by effective elastic properties corresponding to the Young's modulus in the axial direction. The rationale behind this assertion is two folds. First, the beam bending problem has axial strain as the main mechanism of strain energy storage. Therefore, the overall structure at the bulk level must show cells extending and compressing *axially*. The extent of stretching and compression of cells must depend on their distance away from the centre line of the overall beam. Second, the mechanism of strain energy storage for stretching and compression of cells (which is cell wall bending for hexagonal cells) must be the

same as that for uniform strain fields (as in Gibson and Ashby [34]) as well as for non-uniform strain fields provided that the non-uniformity for strain field is not severe. This requires the cells being small compared to the overall depth of the beam in the transverse direction. The distinction between the properties in the two directions is crucial for media that are effectively orthotropic.

Cellular cantilever beams with tip loads are considered. The low frequency dynamics for isotropic as well as orthotropic effective media are undertaken. An approximate method for the calculation of the fundamental frequency based on the static deflected shape is presented. A study of the dynamics when the continuum behaviour breaks down will be taken up in the next chapter.

§2.2 Calculation of response of cellular structures using the finite element method

Cellular structures are modelled as planar networks of elastic members in this dissertation. Each cell wall is modelled as a two node or three node Euler-Bernoulli beam having three degrees-of-freedom at each node. Thus, the nodes and their connectivity describe the geometry completely. The width normal to the plane of the structure is taken as unity. The degrees-of-freedom transverse to a cell wall along with the rotation at the end nodes account for the beam bending energy of the cell walls. The degrees-of-freedom in the direction of the line joining the end nodes of a cell wall provide stretching energy. Hence, the displacements in the horizontal and the vertical directions along with the rotation of all the nodes define the configuration of the whole structure. Within each beam element, cubic interpolation is used for the transverse displacements, whereas the linear interpolation is used for the axial displacements.

The strain energy of the whole structure is determined by summing up the energy contributions arising from different parts. For small displacements around equilibrium, the strain energy V of a structure is a quadratic function in the generalised co-ordinates [88],

$$V = \frac{1}{2}\sum_{i=1}^{N}\sum_{j=1}^{N} K_{ij}q_iq_j = \frac{1}{2}\mathbf{q}^T\mathbf{K}\mathbf{q} \tag{2.1}$$

where $\mathbf{q}$ is the vector of the generalised co-ordinates and $\mathbf{K}$ is the global stiffness matrix $(N \times N)$ of the structure having N degrees-of-freedom. The potential energy of the external loads can be expressed as

$$W = -\mathbf{f}^T\mathbf{q} \tag{2.2}$$

where $\mathbf{f}$ is the vector of the generalised forces. The total potential energy of the system is given by $\Pi = V + W = \frac{1}{2}\mathbf{q}^T\mathbf{K}\mathbf{q} - \mathbf{f}^T\mathbf{q}$. Applying the Principle of Minimum Total Potential Energy (PMTPE), the first variation of the total potential energy of the structure must be zero

$$\delta\Pi(q_1, q_2, ..., q_N) = 0. \tag{2.3}$$

This leads to the following set of algebraic equations

$$\mathbf{K}\mathbf{q} = \mathbf{f} \tag{2.4}$$

which can be solved for the unknowns $q_i, i = 1, 2, ..., N$. The formulation presented so far suffices for the calculation of static response of cellular media. When the dynamic response needs computing, additional energy functionals need to be considered. This is discussed in the next subsection.

§2.2.1 Free vibration calculations for cellular structures

For small oscillations around equilibrium, in the absence of any centripetal and Coriolis forces, the kinetic energy of a structure can be expressed as a quadratic function in the generalised velocities $\dot{\mathbf{q}}$,

$$T = \frac{1}{2}\sum_{i=1}^{N}\sum_{j=1}^{N} M_{ij}q_iq_j = \frac{1}{2}\dot{\mathbf{q}}^T\mathbf{M}\dot{\mathbf{q}}. \tag{2.5}$$

Here, $\mathbf{M}$ is the global inertia matrix ($N \times N$) of the structure. The potential energy $V = \frac{1}{2}\mathbf{q}^T\mathbf{K}\mathbf{q}$ is the same as before (see equation 2.1). Damping is assumed to be derivable from the Rayleigh's dissipation function (whenever it is accounted for in a later chapter of this dissertation), which is a quadratic function in the generalised velocities,

$$\mathcal{F} = \frac{1}{2}\dot{\mathbf{q}}^T\mathbf{C}\dot{\mathbf{q}}, \tag{2.6}$$

where $\mathbf{C}$ is the damping matrix. All other forces are assumed to be obtainable from the first variation of the external work done

$$\delta W = \sum_{i=1}^{N} f_i\delta q_i, \quad i = 1, 2, ..., N. \tag{2.7}$$

For a conservative system, the Lagrangian L takes the form $L = T - V$. Substituting L and $\mathcal{F}$ into Lagrange's equations of motion [73]

$$\frac{d}{dt}\left(\frac{\partial L}{\partial \dot{q}_i}\right) - \frac{\partial L}{\partial q_i} + \frac{\partial \mathcal{F}}{\partial q_i} = f_i, \quad i = 1, 2, ..., N \tag{2.8}$$

we obtain the following set of coupled second order ordinary linear differential equations

$$\mathbf{M}\ddot{\mathbf{q}} + \mathbf{C}\dot{\mathbf{q}} + \mathbf{K}\mathbf{q} = \mathbf{f}(t). \tag{2.9}$$

This chapter is concerned with the undamped free vibration of the cellular structures. Hence, equation (2.9) reduces to

$$\mathbf{M}\ddot{\mathbf{q}} + \mathbf{K}\mathbf{q} = \mathbf{0}. \tag{2.10}$$

Looking for synchronous free vibration, equation (2.10) leads to the well known algebraic eigenvalue problem

$$\mathbf{K}\mathbf{u}_r = \lambda_r \mathbf{M}\mathbf{u}_r \tag{2.11}$$

where λ_r is the r-th eigenvalue and, $\mathbf{u}_r$ is the corresponding eigenvector. The square root of the eigenvalue λ_r is the r-th natural frequency ω_r of the overall structure. Eigenvectors are the mode shapes.

The expressions for the kinetic energy and the potential energy are written for each element. The energy expressions for the whole structure is given by the sum of energies of the constituent parts (the finite elements). The element energies are expressed in terms of the local co-ordinates whereas they are expressed in terms of the global co-ordinates for the complete structure. The correspondence between the global co-ordinates and the local co-ordinates needs establishing which involves co-ordinate transformation and a careful book-keeping of the degrees-of-freedom. The procedure of adding energies and deriving global equations of motion from the total energy expressions is commonly known as assembly. From these energies, the global stiffness matrix $\mathbf{K}$ and the global inertia matrix $\mathbf{M}$ are assembled [73]. The procedure described here was implemented in the MATLAB [72] environment. Finally, the boundary conditions at the fixed end of the cantilever were applied by immobilising all the relevant degrees-of-freedom– this was achieved by deleting the corresponding rows and columns of the two matrices. This results in the eigenproblem of the form (2.11). For statics, the force vector $\mathbf{f}$ is generated along with $\mathbf{K}$ followed by solving equation (2.4) after applying the boundary condition.

§2.3 Effective elasticity of hexagonal and triangular lattices

Structures made of cells possess geometrical features at two scales of length. First, the length scale of the overall structure, say l_s, is typically represented by the characteristic

length of a hypothetical solid when the porosity is completely filled. There is another length scale intrinsic to the microstructure, say l_c, which represents the average characteristic length of cells. l_c is assumed to be small, i.e. $l_c \ll l_s$ (see figure 2.1). Therefore, such structures are not homogeneous at length scales of the order of cell dimensions. However, when the length scales involved in the deformed shape at the macroscopic level are much greater than l_c, the bulk mechanical behaviour is expected to resemble that of an equivalent continuum. This happens for low frequency dynamics, since the wavelengths involved far exceed the cell size. Hence, for lower modes, a cellular structure can be replaced by a homogeneous continuum. Note that for a standing wave, wavelength can be approximately considered as double the distance between any two adjacent nodes or anti-nodes of the associated mode.

Low and high frequency regions can be best characterised using the wavelength of the standing waves for a given normal mode. When this wavelength is much greater than typical cell size, l_c , the corresponding natural frequency will be referred to as *low frequency*. Similarly, when the wavelength is close to l_c, the associated frequency will be defined as *high frequency*. In this way we will use the phrases, low frequency and long wavelength and, high frequency and short wave length, synonymously. The actual values of the frequency is unimportant here since it will vary depending upon various factors, such as the cell geometry, geometric and the elastic properties of the cellular structures.

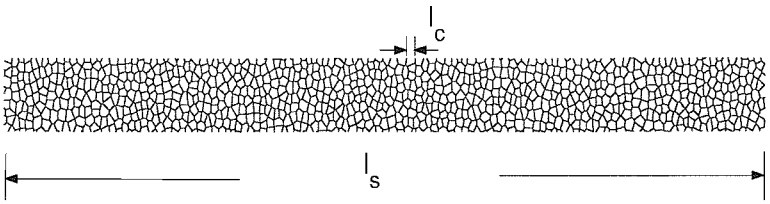

Figure 2.1: Two length scales of the structures made of cells. The length scale l_c is associated with the average cell size and, the length, l_s, is associated with the overall dimensions.

While replacing the cellular material by an equivalent continuum, the overall dimensions of the structure (beam in this case) must be kept unaltered. As a result, the continuum is obtained by filling the porosity with a hypothetical solid material having the same properties of that of the cellular material. Since dynamics involves both elasticity and inertia, the Young's modulus E and the density ρ are the only parameters that need to be determined in order to define the equivalent continuum. This is achieved

by replacing E of the equivalent continuum by an effective value E^*, and ρ by ρ^*, the average density of the cellular structure. When Timoshenko shear correction is incorporated, the effective value of Poisson's ratio ν^* is used as the Poisson's ratio of the effective medium.

The r-th natural frequency of a cantilever beam in bending, made up of homogeneous isotropic medium is given by [73]

$$\omega_r = \frac{c_r^2}{L^2}\sqrt{\frac{EI}{\rho A}} \tag{2.12}$$

where I is the second moment of the cross sectional area, A is the cross-sectional area, L is the length and c_r is a constant that depends on the mode number r. c_r takes the values 1.875, 4.694, 7.855, 10.996, ..., $(2r-1)\pi/2$ [73]. The second moment of the area and the cross-sectional area of the effective beam are calculated from the overall dimensions of the cellular beam. Equation (2.12) is based on the Euler-Bernoulli beam theory. When shear is included in the model, the beam bending frequencies are given by [47]

$$\omega_r = \frac{1}{\gamma}\sqrt{\frac{(d_r^2 - e_r^2)E}{\rho L^2}} \tag{2.13}$$

where, $\gamma = \sqrt{2(1+\nu_s)/k_1}$, d_r and e_r are coefficients related by,

$$d_r = \frac{e_r s}{\gamma}\sqrt{\frac{1}{d_r^2 + s^2/\gamma^2}}. \tag{2.14}$$

s is the slenderness ratio defined as L/r, where, $r = I/A$, is the radius of gyration. The shear factor k_1 is determined based on the shape of the cross-section [17]. For rectangular beams, k_1 is calculated as follows,

$$k_1 = \frac{10(1+\nu_s)}{12 + 11\nu_s}. \tag{2.15}$$

The values of d_r and e_r are evaluated by solving the frequency equation for a fixed-free shear beam

$$(d^2 - e^2)de \sin d \sinh e + (d^4 + e^4)\cos d \cosh e + 2d^2e^2 = 0. \tag{2.16}$$

The finite element calculations will produce bending as well as axial modes of the overall beam out of a single model. This is because the degrees-of-freedom available in the model provide axial as well as transverse motion. The natural frequency of r-th mode of a rod in axial tension and compression is given by [73]

$$\omega_r = \frac{(2r-1)\pi}{2L}\sqrt{\frac{E}{\rho}}. \tag{2.17}$$

In this chapter, the applicability of the effective medium theory is examined for beams made of hexagonal and triangular cells. These two cases are considered because analytical expressions for the Young's modulus are available for them in the published literature. However, no such formula is available for beams having irregular cells (see figure 2.1). Hence, the eigenvalue problem (2.11) needs to be solved for the free vibration calculations of such structures. Bounds on the elastic properties such as Hashin-Shtrikman (HS) bounds [50] (based on the homogenisation theory) can be used for deducing bounds on the natural frequencies.

Two cases of the hexagonal cells are considered here: (i) when the lattice possesses a six-fold rotational symmetry, the hexagons are regular, and (ii) when the lattice possesses two fold symmetry and two mirror planes symmetry: the case of non-uniform hexagons. Figures 2.2 and 2.3 show typical lattices made up of regular hexagons. The geometry of a typical cell was shown in figure 1.2. The aspect ratio h/l and the cell angle θ define the shape of a cell. For regular hexagonal cells, h/l equals 1 and θ is 30^o. The area fraction of the solid depends on the ratio t/l in addition to h/l and θ.

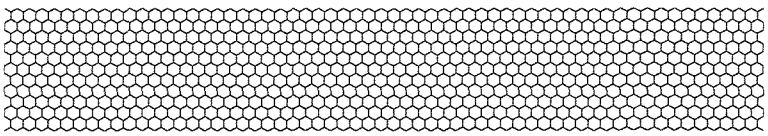

Figure 2.2: A lattice of regular hexagons. The length of the beam runs horizontally whereas the thickness runs vertically. This geometry is referred to as orientation 1 in the text.

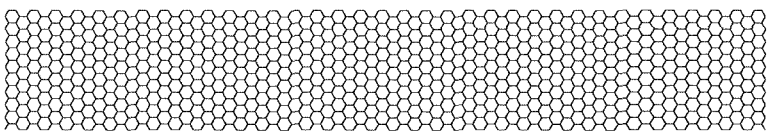

Figure 2.3: Another orientations of the hexagons in the lattice– orientation 2. Note that the hexagons are rotated by a right angle with respect to the orientation shown in figure 2.2. The length of the beam runs horizontally as before.

The expressions of the effective modulus of elasticity in a tension-compression mode of deformation are given by [34]

$$\frac{E_1^*}{E_s} = (t/l)^3 \frac{\cos\theta}{(h/l + \sin\theta)\sin^2\theta} \left[\frac{1}{1 + \cot^2\theta (t/l)^2} \right] \tag{2.18}$$

and

$$\frac{E_2^*}{E_s} = (t/l)^3 \frac{(h/l + \sin\theta)}{\cos^3\theta} \left[\frac{1}{1 + (\tan^2\theta + \frac{2(h/l)}{\cos^2\theta})(\frac{t}{l})^2} \right] \tag{2.19}$$

where, E_1^* is the effective modulus of elasticity of the solid having cells in orientation 1 and E_2^* is the effective modulus of elasticity of the solid having cells in orientation 2 (see figures 2.2 and 2.3). The stretching of the cell walls is included in the above expression in addition to cell wall bending. For regular hexagonal cells, substituting $h/l = 1$ and $\theta = 30^o$ in expressions (2.18) and (2.19) leads to $E_1^* = E_2^*$. The modulus of elasticity E^* can be calculated by using the expressions (2.18) or (2.19), depending upon the orientation of the cells as appropriate. The density of the equivalent continuum ρ^* is calculated using the standard expression for the cellular structures [90]

$$\rho^*/\rho_s = t \sum_i l_i/LD. \tag{2.20}$$

Solids made of non-uniform hexagons with $h/l \neq 1$ and $\theta \neq 30^o$ are in-plane orthotropic [34]. Consequently, structures made of such hexagons possess two Young's modulii E_1^* and E_2^*, in the two orthogonal directions 1 and 2 (see section 1.2.1). Next, we examine the validity of the *isotropic* effective medium theory applied for *orthotropic* cellular beams, when the Young's modulus is taken as that for the axial direction. Such a choice of Young's modulus is preferred when a beam bends transversely. This is because a fibre running parallel to the neutral axis is stretched or compressed axially during continuum beam-bending. We could treat a row of cells as a fibre provided that the dimensions of a cell in the transverse direction are small compared to the overall depth of the beam in the transverse direction.

The performance of the effective medium theory is studied for the statics problems first. It is assumed that the isotropic beam formula continues to hold even for cells that exhibit overall orthotropy. This means that when cells have orientation 1, E_2^* has no effect on the dynamics and when the cells have orientation 2, E_1^* is unimportant. It is one of the aims of this chapter to investigate these hypotheses and assess the accuracy of the approximation. The value of the effective Young's modulus E^* determined on the basis of the finite element results (2.4) is compared with that obtained using (2.18) or (2.19).

At the next step, the effective medium theory is applied for low frequency dynamics. The beam bending and rod extension formula are used for evaluating the natural frequencies of the beam made of regular hexagonal cells as appropriate. For dynamics, equations (2.18) or (2.19) and (2.20) are used to calculate the effective continuum prop-

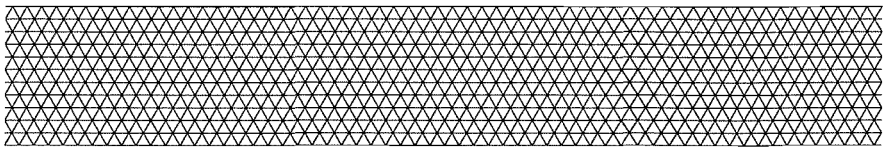

Figure 2.4: A beam made of equilateral triangles. Henceforth, this orientation is referred to as orientation 1.

erties, E^* and ρ^*, which, in turn, are used to calculate the free vibration frequencies according to equations (2.12) or (2.13) and (2.17). These continuum frequencies are compared with the finite element simulations.

In the case of a lattice made of triangular cells, the primary mode of strain energy storage is stretching-compression of the cell walls. Typical beams made of such cells are shown in figures 2.4 and 2.5 for two different orientations of the cells. The effective Young's modulus for tension-compression mode of deformation for lattice made of equilateral triangles having cell orientations 1 and 2 is given by Hunt [56]

$$\frac{E_1^*}{E_s} = \frac{E_2^*}{E_s} = 1.15\frac{t}{l}. \tag{2.21}$$

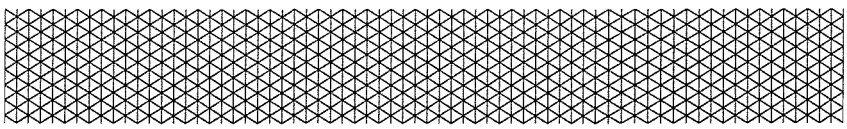

Figure 2.5: Another beam made of equilateral triangles, with the triangles are now oriented at a right angle with respect to the previous orientation. This orientation is referred to as orientation 2 in the text.

§2.4 Results and discussions

The results are presented in seven subsections. In section 2.4.1, results are presented for the transverse bending of beams made of regular hexagonal cells. Energy distribution

through the depth is studied in section 2.4.2. The case of orthotropic beams having hexagonal cells is presented in section 2.4.3. The statics of cellular beams made of triangular cells is presented in section 2.4.4. Free vibration of beams having regular hexagonal cells is taken up in section 2.4.5, followed by the case of non-uniform hexagonal cells in section 2.4.6. The dynamics of beam with triangular cells is undertaken in section 2.4.7. A Rayleigh's principle based method to calculate the fundamental frequency of a cantilever cellular beam is proposed in section 2.4.8 and numerical examples are given.

For all the models, the minimum number of rows of cells stacked vertically is kept as 10 in each case so that sufficient cells are present in the depth direction. The width perpendicular to the plane of the beam is taken as unity for all the models. The t/l ratio for each cell wall and the length/overall depth ratio for the cellular beam are kept greater than 10. This is to ensure that the whole beam as well as the cell walls behave as thin beams. The shear effects in the cell walls have been ignored due to thinness and because the deformed shape of each cell wall does not show rapid fluctuations for statics as well as for low frequency dynamics. It is assumed that all the cell walls are of uniform thickness. Displacements are assumed to be small so that a linear analysis is valid. The rotary inertia is neglected.

§2.4.1 Transverse bending of beams having regular hexagonal cells

Cantilever beams subjected to concentrated load at the free end are analysed here. The beam is fixed at its left end. Beams made of hexagonal cells having orientation 1 are considered first. The geometric data are presented in table 2.1. The L/D ratio of the beam is 13.41. Therefore, the beam is thin enough for Euler-Bernoulli beam theory to be valid. The t/l ratio for each cell wall is 1/20. All the cellular structures analysed in this dissertation are made of aluminum with the material properties as shown in table 2.1, unless mentioned otherwise.

A vertical load of 1 N is applied at a node close to the neutral axis. The displacement field calculated by solving equation (2.4) is shown in figure 2.6. The horizontal and the vertical displacement components of each node are extracted from the displacement vector and are plotted as arrows such that the length and the direction of an arrow represent the magnitude and direction of displacement at the relevant node. Figure 2.6 indicates that the vertical deflection gradually increases from left to right. The overall displacement pattern of the cellular beam looks similar to that of a homogeneous beam under transverse bending. When the same beam is analysed with tensile force being

Geometric data	
Length of the model L	2078.5 mm
Overall transverse depth of the model D	155.5 mm
Length of a vertical/inclined cell wall $h = l$	10 mm
Thickness of each cell wall t	0.5 mm
Number of cells in the horizontal direction	120
Number of rows of cells vertically stacked	10
Number of nodes	2651
Number of elements	3845
Material data	
Cell walls are made of aluminium	
Young's modulus E_s	70 GPa
Density ρ_s	2700 kg/m^3

Table 2.1: Data of a beam made of regular hexagonal cells having orientation 1.

Length of the model L	4640 mm
Overall transverse depth of the model D	355 mm
Length of a vertical/inclined cell wall $h = l$	10 mm
Thickness of each cell wall t	0.5 mm
Number of cells in the horizontal direction	310
Number of rows of cells vertically stacked	20
Number of nodes	13020
Number of elements	19199

Table 2.2: Geometric data of a beam made of regular hexagonal cells having orientation 2.

applied at the right boundary, the displacement field is calculated as in figure 2.7. The uniform stretching from left to right resembles that observed in a rod under tension.

The vertical displacement of the point of the application of the load, $\triangle_L$, as obtained from the finite element calculation is 0.4 mm. The Young's modulus E_b^* of the cellular beam is now calculated using the standard expression of a cantilever subjected to tip loading P [95]

$$E_b^* = PL^3/(3I\triangle_L). \tag{2.22}$$

The subscript 'b' indicates that this value is calculated from a numerical experiment involving beam bending. The value of E_b^* is calculated as 2.41×10^{-2} GPa. Because the beam is subjected to a concentrated load, there may be regions of localised deformation, however, it is not evident from figure 2.6. To eliminate this possible source of error, deflections were measured at five nodes on the neutral axis. The Young's modulus is

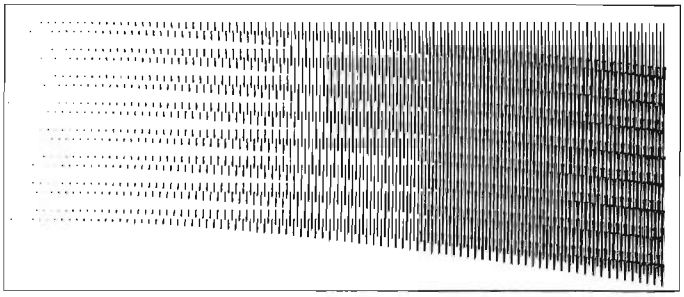

Figure 2.6: The displacement field of a cellular cantilever beam due to a vertical load acting at the free end. The deflected configuration resembles to that of a homogeneous beam.

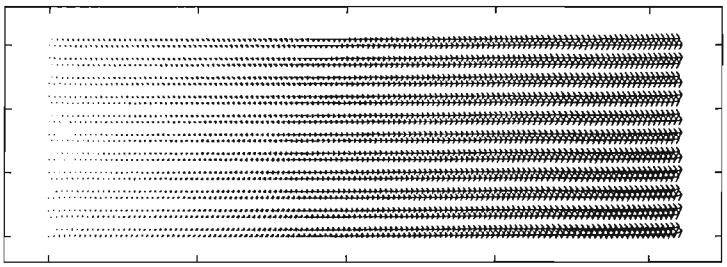

Figure 2.7: The displacement field of a cellular rod subjected to a tensile force at the free end.

also calculated from each deflection using the following expression [95]

$$E_b^* = PL^2(3L - s)/(6I\triangle) \tag{2.23}$$

where, s is the distance of the node from the fixed end and $\triangle$ is the corresponding vertical displacement. The average of the five values of E_b^* is found to be very close to the value calculated based on $\triangle_L$. This indicates that the effect of localised deformation is not so critical in this case.

The effective Young's modulus E_1^* is calculated using the infinite lattice expression (2.18) as 2.01×10^{-2} GPa. The ratio E_b^*/E_1^* is obtained as 1.21. Therefore, the modulus calculated from the bending experiment is about 21% higher than the modulus based on macroscopic tension-compression. When the size of the problem is increased from 120 × 10 (number of horizontal cells × number of vertical cells) to 240 × 20, the ratio E_b^*/E_1^* is reduced to 1.10. This results in a smaller cell size to the overall depth ratio. When a similar experiment is performed on a beam made of cells (310 × 20) having orientation 2, E_b^*/E_2^* is obtained as approximately equal to 1.0. The geometric data of the beam having cells in orientation 2 are presented in table 2.2. The number of cells

stacked vertically is kept 20 in this case. The close to unity value indicates that the effect of the cell size is not so pronounced for this orientation as opposed to orientation 1. The results of the two orientations indicate the importance of the presence of an appreciable number of cells in the model. The value of the Young's modulus as obtained from numerical experiments involving axial tension is found to be within 0.1% of the value for the infinite lattice for both the cell orientations.

§2.4.2 Energy distribution

The strain energy of each cell wall during deformation can be divided into two parts– (i) the contribution from the cell wall bending deformation, and (ii) the contribution from the stretching of the cell walls. For a piece of cellular matter having hexagonal cells, it is well known that the strain energy is mainly due to cell wall bending when the overall deformation is tension or compression at the bulk level [34]. Since beam bending (at the bulk level) is not a case of uniform strain field, it is not obvious if the mechanism of deformation dominates here too. When these two components of energy were separated in a numerical simulation of beam bending, it was found that 99.99% of the total energy can be attributed to the bending of cell walls. This confirms that the main mechanism of energy storage in cellular beams continues to be the bending of cell walls.

The distribution of the bending strain energy with the location of the cell walls is shown in figure 2.8. The cell wall numbering runs from left to right for the lowest level (that has only inclined members, see figure 2.2) first. Then it runs back from right to left covering cell walls of vertical orientation at the level just above the level already numbered. When we reach the left end, the inclined members are numbered from left to right at the next higher level and this procedure continues till we reach the top level having inclined member alone. This numbering is stored in an array and we will refer this as the index of cell walls. Therefore, this array stores information about two dimensional space in a single array with one index.

In figure 2.8 we plot the strain energy (as a percentage of the total strain energy of the structure) for each cell wall on the horizontal axis for the corresponding cell wall index on the vertical axis. This choice is deliberate since it captures the energy distribution through the thickness if we consider two cell wall indices separated by the number of cell walls in a row. Keeping the numbering scheme in the cell wall indices in mind, we now deduce the following from figure 2.8:

(i) The vertical cell walls store negligible amount of strain energy– the cell wall indices

correspond to the periodically placed short vertical lines in figure 2.8. This means that the vertical cell walls behave as rigid bodies– a fact previously known for a uniform strain fields as in uni-axial tension. In case of uniform strain field, the vertical cell walls translate away from each other. For beam bending deformation, they rotate with respect to each other.

(ii) For a particular axial location, the energy stored in the cell walls close to the centre line of the overall bulk is less compared to that in the cell walls away from the centre line. This conforms with the trend that one would expect for a continuum beam. The trend for strain energy density (strain energy per unit volume) for continuum beam bending shows a parabolic variation through the thickness. This variation is approximately observed for the case of cellular beam too– if we joined the peaks of each 'spike' in figure 2.8, we obtain a trend that is approximately parabolic.

(iii) When we move left to right (i.e. from the fixed end to the loaded end) the strain energy in the inclined members reduces. This conforms with the continuum behaviour where the curvature of the neutral axis is maximum at the fixed end and zero at the loaded end. Keeping in mind that the strain energy density for continuum beams is proportional to the square of the curvature, the trend *within* each 'spike' in figure 2.8 shows a continuum behaviour of the cellular beam.

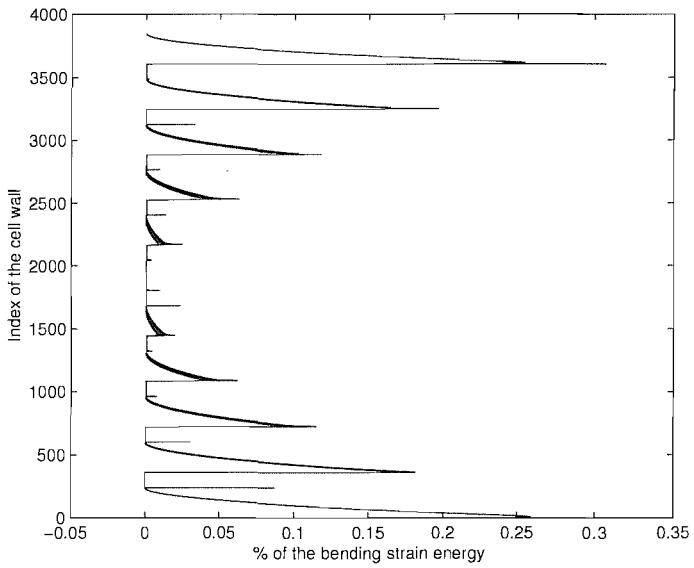

Figure 2.8: Distribution of the bending strain energy among the cell walls due to transverse bending of a cantilever beam subjected to tip load. The beam is made of regular hexagonal cells having orientation 1. The bending energy accounts for 99.99% of the total strain energy.

§2.4.3 Statics of beams made of hexagonal cells exhibiting orthotropy

Non-uniform hexagonal cells are generated next by changing h/l or θ or both. The loading and the boundary conditions are kept the same as before. Table 2.3 shows the ratios of E_b^*/E_1^* and E_b^*/E_2^* as calculated for four samples with various combinations of h/l and θ. All the models possess 20 rows of cells stacked vertically.

Orientation	Geometric data	E_2^*/E_1^*	E_b^*/E_1^*	E_b^*/E_2^*
Orientation 1	$h/l = 2$ $\theta = 45^o$	14.38	1.15	0.08
Orientation 1	$h/l = 0.5$ $\theta = 60^o$	23.40	1.17	0.05
Orientation 2	$h/l = 2$ $\theta = 45^o$	14.65	13.62	0.93
Orientation 2	$h/l = 0.5$ $\theta = 60^o$	22.37	23.94	1.07

Table 2.3: The ratio E_b^*/E_1^* and E_b^*/E_2^* for beams made of hexagonal cells exhibiting orthotropy.

Table 2.3 shows the ratio of the Young's modulus obtained from the bending experiments and the value of the Young's modulus in the axial and the transverse direction for an infinite lattice. When the cells are having orientation 1 (see figure 2.2), E_1^* represents the Young's modulus in the axial direction; E_2^* i.e. the modulus in the transverse direction is much higher than E_1^* (see column 3 of the first two rows). For beams made of such cells, the ratio of the elastic modulus obtained from the bending experiments and E_1^* is close to 1 (the last but one column of the first two rows of table 2.3), whereas absurd values of the ratios are obtained when the Young's modulus in the transverse direction E_2^* is used (see the last column of the same two rows). Similarly, for the cells having orientation 2 (see figure 2.3), E_1^* is much less than E_2^* (see column 3 of the last two rows). Yet the ratios are again close to 1 (the last column of the last two rows) when calculated based on E_2^*. In spite of the strong orthotropy, the ratio of the elastic modulus obtained from the bending experiments and the elastic modulus in the axial direction is close to 1 for all models. This suggests that the effect of the Young's modulus in the transverse direction is not so significant for bending of orthotropic beams.

§2.4.4 Static deflection of cellular beams having triangular cells

The geometric data used to generate the cellular beams having triangular cells are presented in tables 2.4 and 2.5 for the two orientations. The displacement field due to a

tip load on a cantilever beam made of cells with orientation 1 is shown in figure 2.9. The pattern generally resembles that of a homogeneous beam. When the value of the effective modulus was calculated from the static response of the beam made of cells with orientation 1, the ratio of the Young's modulus obtained from a bending numerical experiment to the analytical value for a lattice of infinite extent was found to be 1.23. This ratio is found to be 0.97 for cells having orientation 2. These ratios approach unity as the number of vertically stacked rows of cells is increased. This means that when the cell dimensions are very small compared to the overall depth of the beam D, the effective medium theory becomes increasingly more accurate.

When the strain energy distribution in the cell walls is examined, the pattern is very similar to that obtained for beams having hexagonal cells (not shown here). Again, the cell walls away from the centre line store more strain energy than those close to the centre line. However, for the beam with cell orientation 1, the inclined members store negligible strain energy. The total strain energy is mainly contributed by the stretching-compression of cell walls (up to 99.99%).

Length of the model L	1495 mm
Overall depth in the transverse direction D	121 mm
Length of each cell wall l	10 mm
Thickness of each cell wall t	0.5 mm
Number of cells in the horizontal direction	150
Number of rows of cells vertically stacked	13
Number of nodes	2265
Number of elements	6436

Table 2.4: Geometric data of the beam made of triangular cells having orientation 1.

Length of the model L	1290 mm
Overall depth in the transverse direction D	115 mm
Length of each cell wall l	10 mm
Thickness of each cell wall t	0.5 mm
Number of cells in the horizontal direction	150
Number of rows of cells vertically stacked	11
Number of nodes	2265
Number of elements	6436

Table 2.5: Geometric data of the beam made of triangular cells having orientation 2.

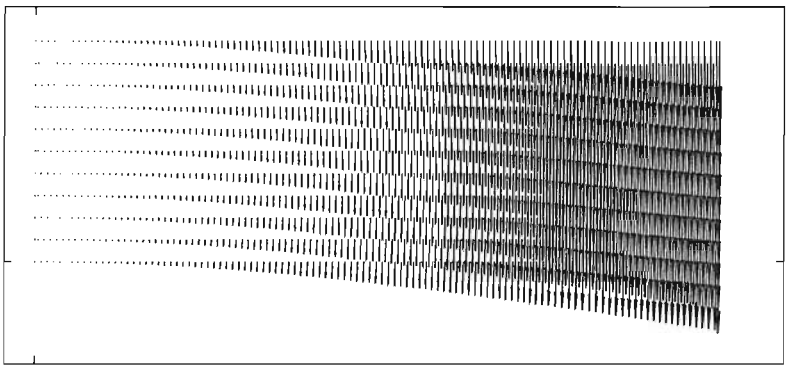

Figure 2.9: The displacement field of a cantilever beam made of triangles when a vertical load acts at the free end. The deflected configuration resembles to that of a homogeneous beam.

§2.4.5 Free vibration of beams made of regular hexagonal cells

The mode shapes and the natural frequencies for beams made of regular hexagonal cells shown in figures 2.2 and 2.3 are presented now. These results are calculated using the full scale finite element model and are compared with those obtained based on the effective medium assumption. When the cell walls are modelled using three node elements, the frequencies are calculated within 0.1% (up to the 25th mode) of the values when only two node elements were used. This shows the convergence of the model for low order modes. Hence, two node beam elements are used here. Two beams made of cells having orientation 1 and 2 were generated with 1560 and 2076 cells respectively.

The number of rows of horizontally running cells is 12 for both the models. The cell wall length is kept the same for both the orientations considered. This means that the overall length of the beams is different for the two models in order to keep the L/D ratio of both the beams at about 12.5. The calculations have been carried out for t/l as 0.05 for both the orientations. The corresponding value of area fraction as calculated from equation (2.20) is 0.0577. Usually, the area fraction of foams considered in practice ranges in the range 0.03 to 0.33 [34].

The mode shapes are shown first for identifying the type of mode which will enable us to use (2.12) or (2.17) accordingly. The mode shapes for the first ten modes are obtained from the corresponding eigenvectors. The eigenvector $\mathbf{u}_r$ in equation (2.11) contains information about the two displacement components and the rotation of each node of the finite element model. Again, the displacement components were extracted from the eigenvectors and plotted using arrows of length proportional to the magnitude

of displacement. Typical plots are shown in figures 2.10 to 2.19. These modes are plotted for the beam made of cells in orientation 1. The mode shapes of the beam made of cells in orientation 2 resemble those of beams having cells in orientation 1 and are, therefore not shown.

The first mode of vibration (figure 2.10) resembles the first flexural mode of a solid cantilever beam. This pattern does not exhibit any node for the motion of the overall structure. The displacements increase from zero at the fixed end to a maximum at the free end. This variation is not linear, instead it closely mimics the trend for a continuum beam. The axial displacements are negligibly small indicating that this mode is primarily a bending mode as far the macroscopic behaviour is concerned.

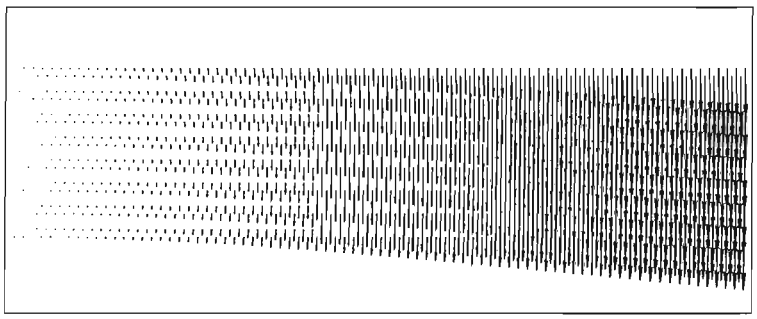

Figure 2.10: The first mode of vibration of the beam made of regular hexagonal cells. Note the resemblance in the displacement pattern with those commonly found in fixed-free continuum beams.

The second and the third modes are shown in figures 2.11 and 2.12 exhibiting one and two nodes respectively. The displacement field shows an interesting pattern. Note the eddy-like structures near the regions where nodes are expected in an effective continuum. The flow pattern around the node of the second mode (figure 2.12) has a counter-clockwise sense. The arrows shrink to a point as we come closer to the nodal point. On the left of this node we have vertically downward displacement whereas on the right of this node we have upward displacement. The displacement field in the direction of the axis of the cantilever is such that in the vicinity of this node the displacements point from right to left at the top; whereas they point from left to right at the bottom. These two observations combined, conform with the counter-clockwise flow pattern. In contrast, when we encounter a node such that vertically upward displacements are on its left and vertically downward displacements are on its right, the flow will have a clockwise sense. This is observed from the node closest to the free end of the third mode (see figure 2.12). As was the case with the first mode, the second and the third modes also do not show

any appreciable displacement along the axis of the cantilever beam.

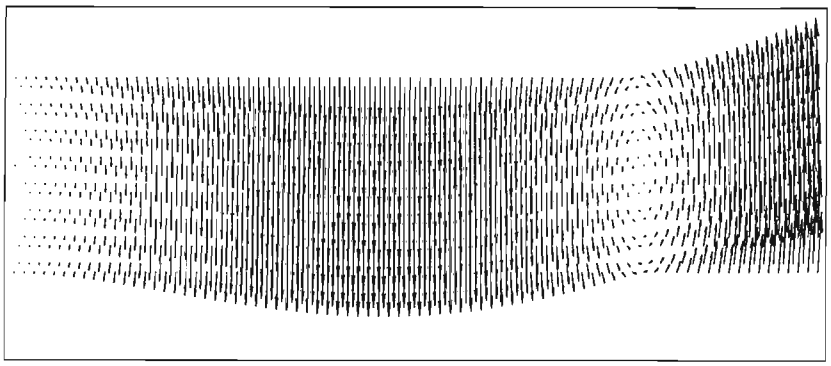

Figure 2.11: The second mode of vibration. Note the existence of a 'node' roughly where a node for a beam made up of continuum would be found.

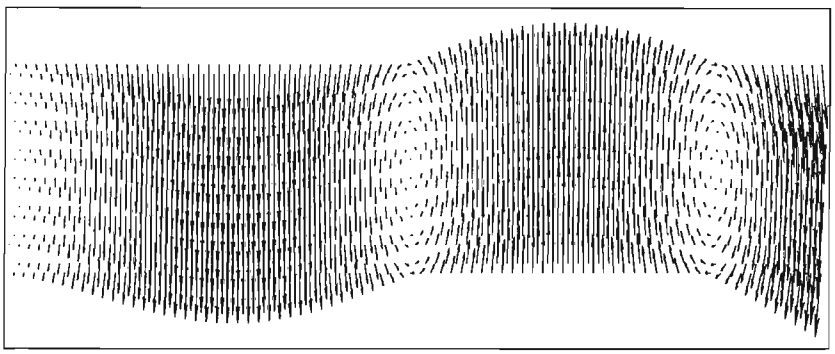

Figure 2.12: The third mode of vibration. Again this mode resembles the third continuum mode of a beam. There are two 'nodes' at the macroscopic level.

The fourth mode shows displacements primarily along the axis of the beam (see figure 2.13). This behaviour is not beam-like. Instead it resembles the first axial mode of a continuum rod in tension and compression. The overall *fifth* mode is again a flexural mode (see figure 2.14) and it corresponds to the *fourth* mode in the series of the bending modes. Further, the sixth, eighth and the ninth modes are flexural modes (see figures 2.15, 2.17 and 2.18). The sixth mode is the fifth in the series of the flexural modes and, contain four nodes. Similarly, the eighth and the ninth mode are the sixth and the seventh in the bending series.

The seventh and the tenth modes are the second and the third modes in the series of axial modes (see figures 2.16 and 2.19). In the case of the seventh mode, a zone of zero displacement can be seen. The 'eddy-like motion' in the nodal zone is not observed

in this case as was found in the case of the bending modes. Instead, the arrows in the central portion meet at the nodes from the opposite directions. The remaining arrows on the top portion move vertically upwards, whereas the arrows on the bottom portion move vertically downwards. The overall tenth mode possesses two nodes of axial motion.

The nodal positions from the fixed end are normalised with respect to the overall length, and presented in table 2.6. The positions of the nodes shown in figures 2.10 to 2.14, are estimated from the plots by noting the reversal of direction of the vertical component of the arrows. The table indicates that the overall mode shapes are very close to the mode shapes of homogeneous slender beams.

Mode no.	Medium	1st node	2nd node	3rd node
1	Continuum beam [49]	–	–	–
	Cellular beam	–	–	–
2	Continuum beam [49]	0.78	–	–
	Cellular beam	0.77	–	–
3	Continuum beam [49]	0.50	0.87	–
	Cellular beam	0.49	0.84	–
4	Continuum beam [49]	–	–	–
	Cellular beam	–	–	–
5	Continuum beam [49]	0.36	0.64	0.91
	Cellular beam	0.34	0.63	0.88

Table 2.6: Comparison of the position of the nodes between the cellular beam and a solid beam.

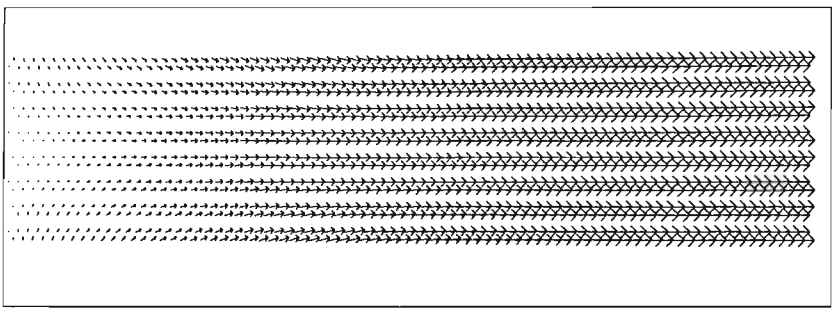

Figure 2.13: The fourth mode of vibration. This mode, unlike the previous three as in figures 2.10 through to 2.12, shows axial mode of vibration at the macroscopic level.

The results for the first ten frequencies are presented next. As pointed out earlier, the first three modes and the fifth mode are primarily bending modes. Therefore, equations (2.12) and (2.13) are applicable. Similarly, the frequencies are calculated for the sixth, eighth and the ninth modes. Equation (2.17) is used to calculate the fourth frequency

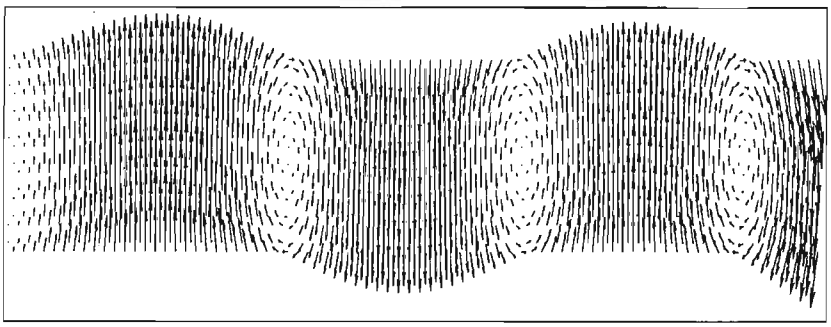

Figure 2.14: The fifth mode of vibration. There are three nodes as expected. The distance between two nodes now approaches the depth, but still the overall beam-like behaviour is remarkable.

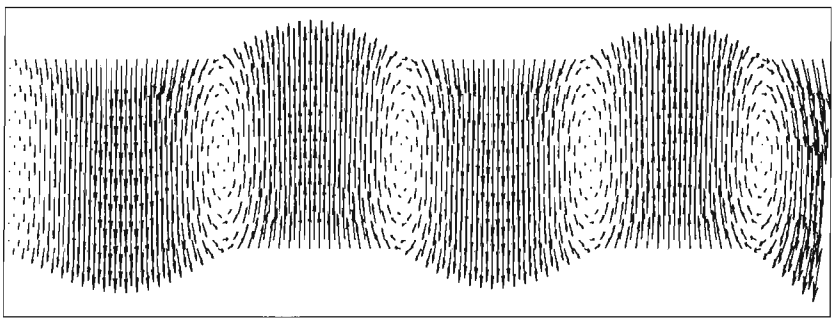

Figure 2.15: The sixth mode of vibration. This mode is the fifth in the series of flexural modes. It has four nodes as expected.

since this mode corresponds to the first axial mode. The same equation is used for the seventh and the tenth mode as well because they are the second and the third in the series of axial modes respectively. The continuum relationships use equations (2.18) or (2.19) for the effective modulus. The density of the effective medium is calculated from equation (2.20). The value of the effective Poisson's ratio for the Timoshenko shear correction is used as 1 for both the cell orientations [34] and equation (2.13) is used to determine the flexural frequencies for the effective continuum.

Figure 2.20 shows comparisons of the values of the first ten natural frequencies obtained from the finite element analysis and the continuum relationship for orientations 1 and 2 respectively. The horizontal axis represents the mode number. The cells in both the orientations are regular hexagons ($h/l = 1$ and $\theta = 30^o$) having the value of $t/l = 0.05$. The frequencies are normalised to obtain the fundamental frequency as unity in each case. This means that the modal frequencies for each set of calculations are divided by the fundamental frequency in that set. Similarly, the axial frequencies are

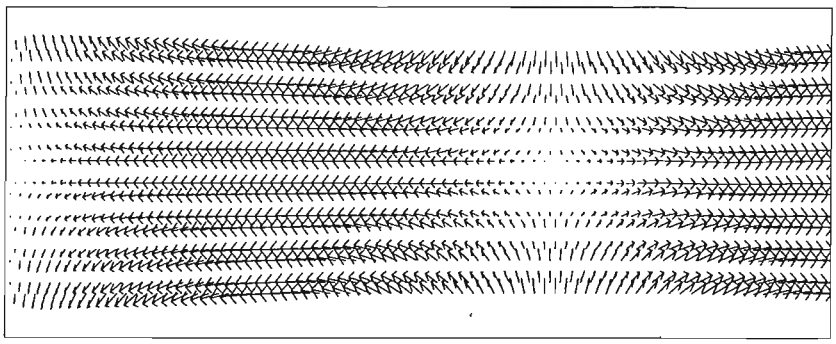

Figure 2.16: The seventh mode of vibration. It is the second mode in the axial vibration series.

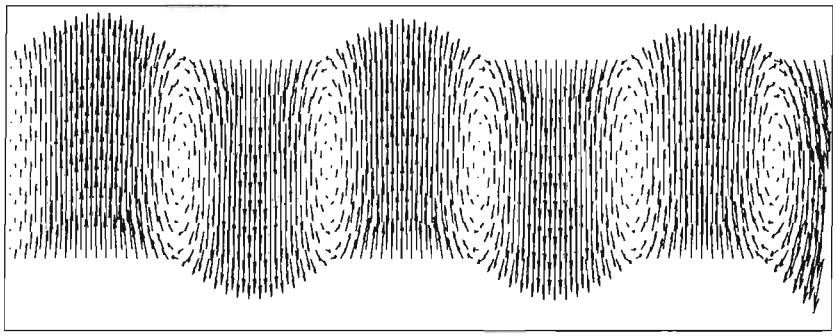

Figure 2.17: The eighth mode of vibration. This mode is the sixth in the series of flexural modes. There are five nodes as expected.

normalised with respect to the first axial frequency as computed from the finite element model. The flexural modes are shown in the top figure of 2.20. The figure shows that the frequencies obtained from the finite element analysis and the continuum relationship for both the orientations are close for the first few modes. This match starts deteriorating with increase in the mode number.

The fundamental natural frequencies obtained from the finite element simulations for orientations 1 and 2 are 2.25 Hz and 1.73 Hz respectively. The difference in the fundamental frequency is attributed to the different values of the mass per unit length for the cantilever. This is because the number of cells accommodated within the same area is different for the two orientations. The ratio of the number of cells for the first orientation to that for the second orientation is about 0.75 which is approximately equal to the ratio of mass per unit length $\rho^* A$ for the two cases. Thus the frequencies must be in the ratio of the reciprocal of the square root of $\rho^* A$ i.e. approximately equal to 1:0.87 because the effective modulus is the same for the two directions. The computationally

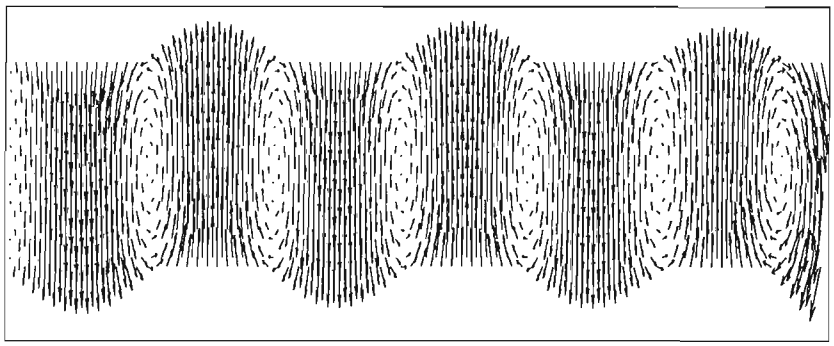

Figure 2.18: The ninth mode of vibration. It is the seventh mode in bending series. Note the presence of six nodes.

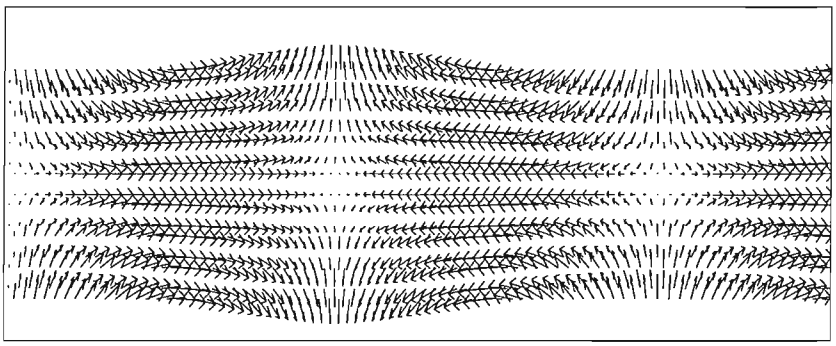

Figure 2.19: The tenth mode of vibration. It is the the third mode in axial vibration series.

obtained ratio of 1:0.77. The difference may be attributed to the fact that the cellular structures are not homogeneous and possibly the shear correction required for the two orientations are different.

The Euler-Bernoulli beam theory does not account for the effect of shear. As the mode number increases, shear induces more flexibility and thus, reduces the natural frequencies. When Timoshenko correction is used via equation (2.13), the discrepancy between the finite element results and the effective medium calculations is reduced; yet there is a progressive deviation of the frequencies of the cellular beam with mode number (see figure 2.20). The deviation increases as the wavelength approaches the overall depth of the sample. At this stage, a cellular beam starts behaving as a two-dimensional solid rather than a one-dimensional beam. Consequently, the effective medium theory based on Euler-Bernoulli or Timoshenko beam theory is no longer applicable. We will look into the dynamic behaviour in the higher frequency range in the next chapter.

Comparisons of the natural frequencies for the axial modes are made in the bottom

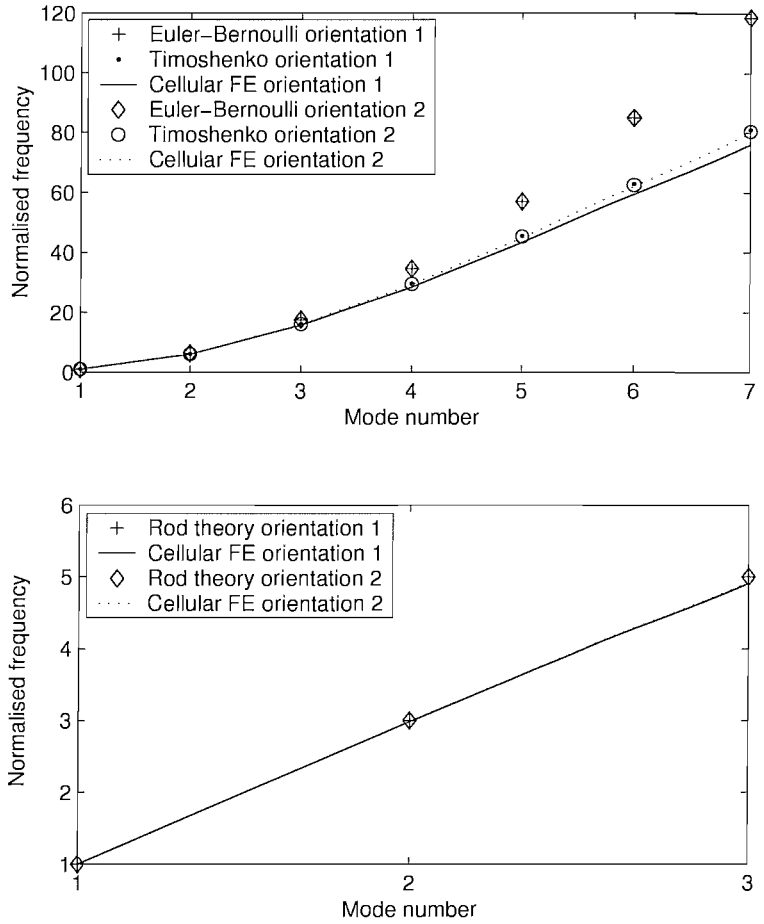

Figure 2.20: Comparison of the natural frequencies of the cellular beams as calculated by the finite element analysis with those from the effective medium theories. The top half and the bottom half show the frequencies associated with the flexural and the axial modes respectively. The beams are made of regular hexagonal cells ($h/l = 1$ and $\theta = 30^o$) of orientation 1 and 2 (see figures 2.2 and 2.3). The value of t/l is 0.05.

figure of 2.20. The overall agreement between the finite element computations and the rod theory (equation 2.17) is excellent. The third frequency deviates less than 3% from the values predicted by the effective medium theory for both the orientations. The difference for the axial modes is much less compared to that for the flexural modes. The reasons for this are three fold. Firstly, the Young's modulus used for the effective medium theory exactly represents the stretching-compression behaviour. Secondly, only the first three modes in the axial series are considered. Larger discrepancy is expected for higher modes because the one-dimensional rod theory is not valid. Finally, there is no shear correction for axial motion unlike the case of beam bending.

The values of the fundamental frequencies in the axial motion are 40.69 Hz and 33.88 Hz respectively corresponding to orientation 1 and orientation 2 of the cells. Again, this

discrepancy is due to the differences in the mass per unit length $\rho^* A$ for the two models. The ratio of the frequencies (finite element)is 1:0.83 which is close to the continuum value equal to 1:0.87.

Instead of using equations (2.18) and (2.19) of Gibson and Ashby, bounds on the Young's modulus based on the homogenisation theory can be used. Torquato et al. [96] applied Hashin-Shrikman (HS) bounds [50] for the cellular structures (mentioned in section 1.2.1). The HS upper bounds for the Young's modulus in the low density asymptotic limit ($\rho^*/\rho_s \ll 1$) becomes,

$$\frac{E^*}{E_s} \leq \frac{1}{3}\frac{\rho^*}{\rho_s}. \tag{2.24}$$

In the case of the two models described in this section, the maximum value of E^* calculated from the above expression is 1.34 GPa. This value can be used for deducing the upper bound of the natural frequency using (2.12) or (2.17). However, the value of the Young's modulus 1.34 GPa is much greater than 0.02 GPa, evaluated using (2.18) or (2.19). Three point bounds proposed by Hyun and Torquato [57] may be used for a better estimate of the modulus in this case.

§2.4.6 Vibration of hexagonal cells exhibiting overall orthotropy

It was remarked in section 2.3.2 that the Young's modulii for two orthogonal directions are equal for regular hexagons (i.e. $h = l$ and $\theta = 30^o$). When hexagons do not have all sides equal and/or the included angle is not 120^o but mirror symmetry about two planes is preserved, then we expect an overall orthotropy of the medium. Numerical results for cellular beams made up of such cells for two cases are described next.

The first orthotropic model beam is made of cells of orientation 1 ($h/l = 1.5$ and $\theta = 45^o$), whereas the second is made of cells of orientation 2 ($h/l = 0.5$ and $\theta = 60^o$). The L/D ratio of the two beams are 12.23 and 12.48 respectively. The geometric parameters for the two beam, are as given in tables 2.7 and 2.8.

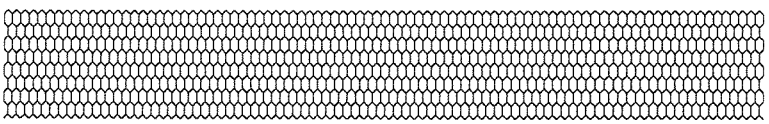

Figure 2.21: A cellular beam made of non-uniform hexagonal cells ($h/l = 1.5$ and $\theta = 45^o$) having orientation 1. The beam runs horizontally as before.

Figure 2.21 shows a part of the orthotropic beam made of cells having orientation 1. The overall mode-shapes resemble to those of the beams made of uniform hexagons

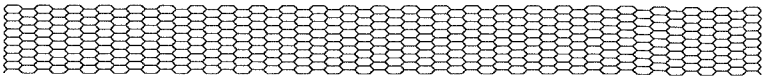

Figure 2.22: A cellular beam made of non-uniform hexagonal cells ($h/l = 0.5$ and $\theta = 60^o$) having orientation 2.

Length of the model L	2969 mm
Overall transverse depth of the model D	249.8 mm
Length of an inclined cell wall l	10 mm
Length of a vertical cell wall h	15 mm
Thickness of each cell wall t	0.5 mm
Number of cells in the horizontal direction	210
Number of rows of cells vertically stacked	11
Number of nodes	5052
Number of elements	7355

Table 2.7: Geometric data of the beam made of non-uniform hexagonal cells of orientation 1.

Length of the model L	1497.6 mm
Overall transverse depth of the model D	125 mm
Length of an inclined cell wall l	10 mm
Length of a horizontal cell wall h	5 mm
Thickness of a cell wall t	0.5 mm
Number of cells in the horizontal direction	109
Number of rows of cells vertically stacked	12
Number of nodes	2860
Number of elements	4167

Table 2.8: Geometric data of the beam made of non-uniform hexagonal cells of orientation 2.

and, therefore, the mode-shapes are not shown here. The frequencies as calculated from the finite element simulations and those based on equations (2.12) through to (2.17) and equations (2.18) through to equation (2.20) are compared in figure (2.23). The normalisation is carried out in the same way as was done before for the regular hexagons. We observe that the frequencies calculated based on E^* of axial stretching match well with the finite element results for the first few modes: a discrepancy of about 10% is observed up to the fifth mode. The deviation increases to 20% for the seventh mode of the bending series. In contrast, frequencies predicted based on E^* in the transverse direction start deviating rapidly with mode number. The first frequency predicted based on E^* in the transverse direction is 2.85 times of that calculated by the finite element

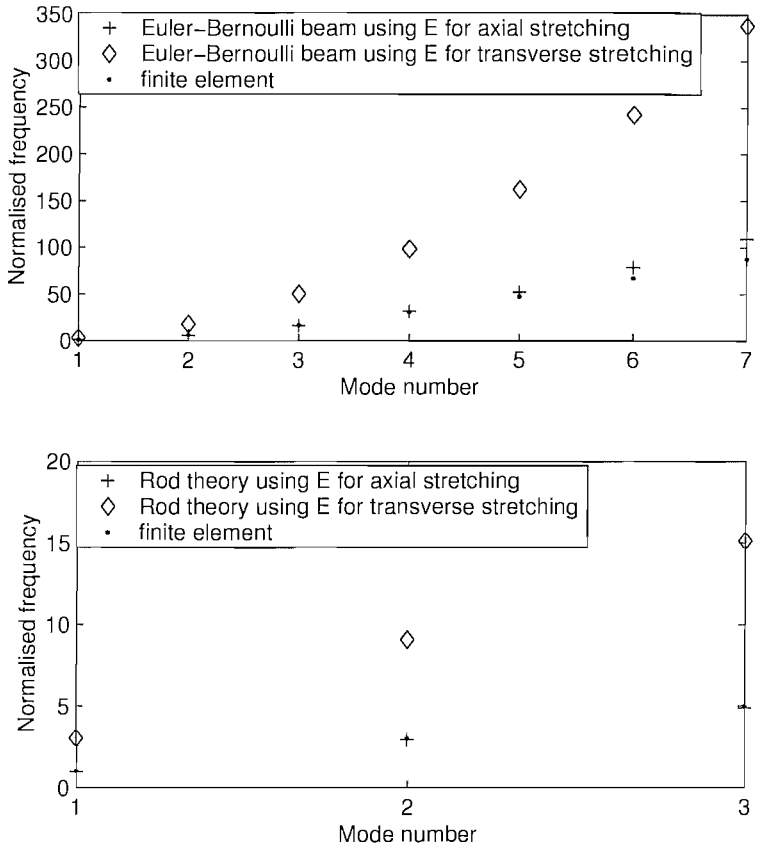

Figure 2.23: Comparison of the natural frequencies of orthotropic cellular beam as calculated by the finite element analysis and the isotropic effective medium theory. The beam is made of non-uniform hexagonal cells ($h/l = 1.5$ and $\theta = 45^o$) of orientation 1 (see figure 2.21). Value of t/l is 0.05. Frequencies corresponding to both the axial and the bending modes are presented.

simulation (this is not so clear on the wide range of the vertical scale in the top figure of 2.23).

The fact that there is a good agreement for low frequencies when we use modulus in the axial direction for transverse motion indicates that orthotropy due to cell shape has little effect on the dynamic behaviour at least for the lower modes. As the mode number increases, the deformations in the transverse direction would have increasingly important role and they are affected by the Young's modulus in the *transverse* direction: a fact not accommodated by the isotropic beam formula 2.12. Further, the cellular medium itself will be another source of discrepancy, similar to the case of the isotropic cells. The axial modes (see bottom figure of 2.23) also show good agreement for the calculations based on E^* of axial stretching. The deviation is less than 3% up to the third mode.

The next model has cells in the second orientation but there is no in-plane isotropy now (see figure 2.22). Results on the lines of figure 2.23 are presented in figure 2.24.

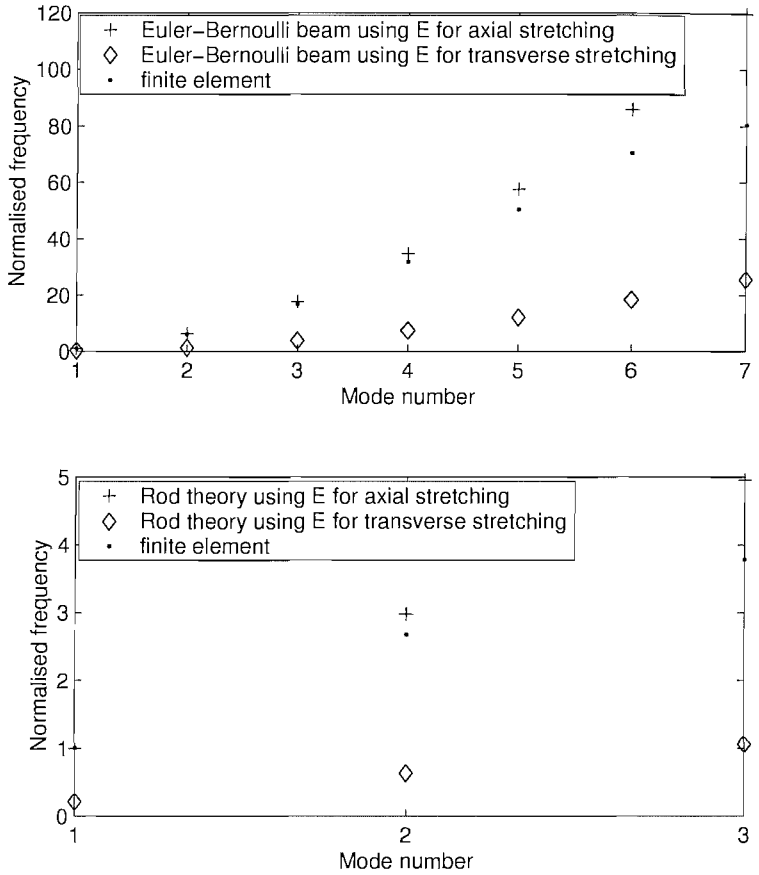

Figure 2.24: Comparison of the natural frequencies of an orthotropic cellular beam as calculated by the finite element analysis and the isotropic effective medium theory. The beam is made of non-uniform hexagonal cells ($h/l = 0.5$ and $\theta = 60^o$) having orientation 2 (see figure 2.22). The value of t/l is 0.05. Frequencies associated with the flexural and the axial modes are presented.

As before, the top figure refers to the flexural modes whereas the bottom figure refers to the axial modes. Once again, the calculations for this orthortropic beam match well with the finite element simulations when the elastic properties in the axial direction are used in the Euler-Bernoulli calculations. The error increases from 12% for the fifth mode to 33% for the seventh mode. In contrast, the frequencies calculated on the basis of the transverse Young's modulus are quite erroneous. The first predicted frequency is 80% less than the corresponding value obtained from simulations. We expect a lower predicted frequency from this calculation because $E^*_{\text{axial}} > E^*_{\text{transverse}}$ for the orientation of cells as in figure 2.24. The axial modes also do not match very well except the first mode. The third mode is 60% off. Frequency calculations based on E^* in the transverse direction show larger error.

§2.4.7 Vibration of beams made of triangular cells

Two models of cellular beams having triangular cells in two different orientations (as in figures 2.4 and 2.5) were studied. Ten modes were extracted from the finite element model and the mode types were identified by examining the mode shapes. Out of the first ten modes, seven modes were essentially beam bending modes and the remaining three modes were primarily axial modes. The frequencies were normalised in each case as explained previously. The results are plotted in figure 2.25. The top figure shows the variation of the natural frequencies with the mode number in the bending series. The bottom figure shows the three axial vibration frequencies with the mode number in the overall extension-compression series.

In case of the modes in the bending series, the finite element simulations are compared with the analytically obtained frequencies on the basis of (i) the effective modulus expression for infinite lattices [56], and (ii) the frequency equations (2.12) or (2.13) for the Euler-Bernoulli beam bending formula or the Timoshenko beam bending formula. When the Euler-Bernoulli beam bending theory is used, the first three modes show excellent agreement with the numerically obtained values. This agreement deteriorates with mode number and errors of about 50% are observed for the seventh bending mode. When shear correction is incorporated, the agreement is substantially improved– the error now comes down to the order of 10%. This implies that the disagreement between the simulation results and the Euler-Bernoulli calculations based of effective medium values taken for an infinite lattice is largely due to the inadequacy in the Euler-Bernoulli theory rather than any cellular features in the problem.

The three axial modes show excellent agreement for cells in both the orientations. This confirms the validity of the effective medium theory for low order axial modes.

§2.4.8 A method for approximately calculating the fundamental frequency

The deformed shape of a fixed-free beam under tip loading resembles the first mode of vibration (see figures 2.6 and 2.10). This suggests that the static response vector could be used as a trial vector in a Rayleigh's quotient approximation. Therefore, the cellular beam was first analysed under a vertical static load that acts at the node on the neutral axis of the free-end. The stiffness matrix $\mathbf{K}$ and the force vector $\mathbf{f}$ were generated as before. The static equilibrium leads to a set of algebraic equations $\mathbf{Kq} = \mathbf{f}$, in the form of equation (2.4). This equation was solved to calculate the response vector $\mathbf{q}$.

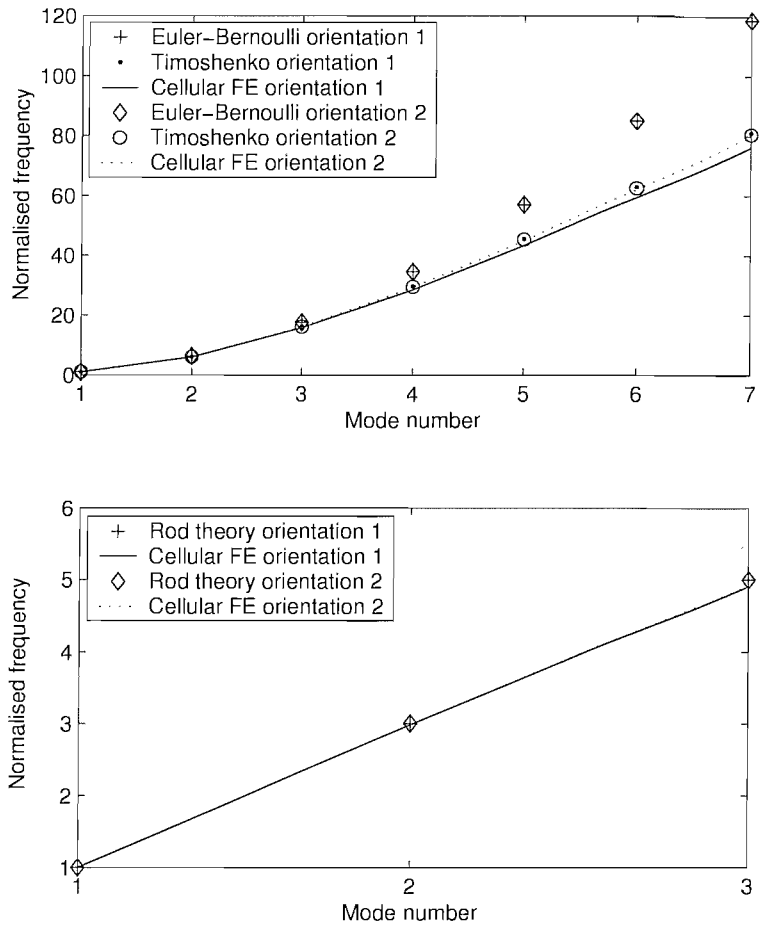

Figure 2.25: The natural frequencies of beams made of triangular cells (cell orientations 1 and 2) compared with those of an effective medium. The top half and the bottom half show the frequencies associated with the flexural and the axial modes respectively. The value of t/l is 0.05.

At this stage, the information about the translational as well as the rotational degrees-of-freedom under static loading are available through the vector $\mathbf{q}$. The stiffness matrix $\mathbf{K}$ and the inertia matrix $\mathbf{M}$ incorporate all the details about the topology, geometry and the properties of the individual cell walls. Computationally, the most expensive step is solving the eigenproblem, equation (2.11), when $\mathbf{K}$ and $\mathbf{M}$ are large. Usually, assembly is a relatively inexpensive process. Therefore, a Rayleigh's quotient based approximation to estimate the fundamental frequency of the overall structure without the solution of the eigenproblem (2.11) is proposed. Since the static deflection shape resembles the first mode of vibration, the value of the Rayleigh's quotient will be a good approximation for the first eigenvalue of (2.11) when the static deflection shape $\mathbf{q}$ is used as a trial vector, i.e.

$$\lambda_1 \approx R = \frac{\mathbf{q}^T\mathbf{K}\mathbf{q}}{\mathbf{q}^T\mathbf{M}\mathbf{q}}. \tag{2.25}$$

Two samples, each made of regular hexagonal cells of orientation 1 and 2 (used before) and another sample made of non-uniform hexagonal cells (orientation 2, $h/l = 0.5$ and $\theta = 60^o$) were analysed. All the models have the same values of t/l as 0.01. The errors with respect to the full scale eigencalculations (2.11) for the three cases is about 1.6%, 1.5% and 1.7% respectively for the three cases. The solution of equation (2.4) is substantially cheaper than solving the eigenvalue problem of equation (2.11). For example, for the first model, the total floating point operations required for the approximate method is less than 1% of those required for extracting one eigenvalue.

§2.5 Conclusions

Since analytical results for the effective medium properties for an infinite hexagonal and triangular lattice exist, the applicability of these values to predict the response of a beam was examined. Six cases of cell lattice were considered: (i) regular hexagons in orientation 1, (ii) regular hexagons in orientation 2, (iii) hexagons with two-fold rotational symmetry in orientation 1, (iv) hexagons with two-fold rotational symmetry in orientation 2, (v) triangles in orientation 1 and (vi) triangles in orientation 2. In all the cases, the response calculated from the finite element simulations matched closely with the values predicted by the use of the effective elastic properties for an infinite lattice. The match improves with the increase in the number of rows of cells running along the length of the beam. This is explained by the fact that the theoretical values are based on a uniform strain field and this situation in the beam bending problem is realised more accurately when the cell size is infinitesimally small compared to the depth of the beam in the transverse direction.

When the hexagons are not regular and exhibit overall orthotropy, the response predictions are accurate when the properties corresponding to stretching in the axial direction are used. There is a gross mismatch in the simulation results and the theoretical predictions if the properties in the transverse direction are used. This can be explained because cells extend or compress in the *axial* direction for beam bending problems.

The strain energy distribution in the cell walls was studied for the cellular beam bending problem. In all the cases, the pattern broadly resembles the distribution in the continuum counterparts. For example, the strain energy density varies parabolically across the depth and cell walls store greater energy along the length in areas where large value of curvature of the centre line is observed.

The fundamental natural frequency was fairly accurately predicted on the basis of

effective medium calculations in all the cases. The agreement with the predictions based on the effective medium values is good for the first few modes. However, this progressively deteriorates with mode number. The agreement is improved when Timoshenko shear correction is introduced, as expected. The finite element model produces results for the overall axial vibration modes in addition to the bending modes. These modes are very accurately predicted when effective medium calculations are preformed. This is because the axial modes possess a strain field that resembles the uniform strain in the infinite lattice calculations. In addition, unlike the beam bending problem, there is no source of error due to Timoshenko shear for axial deformation.

Guided by the observation that the static deflection shapes for cantilever beams under tip load resemble the first mode of bending vibration, a Rayleigh's quotient based approximation was proposed. The fundamental frequency was calculated within an accuracy of 2% with a computational expense less than 1% of that of the eigenvalue extraction.

Chapter 3

Statistical analysis of modal spacing and progressive departure from the continuum behaviour

§3.1 Introduction

It was concluded in the previous chapter that cellular structures exhibit a continuum behaviour for low frequency dynamics. The effective elasticity can be approximately taken as the effective properties for static calculations. However, it was noted that this changes with the increase in the mode number. In this chapter this departure from the continuum behaviour is investigated systematically. Trends in modal density (number of modes over a band of frequency) for the continuum are compared with those arising out of cellular matter of the same external dimensions.

In order to get an insight into the statistical distribution of modes, a large number of modes need to be evaluated. This raises the issue of convergence in the calculations. When a small fraction of the total number of degree-of-freedom available in the model is used, the calculations are found to be satisfactory and mesh refinement in not required. In most cases considered in this chapter, when about 10% of the total number of degrees-of-freedom are accepted, the accuracy of calculations of the highest mode used in the statistical analysis is found to be satisfactory.

In the previous chapter, only the first few modes were examined in the light of an effective medium theory. The Euler-Bernoulli beam theory or improvements over it (e.g. shear correction due to Timoshenko) were adequate to capture the behaviour of

the cellular beam when the external shape of the continuum beam is the same as the cellular beam. When the statistics of modal distribution is to be studied, the continuum needs to be modelled more carefully for comparisons with the modal distribution arising from the cellular structure. Even the most sophisticated beam theory may be inadequate for this. Therefore, modal density has been calculated from cantilever beams modelled as plane stress problem in this chapter.

We were restricted to the hexagonal and the triangular cells in the previous chapter when we needed to compare the dynamics results with those calculated from effective elasticity because analytical expressions are available for a limited class of cell geometries. This restriction is removed in this chapter and, therefore, in addition to the beams made of triangular, and hexagonal cells, those made of square and irregular cells are also considered.

§3.2 Numerical experiments using the finite element method

Again, finite element models of cantilever cellular beams are considered. While shear in cell walls has negligible effect on the accuracy of the first few modes (about 100 modes), the refined model is used in this chapter. When the mesh is refined by by inserting an extra internal node for elements representing a cell wall, the frequency calculations improve slightly but they are always within 3% of the values for the coarse mesh (up to about 800th mode). Shear in the cell wall is modelled here using a quadratic Timoshenko beam element. The L/D ratio of the beam is taken as 1/12. The overall dimensions of beams made of various topologies are kept the same for comparison purposes. The area fraction (the same as the volume fraction if the depth is is constant) is also kept the same for all the models.

The plane stress problem is generated by filling the porosity with a hypothetical material having the density and the effective Young's modulus equal to those of the cellular structure. The effective Young' modulus E^* is calculated from the *fundamental* frequency ω_1 of the cellular beam. The Young's modulus is evaluated using beam formula [73]

$$E^* = \omega_1^2 (L/c_1)^4 \rho^* A/I \tag{3.1}$$

with c_1=1.875 since the fundamental frequency is always flexural. The Poisson's ratio values are taken from the literature when known; and it is set at 1/3 for irregular cells. The continuum beam is modelled using the 8 noded plane stress element (CPS8) in ABAQUS [2].

§3.3 Results and discussions

The overall length $L = 600$ mm and the depth in the transverse direction $D = 50$ mm give the L/D ratio as 1/12. The width B of the beam is taken as unity. The area fraction of the cellular beam is chosen as 0.044, which is kept the same for all the models.

§3.3.1 Modal distribution for beams made of triangular cells

Beams made of triangular cells having orientation 1 (see figure 2.4) are analysed first. The geometrical data are given in table 3.1. The t/l ratio is 1/81. Therefore, modelling each cell wall as Euler-Bernoulli beam is valid. The Young's modulus E^* of the hypothetical continuum is evaluated using equation (3.1), based on the fundamental frequency of the cellular beam. The value of the Poisson's ratio ν^* is taken as 1/3 [56]. Similarly, the mass density ρ^* is calculated using (2.20). We recall that structures made of uniform triangular cells are isotropic (see section 1.2.1). Therefore, E^*, ν^* and ρ^* completely define the properties of the continuum beam. The natural frequencies of the solid beam are now obtained solving the eigenvalue problem (2.11). All the frequencies are then normalised with respect to the fundamental frequency.

Length of the model L	600 mm
Overall depth in the transverse direction D	50 mm
Length of each cell wall	5.25 mm
(except the ovehanging cell walls at the free end)	
Length of the overhanging cell walls	2.63 mm
Thickness of each cell wall t	0.065 mm
Number of nodes	1392
Number of elements	3899

Table 3.1: Geometric data for the beam made of equilateral triangles having orientation 1 (see figure 2.4).

Figure 3.1 shows comparisons of the normalised cellular beam frequencies with those of a continuum of the same external dimensions. The values of the first 800 frequencies are plotted. The mode number scale is divided into two parts: the low mode number end spans the first 30 modes (the top figure), whereas the high mode number end shows the remaining modes (the bottom figure). This is deliberately done to present the distribution with different resolutions. These modes represents about 5% of the total number of modes (15873) available in the model. Therefore, convergence of modes is not an issue here.

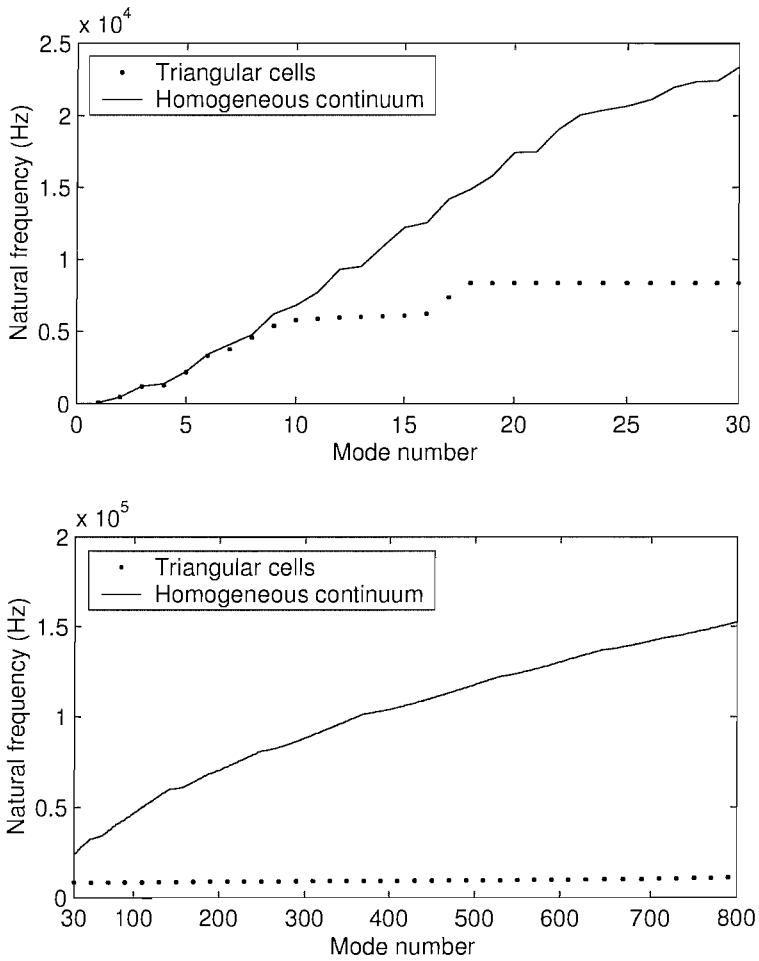

Figure 3.1: Comparisons of the natural frequencies of a beam made of triangular cells with those of an equivalent continuum. The first few frequencies of the cellular beam are very close to those of the continuum. Later, the frequency curve of cellular beam becomes close to the horizontal indicating small increase in frequency per mode i.e. very high modal density.

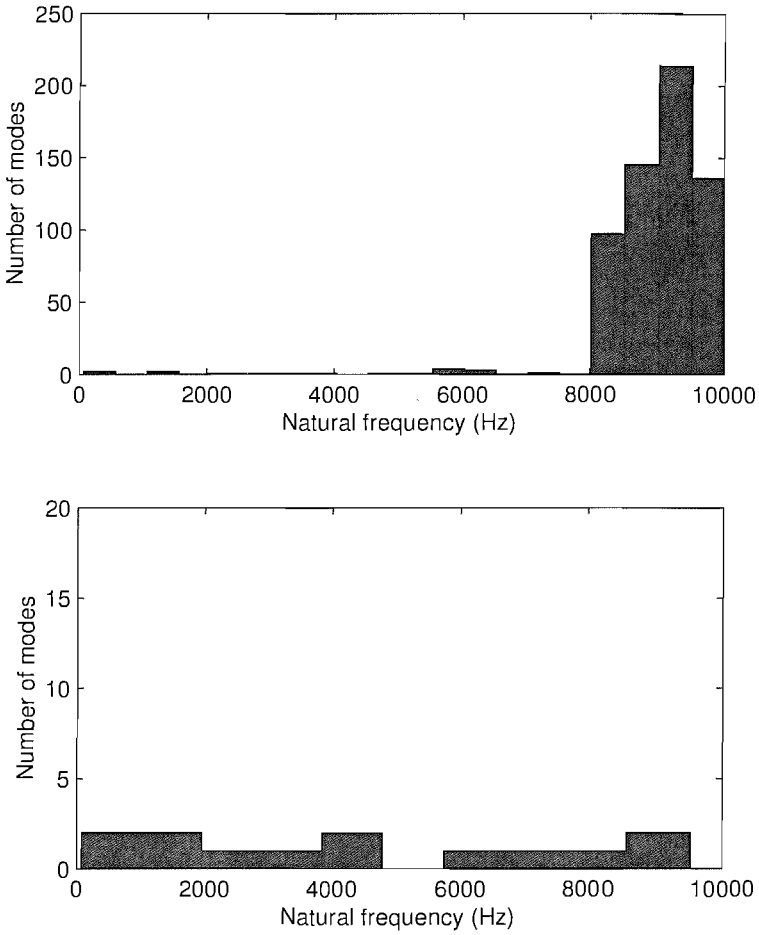

Figure 3.2: The top figure is the modal density plot of a beam made of triangular cells, whereas the bottom figure is the that for a continuum. Note that for triangular cells, 592 modes appear between 8 kHz and 10 kHz. This shows a sudden decrease in the modal separation. In contrast, the continuum has only 13 modes in the same frequency band.

The plot in figure 3.1 shows three identifiable regions. The first few frequencies of the cellular beam are very close to those of the plane stress continuum. For example, the eighth and the tenth modal frequencies are lower than the corresponding frequencies of the continuum by 8% and 18% respectively. The discrepancy between the values obtained for the cellular beam and those from the plane stress problem increases gradually with mode number. The curve for the cellular beam increasingly falls *below* that for the continuum. This indicates that the frequency spacing for the cellular beam shrinks when compared to the continuum counterpart. Therefore, the modal density for the cellular medium grows relative to a continuum of the same shape and size. This regime of modal distribution is followed by a regime of extremely high modal density as indicated by the near horizontal line.

Let us introduce a third length scale l_d corresponding to the depth D of the sample. The other two length scales, l_s and l_c, were introduced in the previous chapter. Now, the whole frequency regime is roughly divided into three regions. When the wavelength is greater than l_d, the frequencies belong to region 1. In this frequency band, the wavelength may be equal to or less than l_s. Structures made of cellular material approximately behave as those made of continua with some effective elastic properties in this frequency band. On the other extreme, for the frequency band associated with short wavelengths comparable or less than l_c (region 3), continuum behaviour breaks down and the modal density is remarkably high compared to a structure of the same external dimensions but made up of continuum. The transition regime (region 2) between region 1 and region 3 is characterised by wavelengths in the range of l_d and l_c.

The cellular beam frequencies show marked deviation from those of the homogeneous continuum when the wavelength approaches the depth of the sample l_d. At this stage, the one-dimensional cellular beam starts behaving as a two-dimensional solid. The cellular frequencies are now lower than the corresponding continuum ones. Hence, the cellular modes are more closely spaced as compared to those of the continuum. This results in an increase in the modal density in zone 2. Wavelengths in this regime are equal to or less than l_d, but greater than the cell dimension l_c.

The gradual 'softening' of the cellular beam with mode number along with the sudden increase in the modal density can be explained on the basis of the microstructure. Structures made of continua possess extended modes in the sense that all the parts of the structure contribute to the energy expressions. On the other hand, cellular structures progressively exhibit localised modes at high mode numbers. This leads to a crowding of modes in a narrow band of frequency known as the passband. In the present context, region 3 on the mode number scale (the bottom figure in 3.1) represent the local resonance of the individual cell walls. Prior to this extreme situation, there is a transition region between the effective medium regime and the cell wall resonance regime. This behaviour is very unlike a continuum and we will explore this further with other cell geometries.

The abrupt increase in the modal density can be clearly seen in a plot showing the distribution of modes. The histogram of the number of modes in the selected bands of frequency is shown in figure 3.2. A distribution of a total of 609 modes has been shown as a function of frequency. Note the last four frequency bins in which there is a sudden rise in the number of modes. There are only 17 modes up to 8 kHz and the remaining

592 modes appear between 8 kHz and 10 kHz. In contrast, there are only 13 modes within the same frequency band in the case of the equivalent continuum (see figure 3.2). The type of the modes appearing in the frequency band beyond 8 kHz will be explored next.

It is well known that the mechanics of triangular lattices is dominated by cell wall stretching as opposed to cell wall bending (as in hexagonal lattices). While this is true for most statics problems, the story is incomplete for the case of dynamics. If the cell walls have to resonate locally, this motion must be dominated by bending deformations. The natural frequencies due to the stretching mechanism of deformation are independent of the cell wall thickness (both stiffness and inertia increase linearly with thickness), whereas the bending dominated modes show a linear variation with thickness (stiffness $\sim$ thickness^3 and inertia $\sim$ thickness, hence the ratio $\sim$ thickness^2 and therefore frequency $\sim$ thickness). A convenient way to broadly distinguish the mode type, therefore, is to change the cell wall thickness systematically and observe the change in the modal frequencies. The results of this are presented in figure 3.3. Each marker type in the figure refers to a particular cell wall thickness. If the modes corresponding to the (approximately) horizontally running group of markers did correspond to cell wall resonance, then the level of these horizontal lines must be a measure of the cell wall resonance frequency in each case. As can be seen from the figure, the level of these horizontally running markers is in fact proportional to the cell wall thickness confirming that the mechanism of strain energy storage in the band is cell wall bending. There are a large number of modes having approximately the same natural frequency because for each overall mode, a different cell wall may resonate. In principle, the number of cell wall resonance modes should be equal to the number of the cell walls.

The markers on the initial rising part of the modal frequency curve in each case do not show a strong dependence on thickness, which confirms that the low order modes (the extended modes) are cell wall extension dominated when the lattice is made of triangular cells. This independence of thickness is pronounced for the first ten modes beyond which the transition regime comes into play.

An approximate estimation for the cell wall resonance frequency

If cell walls resonated as isolated structures, one could determine the frequency of this oscillation. In practice, the ends of a cell wall are connected to the rest of the lattice and there is no easy way of determining the stiffness of a lattice analytically. However, the

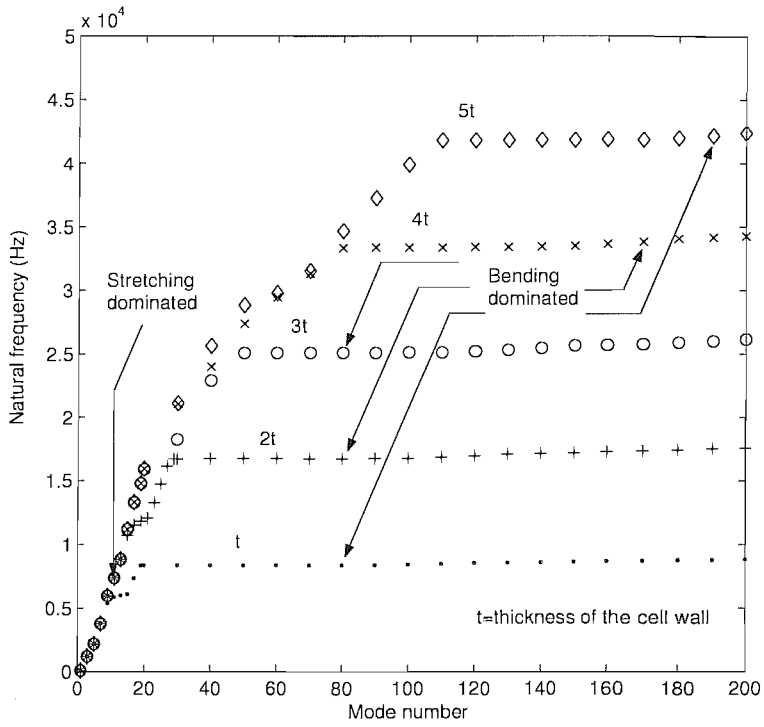

Figure 3.3: The natural frequency vs mode number plot for various thicknesses of the cell wall of the beam made of triangular cells. The plot indicates that at the lower mode number, modes are independent of thickness (hence stretching dominated) whereas the high mode number modes have frequency $\approx$ thickness (hence cell wall bending dominated).

bounds on the cell wall resonance can be obtained rather easily. Since the ends of a cell wall are connected elastically to the rest of the lattice, the stiffness offered by the lattice could be represented by effective springs. In the extreme case of the lattice offering no flexibility, the ends could be modelled as clamped. This frequency must be the upper bound for the cell wall resonance frequency because clamped beam has least freedom– applying Rayleigh's theorem on systems with constraints, it follows that the greatest frequency is that of a beam with both ends clamped. When calculated for the cell wall parameter used in the simulations, this frequency is calculated as 12.3 kHz. Therefore, the cell wall resonance frequency for the network of beams must be less than 12.3 kHz.

Encouraged by the calculations on the bounds, a model of a pinned-pinned isolated cell wall was considered because it represents the ideal end condition of a member in a truss. The resonant frequency is calculated as 5419 Hz, which is much less than the frequency of 8360 Hz where bending dominated modes appear in figure 3.2. This showed the need of a more realistic model. Since the ends of each cell wall possess three degrees-of-freedom in a plane (two translations and one rotation), a model for the individual cell

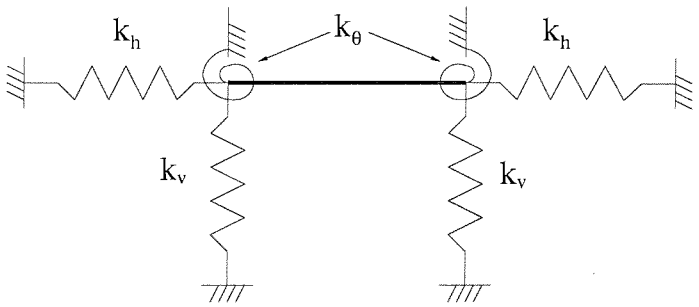

Figure 3.4: Model of an isolated cell wall. The end connections with its neighbours are replaced by vertical k_v, horizontal k_h and torsional springs k_{theta}.

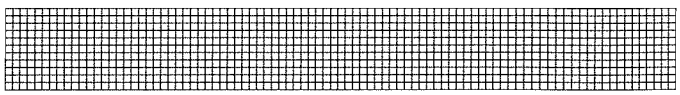

Figure 3.5: A cellular beam made of square cells.

wall is presented in figure 3.4. Note that this model is valid only for calculations of the cell wall resonance frequency. A vertical spring k_v, a horizontal spring k_h, and a rotational spring k_θ account for the stiffness at the ends. Since it is very difficult to have an estimate for these stiffnesses analytically, these stiffnesses were determined computationally by removing a cell wall from the overall cellular beam model and applying forces or moment appropriately. The values of k_h, k_v and k_θ were numerically calculated as 1.29×10^8 N/m, 1.16×10^6 N/m and 5.80 N.m/rad respectively. The fundamental frequency of the isolated cell wall is now obtained as 8014 Hz.

§3.3.2 Modal distribution for beams made of square cells

A cellular beam made of square cells (see figure 3.5) is studied next. The geometric properties are presented in table 3.2. The t/l ratio of each member is 1/50. Note the value of t here is not the same as the case of the triangular cells. This is to ensure that the area fraction for the two models remains the same. The natural frequencies and the mode shapes of the cellular structure are calculated by solving the eigenvalue problem (2.11) as before. The Young's modulus E^* is calculated from the numerically evaluated fundamental frequency. The E^* value in this case is different from that calculated in the case of the triangular cells which can be attributed to the difference in the topology of the lattice.

Length of the model L	600 mm
Overall depth in the transverse direction D	50 mm
Length of each cell wall l	4.5 mm
Thickness of each cell wall t	0.09 mm
Number of nodes	1608
Number of elements	3070

Table 3.2: Geometric data for the beam shown in figure 3.5.

The frequencies of the cellular beam having square cells are compared with those of an isotropic plane stress beam in figure 3.6. Again, the continuum properties are chosen such that the fundamental frequency is matched. Unlike the case of the beam with triangular cells, the deviations are significant even for low mode numbers. The reason for this discrepancy lies in the fact that the effective continuum is not isotropic for a square lattice but it is orthotropic.

There are three cases of the cellular beam in the results plotted in figure 3.6. All the three cases of the cellular beam shown in figure 3.6: (i) using data in table 3.2 when the cell walls are modelled as Euler-Bernoulli beams, (ii) same as the first case except that the cell walls model includes shear correction, and (iii) using all data in table 3.2 except the thickness of the cell walls which is doubled. The three cases exhibit a common feature– there are three identifiable regions on the mode number scale. The first regime is characterised by low frequency continuum modes. When the cell wall thickness is doubled, the frequency is approximately doubled (note the approximately doubled slope of the line through the origin). This is in contrast with the behaviour for beams made of triangular cells. Since frequency $\sim$ thickness, it follows that even the lowest modes are bending dominated. This is expected for the square topology of cell wall connections. A closer look at the mode shape reveals that some of the modes are *thickness-shear modes*. A typical thickness-shear mode is plotted in figure 3.7. Depending on the sign of the deformation in a group of cell walls belonging to a row, a thickness-shear mode is obtained. Such modes are commonly found in the dynamics of crystal plates/beams. Since there are only 12 horizontally running rows of cell walls, the total number of thickness-shear modes would also be equal to 12 provided the sign of axial displacement does not change along the length. However, the modes observed do show this sign change in many cases accounting for a number of thickness-shear modes. The lack of thickness-shear modes for triangular cells can be attributed to the high stiffness of the triangular lattice to shear deformations.

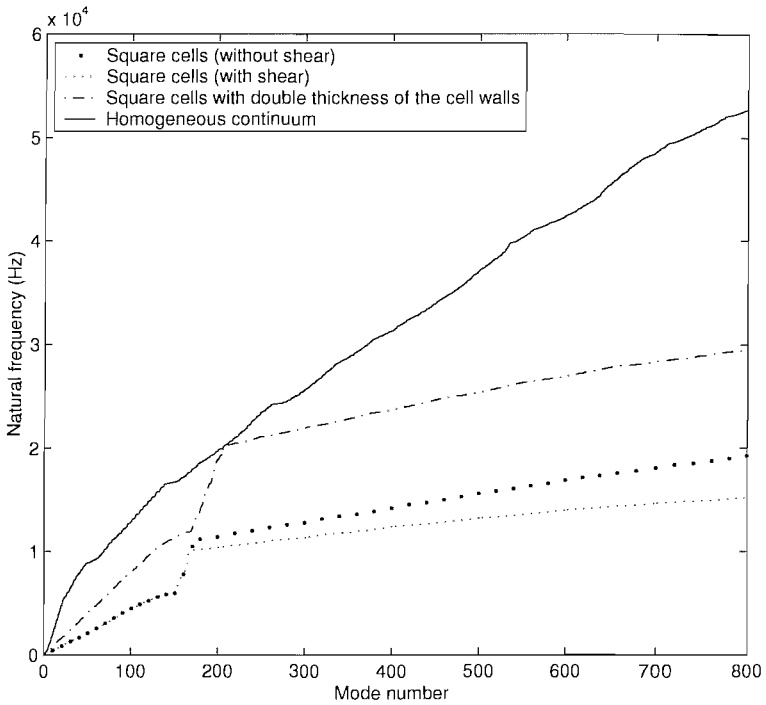

Figure 3.6: Comparisons of the natural frequencies of structure made of square cells with those of continuum whose properties are chosen to match the fundamental frequency.

In the second region on the mode number scale (spanning 17 modes starting mode number 151 up to and including mode number 167), the natural frequency trend is found to be on the up-slope. This means increased modal separation and a fall in modal density. Again this behaviour is not in agreement with that for beams made of triangular cells. The modes in this region are thickness-shear modes coupled with axial deformation. A typical such mode is plotted in figure 3.8. The increase in the modal separation is perhaps attributed to the high stiffness of the square cells in the axial direction.

The final regime at the right end of each curve for shows a relatively small slope indicating a high modal density. These modes can be attributed to cell wall resonance. Unlike the case of cellular beams with triangular cells, the frequency variation with mode number is less flat. This means a relatively high modal separation and a relatively low modal density. The reason for this difference lies in a relatively strong coupling between the cell walls in case of square lattice as compared to the triangular lattice. In the case of the triangular lattice, the cell walls can be approximately imagined to be isolated from the adjacent neighbours when cells wall bending resonance takes place.

The modal frequency curve, for the plane stress problem with properties chosen to match the fundamental frequency, is the steepest curve in figure (3.6) (the solid line).

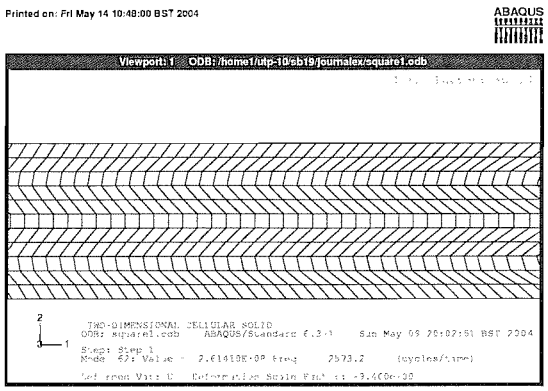

Figure 3.7: A portion of the cellular beam showing thickness-shear mode of vibration. This is the overall 62nd mode.

When the modal separation is compared with that of a homogeneous beam , it can be seen that the cellular beam exhibits a progressively reduced modal separation (i.e. an increase in modal density). This observation is in tune with our previous remark regarding the case of the beams made of triangular cells. The reason again is the presence of a large number of localised modes for cellular structures (equal to the number of cell walls if the couping were infinitesimally weak) as opposed to the homogeneous beam for which the modes continue to be extended even for relatively high mode numbers.

The histograms of modes are shown in figure 3.9. The top figure corresponds to the cellular beam whereas the bottom figure refers to a homogeneous isotropic counterpart. Note the sudden rise in modal density around the frequency associated with cell wall resonance.

§3.3.3 Modal distribution for beams made of hexagonal cells

Beams made of regular hexagonal cells (in orientation 1, see figure 2.2) are analysed next. The geometric data of the beam are given in table 3.3. The t/l ratio for the cell walls is 1/27. Figure 3.10 shows the comparison of the frequencies of the beam

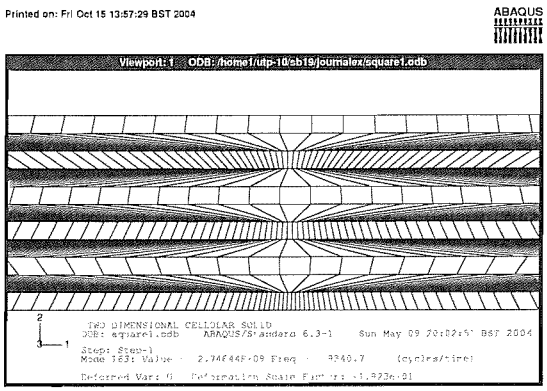

Figure 3.8: A portion of the cellular beam showing thickness-shear mode coupled with axial mode. This is the overall 163rd mode.

made of hexagonal cells with a continuum beam with properties chosen to match the fundamental frequency. Again, the mode number scale is divided into two parts to show the low mode number end and the high mode number end with different resolutions. Lattices made of regular hexagonal cells are known to exhibit isotropy. The plot shows that the cellular beam frequencies agree with those of the homogeneous beam for low mode numbers indicating the validity of the equivalent isotropic continuum model in this regime. The 0 to 1 kHz band contains 16 and 14 modes for the cellular and the homogeneous beams respectively.

Length of the model L	600 mm
Overall depth in the transverse direction D	50 mm
Length of each cell wall l	3.05 mm
Thickness of the cell walls t	0.11 mm
Number of nodes	2748
Number of elements	3995

Table 3.3: The geometric data for the beam made of regular hexagonal cells.

The discrepancy between modal frequencies for the cellular beam and those for the

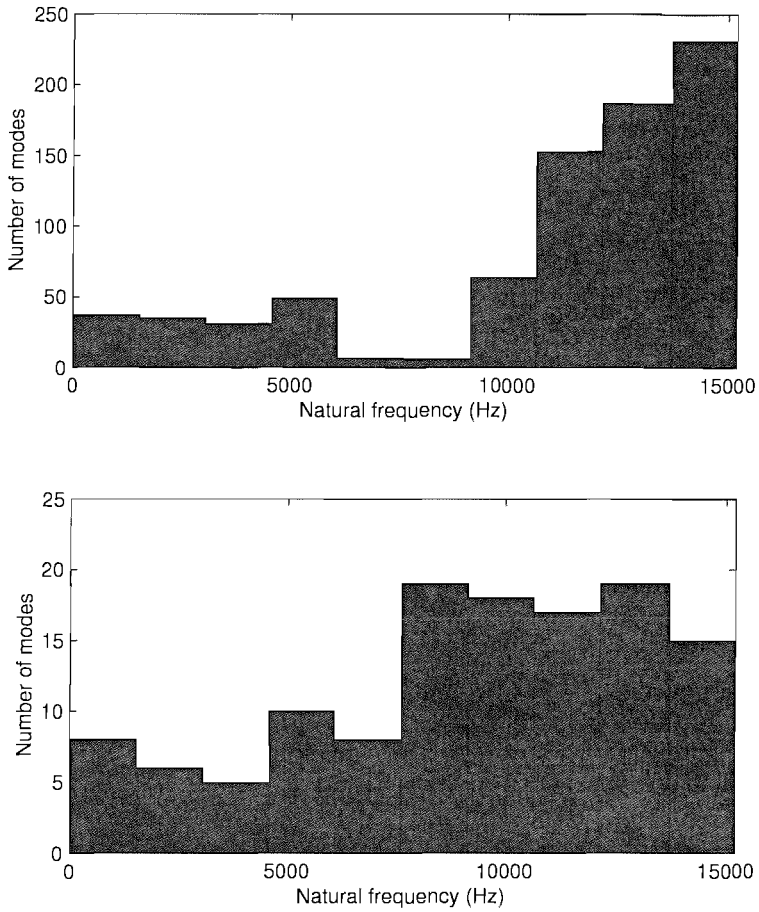

Figure 3.9: Comparisons of the modal density plot for the square cells and the continuum for the first 800 modes. A sudden increase in the modal density is observed in the case of the square cells in the regime of cell wall resonance.

homogeneous beam increases with mode number. There are no identifiable bands for frequency that could be associated with a change in the mechanism of deformation (unlike, for example, the case of triangular cells when the low frequency modes were cell wall stretching dominated whereas the cell wall resonance is bending dominated; or the case of square calls in which the thickness shear modes have a characteristic band of frequency). Therefore, the departure from the continuum behaviour is gradual in case of the hexagonal lattice.

The trend of modal separation can be observed in the plot for modal density (see figure 3.11). The increase in the modal density with mode number is much more pronounced for the cellular model than that for the the continuum beam having the fundamental frequency matched. The total number of modes appearing in the 0 to 10 kHz band is 961 and 476 for the cellular beam and the continuum beam respectively.

When the thickness of the cell walls is doubled, all the frequencies are approximately

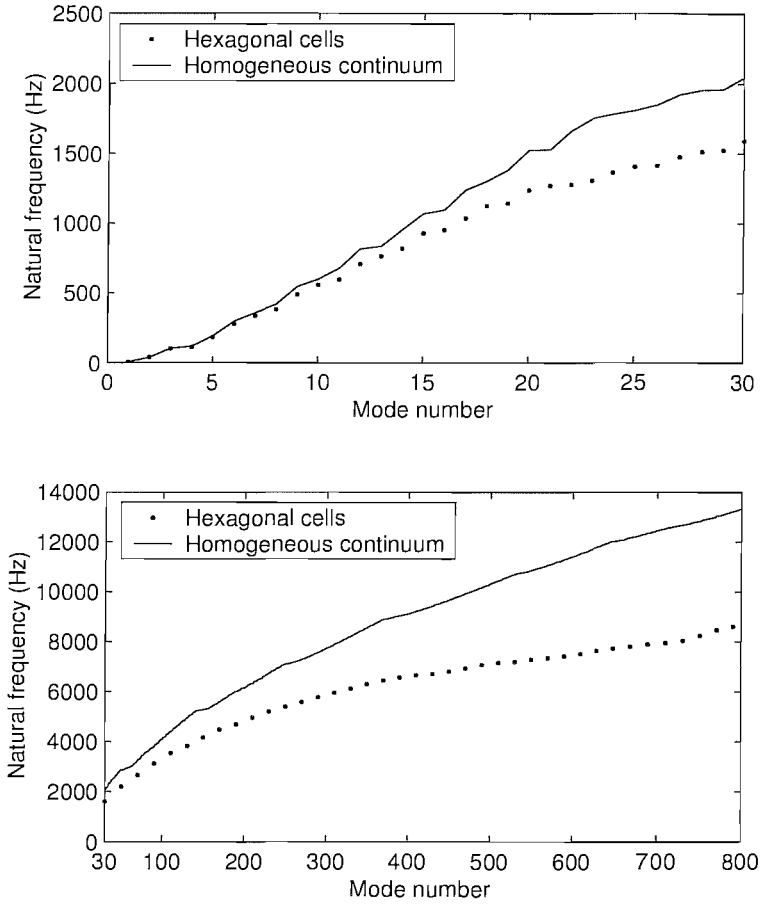

Figure 3.10: Comparisons of the natural frequencies of a beam made of hexagonal cells with those of continuum whose properties are chosen to match the fundamental frequency.

doubled indicating cell wall bending as the dominant mechanism of strain energy storage for all the modes. When shear correction is introduced, the frequencies are practically unaltered which means that shear in the cell walls is unimportant up to the modes under consideration.

§3.3.4 Modal distribution for beams made of irregular cells

To create a model of a beam having irregular cells, Voronoi cells were generated using randomly distributed 'seed' points. A rectangular portion was then cut from the block of these cells. The edges of each Voronoi cell represents a cell wall (see figure 3.12). The structure made of irregular cells is statistically isotropic as the Voronoi cells were generated without any directional preference.

Since the generation of these cells required randomly placed nucleation points for the Voronoi cells, there is a distribution of length of the cell walls– shown in figure 3.13. As

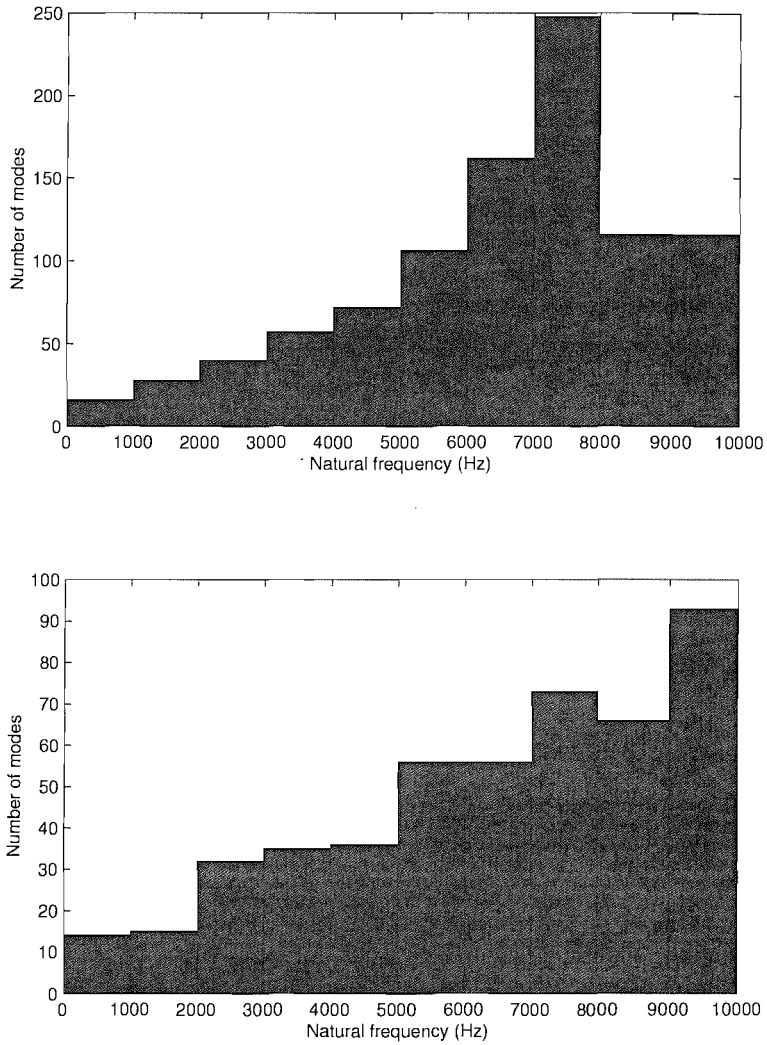

Figure 3.11: Modal density plot for beams made of hexagonal cells and continuum whose properties are matched to give the same fundamental frequency as the cellular beam. 961 modes are present in the case of the hexagonal cells in contrast with 476 modes for the continuum.

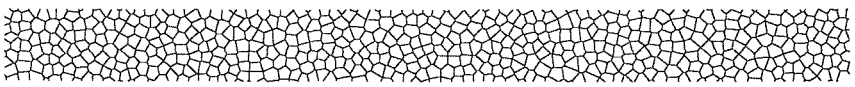

Figure 3.12: A cellular beam. The microstructure is composed of irregular cells.

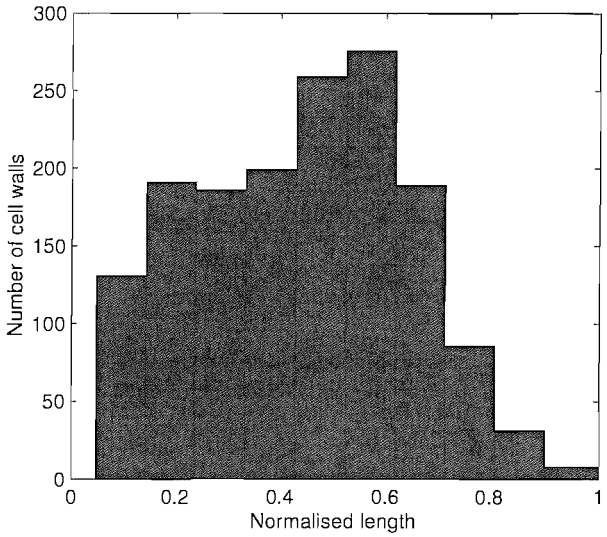

Figure 3.13: The distribution of length of the cell walls of the beam shown in figure 3.12.

a result, there is a small fraction of the total number of cell walls that is represented by short beams. This is undesirable from the point of view of mechanical modelling since the Euler-Bernoulli beam theory breaks down for very short beams. Since it is hard to control the length of the cell walls or the relative distance of the nucleation points with respect to close neighbours, an alternative approach of eliminating exceptionally short cell walls was taken. The nodes were moved such that that the two ends of a short beam (shorter than a prescribed threshold) coalesce to a point. The connectivity with other neighbours for each of the two merging nodes is left unchanged. The threshold of discarding short beams was kept as the thickness t to length l ratio equal to 1:3. Although this ratio may appear as one representing a very short beam, in practice, there are very few beams of this t/l ratio. A large majority of cell walls (about 90%) have a t/l ratio of 1:10 or less. A histogram of the distribution of the thickness to length ratio is plotted in figure 3.14. Note the strong skewness towards the left end of the histogram that represents thin long beams. The geometric data of the model are presented in table 3.4. The thickness is taken as the same for all the cell walls. The volume fraction of the solid is calculated using expression (2.20) as 0.044.

The dependence of natural frequencies on the mode number is shown in figure (3.15). The initial portion of the graph (the top figure in 3.15) shows a close match between the cellular beam frequencies and the homogeneous beam frequencies when the material parameters of the homogeneous beam are chosen to match the fundamental frequency.

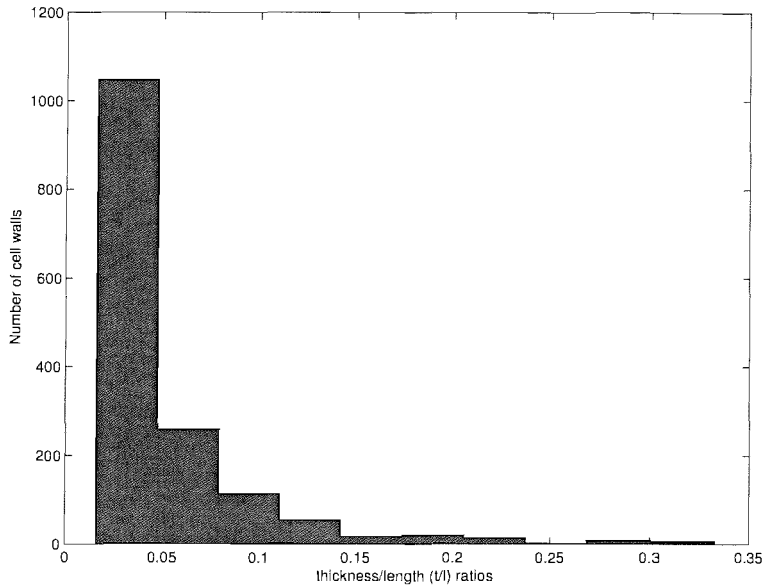

Figure 3.14: Histogram of thickness/length (t/l) ratio for the cell walls for the beam shown in figure 3.12. The distribution indicates that only about 10% cell walls have t/l ratio greater than 1/10 whereas 2.5% cell walls have t/l ratio greater than 1/5. Therefore, most of the cell walls (about 90%) have t/l ratio less than 1/10.

Length of the model L	600 mm
Overall depth in the transverse direction D	50 mm
Length of the cell wall material $\sum_i l_i$	7575.4 mm
Thickness of the each cell wall t	0.175 mm
Number of nodes	1148
Number of elements	1556

Table 3.4: Geometric data for the beam shown in figure 3.12.

A good match up to the seventh mode shows the validity of the effective medium theory in this band of frequency. The agreement is within 7% for up to the 13th mode. Beyond about the 20th mode, the cellular beam shows a relatively small modal spacing (and hence greater modal density). This is shown by a relatively flattening curve for the cellular beam in the top figure of (3.15). The bottom graphs in figure (3.15) show this trend changing– the curve for the cellular beam is steeper showing a greater modal separation and lower modal density. All this is a significant departure from the continuum behaviour. It can, therefore, be concluded that the effective medium behaviour is limited to the first few modes.

The modal spacing characteristics can be seen in the histogram showing the distribution of the number of modes in various intervals of natural frequency (figure 3.16).

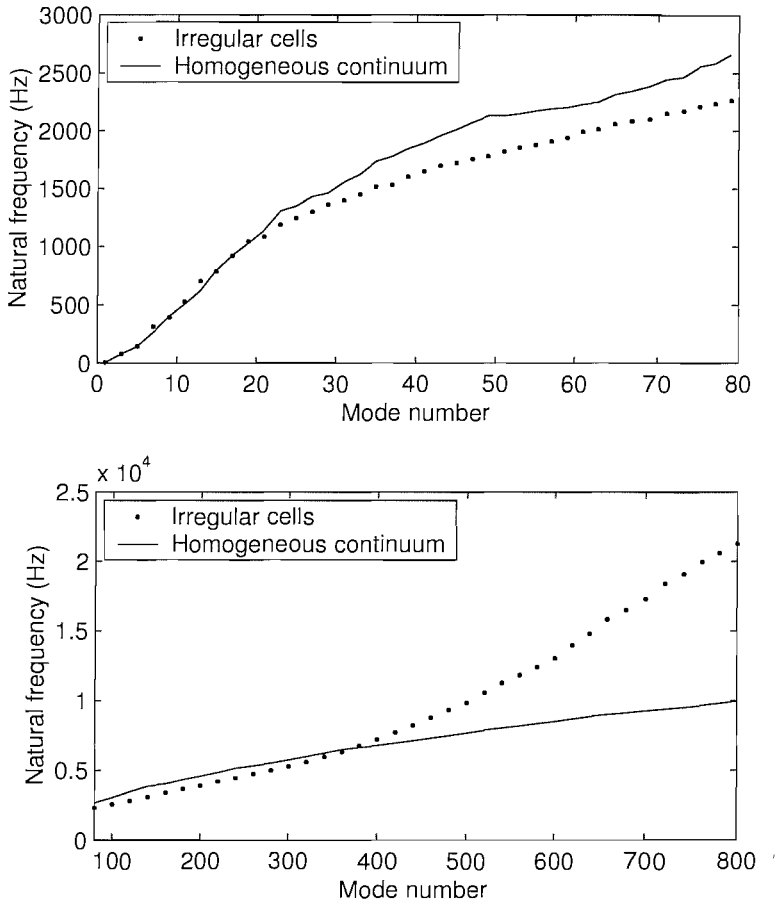

Figure 3.15: Comparison of the natural frequencies against the mode number for a beam made of irregular cells with those of a continuum whose properties are matched to give the same fundamental frequency.

The continuum beam shows a steadily increasing trend for modal density whereas the cellular beam shows an initially rising trend for modal density which falls gradually for high mode numbers.

When the thickness of the cell walls is doubled all the natural frequencies approximately double (not shown in any figure here). Therefore, the deformation of the cell walls is bending-dominated. This happens because most of the cells are polygons with the number of sides greater than three. Stretching-compression behaviour may become important if there is a significant number of the triangular cells present in the structure.

Structures made of irregular cells are different from the earlier ones in that the length of the cell walls is distributed (see figure 3.13). Therefore, the natural frequency of the individual cell walls also follows a certain distribution. This has important implications to the distribution of the cell wall resonance. In case of lattice structures, a large number of cell walls resonate at approximately the same frequency since each cell wall is identical.

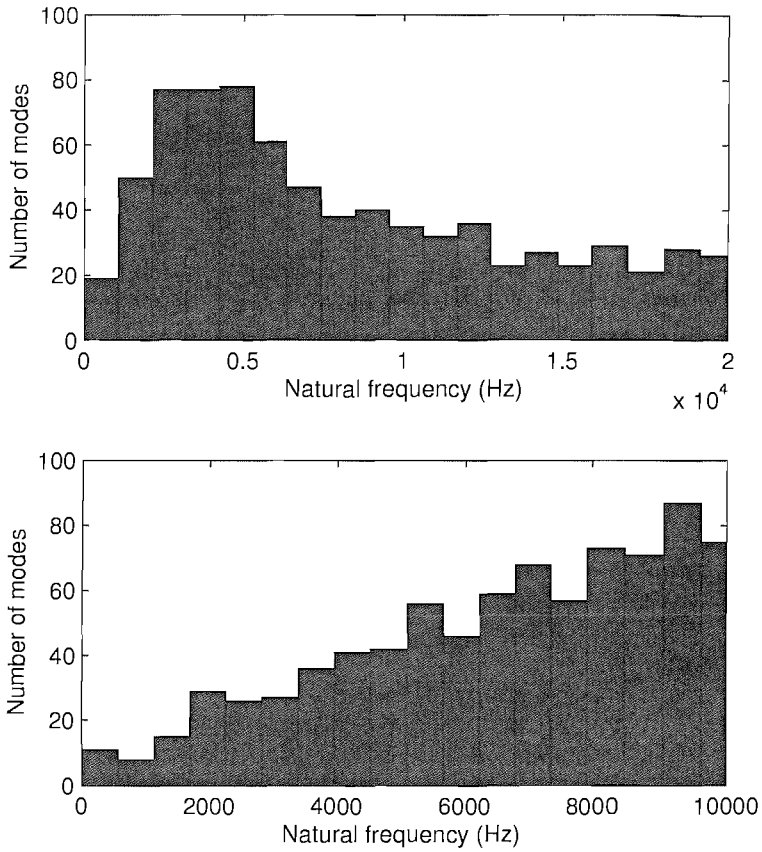

Figure 3.16: Modal density plot for the beam made of irregular cells (top figure) and the beam made of continuum whose fundamental frequency is matched with that of a beam having irregular cells (bottom figure). The first 800 modes are considered.

This leads to a sudden rise in the modal density around the cell wall resonance frequency. In the case of beams with irregular cells, this is gradual with mode number, hence a lack of a band of exceptionally high modal density (as in case of the triangular cells). The steeper curve at the high frequency end of for the natural frequency dependence on the mode number is in agreement with this general observation.

Comparisons of the frequencies of all the topologies are shown in figure 3.17. The fundamental frequency is the highest for the same area fraction in the case of the triangular cells. This is because triangular lattices deform due to cell wall extension for the low frequency regime. While the beams made of hexagonal cells show greatest modal density (least modal separation) at high mode number, the transition from low modal density to high modal density is gradual in case of hexagonal cells. As oppose to this the beams with triangular cells show a sudden increase in modal density since each cell wall is practically isolated from the rest once the cell walls start resonating. The square cells have an unusual dependence of the modal density on the mode number– this is attributed

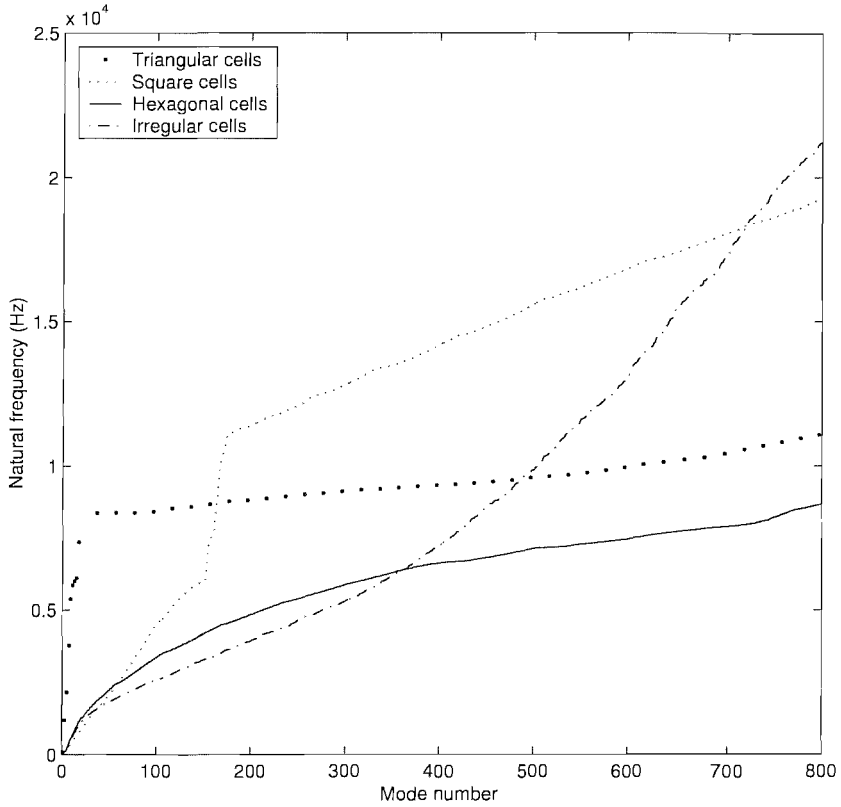

Figure 3.17: Comparisons of the frequencies against the mode numbers for four topologies: triangular, square, hexagonal and irregular cells are considered. The first 800 modes are shown.

to a large number of thickness-shear modes. Finally, the beams made of irregular cells show an increase in modal density followed by an increase in modal separation– this is partially due to (i) the distribution of the cell wall length, and (ii) the resonance of the cell walls at the edges at relatively low frequencies. There is one observation common to all the cellular topologies studied– the modal separation always decreases with respect to the properties matched continuum at the low frequency end of the spectrum.

§3.4 Conclusions

The modal spacing characteristics of cellular beams having various microstructures were compared with those of their continuum counterpart. Since this requires a large set of modes to be extracted, the one-dimensional theories, such as beam theory or rod theory, break down. Therefore, the use of plane stress finite elements was preferred for modal density calculations in this chapter.

Four cases of the microstructure were considered– beams made of triangular cells,

square cells, hexagonal cells and irregular cells were simulated. Each case exhibits its own modal spacing characteristics which is strongly dependent of the geometry of the microstructure.

Beams made of triangular cells show discrepancy with continuum behaviour as the mode number increases. Three regimes of mode number were identified– the first few modes are dominated by cell wall extension and the overall behaviour resembles that of an effective continuum when the properties are chosen to match the fundamental frequency. Beyond a certain critical frequency on the high frequency end of the spectrum the cell deformations are dominated by bending. This regime of mode numbers shows an unusually high modal density (low modal separation) as compared to the continuum counterpart. The reason for high modal density is the presence of a large number of identical cell walls– when they are interconnected, a large number of resonances are observed in a narrow frequency band. The mode number regime between the two extremes shows a transition.

The case of beam with square cells shows two main features in the modal density variation. Firstly the modal spacing is reduced as the continuum behaviour gradually breaks down. This is followed by a large number of thickness-shear modes. These modes are not observed for continuum at moderately high mode numbers. The reason for the existence of thickness-shear modes is the relatively low stiffness in shear when the cell walls are vertical and horizontal– the vertically oriented cell walls offer small resistance in bending. The main mechanism of strain energy storage is cell wall bending for all the modes up to moderately high mode number.

Beams made of hexagonal cells show a gradual decrease in modal separation. At high mode number, natural frequency is lowest compared to other microstructures studied for a fixed volume fraction of the material. The mechanism of strain energy storage is primarily cell wall bending for all the modes studied.

When the microstructure is irregular, the modal spacing decreases first, then increases (i.e. the slope of the natural frequency vs mode number shows this variation). This is partly due to the statistical distribution of the cell wall length as well as the presence of a significant number of cell walls at the boundary of the structure that are attached to the structure at one end and free at the other end.

Two features common to all the microstructure are (i) an initial agreement with continuum behaviour with an effective modulus of elasticity, and (ii) the gradual reduction in modal spacing as the continuum behaviour breaks down.

Chapter 4

Efficient free vibration calculations of cellular structures using continuum modes

§4.1 Introduction

While studying the macroscopic behaviour of cellular structures using the finite element method, the overall size of the domain should be much greater than the typical cell dimensions. Therefore, a realistic model of a cellular structure usually contains a large number of cells. Supposing that this description is available either by an analytical method or by digital image based techniques, the number of degrees-of-freedom of the overall structure will then be very large. Thus, the eigenvalue problem resulting from the free vibration analysis is large. Hence, the calculation of the eigenvalues and the eigenvectors is computationally expensive even if only the first few of them are required.

There have been attempts to reduce the order of the problem when the number of degrees-of-freedom in a structural problem is large. A commonly used approach is to take a small set of modes as the basis and apply Rayleigh's variational principle after expressing the kinetic energy and the potential energy in terms of the chosen set of basis modes. A practical difficulty here is a lack of a set of reasonable basis functions without performing any calculations associated with the original large scale eigenvalue problem. However, substantial computational gains can be made without compromising accuracy significantly, if there are physical (or any other) arguments that supply a set of guessed modes that are rich in the eigenvectors (eigenfunctions) of interest. In this thesis, the

so-called *continuum modes* afford such a basis.

There are alternative approaches to reduce the order of a model. For example, frequently a set of degrees-of-freedom (known as slave degrees-of-freedom) of a large finite element model are removed and a small group of degrees-of-freedom (known as master degrees-of-freedom) is retained [46, 76, 30, 110]. The eigenvalue problem of the reduced model is then solved for the approximate eigensolutions of the original eigenproblem. Two types of reduction methods exist, the static reduction and the dynamic reduction method. In the case of the static method, such as Guyan reduction [46], the inertia terms associated with the slave degrees-of-freedom are neglected because they are associated with the inverse of the dynamic stiffness matrix. In contrast, the dynamic methods include the effects of the inertia terms in a simple way. For instance, O'Callahan [76] suggested an improved reduced system (IRS) by adding a higher order term in the Taylor's series expansion of the inverse of the dynamic stiffness matrix. Friswell et al. [30] proposed an iterative IRS scheme to improve the accuracy. Recently, Xia et al. [110] developed a new iterative order reduction (IOR) technique by retaining all the inertia terms associated with the slave degrees-of-freedom.

The main aim of this chapter is to reduce the computational expense for free vibration calculations of cellular structures. Unlike the methods in the last paragraph, the proposed method incorporates all the structural details via complete mass and stiffness matrices but the resulting full scale eigensolution is avoided. The proposed method is suitable for calculations involved in low frequency dynamics. For high frequency dynamics, a piece of cellular solid ceases to behave as a continuum and the proposed method is not suitable in that case. It is reported here that a direct model order reduction by the use of a small set of basis modes possesses difficulties. It is then shown that this difficulty can be attributed to the presence of small components in the assumed modes that are associated with exceptionally high frequencies. A method to remove these high frequency components from the assumed modes is proposed. Two illustrative examples are presented to demonstrate the working of the method. For simplicity, the examples given in this chapter are two-dimensional.

§4.2 The proposed approximation for cellular structures based on continuum modes

It was shown in figure 2.1 that a structure made up of cellular material possesses geometrical features at two scales of length, l_s and l_c. We assume here that we are interested in the dynamics at a length scale much greater than l_c which means that the standing waves involved are longer than l_c. In these circumstances, we can guess the mode shape of the overall structure by filling the porosity and treating the structure as a homogeneous medium at the length scale l_s. Since the mode shapes do not strongly depend on the material properties, it does not matter what properties (in terms of the elastic modulus and density) are chosen while calculating the guessed mode shape. Once the mode shapes of this hypothetical medium are calculated, the mode shapes of the cellular structure are interpreted by mapping the displacement and rotation fields of this hypothetical porosity filled structure onto the nodes where cell walls join each other. The modes of this hypothetical medium will be referred to as the *continuum modes* in future. The calculation of the continuum modes does not require the knowledge of the effective properties and any reasonable value can be assumed. The reason why this approach is successful lies in the poor sensitivity of the normal modes to the material properties.

The last step of interpreting mode shapes of a cellular structure based on those of a continuum structure requires simple kinematic calculations. In engineering practice, the overall structures are often made of simpler elements such as plates, beams or shells. In that case, the calculation of the continuum modes will be greatly simplified. For example, if we have a planar cellular structure made up of beams at the length scales l_s, then we need to consider only the skeleton of beams to calculate the modes of a structure made of a hypothetical homogeneous medium. The displacement field at other points can be calculated by using the kinematic relations intrinsic to the beam theory i.e. plane sections remain plane and normal to the skeleton axis.

In our numerical implementations, we have restricted ourselves to planar structures with cell walls modelled as beams. The skeleton at length scales l_s is also modelled using beam elements. These beams have axial degrees of freedom in addition to the transverse displacement and rotation at each of the two nodes of an element as before. In a local co-ordinate system, the transverse displacement $\varphi(x)$ is approximated using the four Hermite cubics. The displacement and rotation fields within an element are then given

by

$$v_x^b(x,y) = -y\frac{\mathrm{d}\varphi}{\mathrm{d}x}, \quad v_y(x) = \varphi(x), \quad \theta(x) = \frac{\mathrm{d}\varphi}{\mathrm{d}x} \tag{4.1}$$

where $v_x^b(x,y)$ is the displacement in the axial direction of the element due to bending effects only, $v_y(x)$ is the transverse displacement of the neutral axis which is the transverse displacement of all the points normal to the neutral axis, and $\theta(x)$ is the rotation of the cross-section. The total displacement field is obtained by superposing the displacement in the axial direction due to tension-compression effects, i.e.

$$v_x(x,y) = v_x^b(x,y) + v_x^{tension}(x). \tag{4.2}$$

Note that $v_x^{tension}$ is assumed to be a function of x alone which asserts that this displacement component is distributed uniformly through the cross-section: an assumption consistent with one-dimensional rod theories. This component is calculated by interpolating the axial displacement field from the nodal axial displacements.

There will be a transverse displacement field $v_y^{tension}(x)$ due to the Poisson's ratio effect. However, this part of the displacement field has been ignored while obtaining the assumed modes for two reasons: firstly, the contribution to the overall displacement from tension-compression is usually small since rods are stiff in tension-compression than in bending. Secondly, there is no way to know the effective Poisson's ratio of the cellular material at the start of the calculations.

Having obtained the nodal displacements of the elements used to model the skeleton, equations (4.1) and (4.2) enable us to calculate the displacement and rotation fields at any point within the structure, as though the structure were made of homogeneous material. We use these kinematic relations now to map the displacement field $v_x(x), v_y(x), \theta(x)$ onto the displacements at the joints of the cell walls in the actual cellular structure, i.e.

$$\{v_x, v_y, \theta(x)\} \mapsto \boldsymbol{\psi}_{joints}. \tag{4.3}$$

The generalised displacement vector at the joints contains displacements in the plane and rotation. We will denote these components for the complete structure as obtained for the i-th mode of the structure by $\boldsymbol{\psi}_i$. We assume that the necessary co-ordinate transformations have been employed so that $\boldsymbol{\psi}_i$ is expressed in a global co-ordinate system.

Starting with p number of assumed modes $\boldsymbol{\psi}_i$, $i = 1, 2, ...p$ we are now in a position to build a reduced order model of size $p \times p$. To achieve this, we express the N-dimensional

vector of generalised co-ordinates ψ in terms of the assumed modes ψ_i as

$$\psi = \sum_{i=1}^{p} a_i \psi_i. \tag{4.4}$$

This expansion can be seen as the following transformation

$$\psi = \mathbf{T}\mathbf{a} \tag{4.5}$$

where the $N \times p$ transformation matrix $\mathbf{T}$ is the matrix whose columns are ψ_i, i.e.

$$\mathbf{T} = \left[\psi_1 | \psi_2 | ... | \psi_p\right]. \tag{4.6}$$

The vector $\mathbf{a}$ is of length p and contains $a_1, a_2, ..., a_p$ in a column.

The Rayleigh's quotient in terms of ψ as the trial vector is now given by

$$R = \frac{\psi^T \mathbf{K} \psi}{\psi^T \mathbf{M} \psi} \tag{4.7}$$

where $\mathbf{K}$ and $\mathbf{M}$ are the $N \times N$ stiffness and mass matrices respectively of whole structure. Note that these matrices contain all the detailed information about the geometry, properties and topology of the network of beams at the cell level.

Substituting the transformation (4.5) into (4.7) we have

$$R = \frac{\mathbf{a}^T \mathbf{T}^T \mathbf{K} \mathbf{T} \mathbf{a}}{\mathbf{a}^T \mathbf{T}^T \mathbf{M} \mathbf{T} \mathbf{a}}. \tag{4.8}$$

Thus Rayleigh's quotient is a ratio with $a_i, i = 1, 2, ..., p$ as the unknowns. Applying Rayleigh's variational principle, the first variation of this quotient must be zero, i.e. $\delta R(a_1, a_2, ..., a_p) = 0$. This amounts to setting the first derivative of R with respect to each of the unknowns to zero, i.e.

$$\frac{\partial R}{\partial a_i} = 0, i = 1, 2, ..., p. \tag{4.9}$$

Since both the numerator and the denominator of R are quadratic forms, application of condition (4.9) leads to the following eigenvalue problem

$$\overline{\mathbf{K}}\mathbf{a} = \mu \overline{\mathbf{M}}\mathbf{a} \tag{4.10}$$

where, $\overline{\mathbf{K}} = \mathbf{T}^T \mathbf{K} \mathbf{T}$ and $\overline{\mathbf{M}} = \mathbf{T}^T \mathbf{M} \mathbf{T}$. This eigenproblem is of size p. Assuming that $p \ll N$, we conclude that the reduced order model will save substantial computation since we do not need to solve the full scale eigenproblem (2.11) of size N.

Solution of the eigenvalue problem (4.10) gives p number of eigenvalues $\mu_r, r = 1, 2, ..., p$ and the corresponding eigenvectors $\mathbf{a}_1, \mathbf{a}_2, ..., \mathbf{a}_p$. The eigenvalues μ_r are approximations for the exact eigenvalues λ_r and the eigenvectors $\mathbf{a}_r$ contain information

about the corresponding mode shapes $\mathbf{u}_r$. Mode shapes of the overall structure are calculated for each $\mathbf{a}_r$ by substituting the components of these vectors into the summation (4.4). As can be seen that the reduced order eigenproblem (4.10) affords only p number of modal parameters instead of the complete set of N, but this is the price that one has to pay for computational economy. Often this will be satisfactory because in many practical situations, the excitation occurs over a band of frequency and hence one needs to consider modes only within (and slightly outside) this band.

When only one assumed mode is used in the summation (4.4), it amounts to substitution of the assumed mode for the trial vector ψ in equation (4.7). The accuracy of this approximation depends on the closeness of the assumed mode to the actual mode. It is a well known property of the Rayleigh's quotient that if the trial vector ψ differs from an eigenvector (say, $\mathbf{u}_r$) by an amount of the order of a small quantity, say ϵ, then the Rayleigh's quotient for this trial vector differs from the corresponding eigenvalue by an amount of the order of ϵ^2. Thus eigenvalue estimates are more accurate than the trial vectors used in the Rayleigh's quotient approximation. While using the continuum modes we find that the assumed modes are indeed very close to the actual modes (the difference, say, being of the order of ϵ), still the frequencies are poorly predicted by a direct application of Rayleigh's approximation. We will look into the approximation more closely in the next section. We will also propose a method to overcome the difficulty identified.

§4.3 Rayleigh's variational method and pre-conditioning of the trial modes

We turn to the single mode approximation first. It will be assumed that the trial mode is close to the actual mode shape. Expanding the trial vector ψ in terms of the eigenvectors of the original eigenproblem (2.11), we have

$$\psi = b_1\mathbf{u}_1 + ... + b_i\mathbf{u}_i + ... + b_N\mathbf{u}_N \tag{4.11}$$

where N is the size of the original eigenproblem and b_1, b_2,..., b_N are constants. For the ease of presentation of analysis, we assume that the trial mode resembles the first mode shape $\mathbf{u}_1$ and is corrupted by contribution from a single mode $\mathbf{u}_m$ so that

$$\psi = c_1\mathbf{u}_1 + c_m\mathbf{u}_m. \tag{4.12}$$

Further, assuming that the contribution from the m-th mode is small compared to that from the first mode (the mode whose frequency is being estimated by the approximation), we set $c_1 = 1$ and $c_m = \epsilon$ with $\epsilon \ll 1$. Substituting for ψ in the expression of R in (4.7) we have

$$R = \frac{(\mathbf{u}_1^T + \epsilon \mathbf{u}_m^T)\mathbf{K}(\mathbf{u}_1 + \epsilon \mathbf{u}_m)}{(\mathbf{u}_1 + \epsilon \mathbf{u}_m^T)\mathbf{M}(\mathbf{u}_1 + \epsilon \mathbf{u}_m)}. \tag{4.13}$$

We assume that the eigenvectors $\mathbf{u}_r$ are mass-normalised, so that the orthogonality relationship gives $\mathbf{u}_r^T \mathbf{M} \mathbf{u}_s = \delta_{rs}$ and $\mathbf{u}_r^T \mathbf{K} \mathbf{u}_s = \lambda_r \delta_{rs}$, $r, s = 1, m$, where δ_{rs} is the Kronecker-delta. Substituting the above in (4.13), after some algebra we obtain

$$R = \frac{\lambda_1 + \epsilon^2 \lambda_m}{1 + \epsilon^2}. \tag{4.14}$$

If $\lambda_1 = o(\lambda_m)$, then $R = \lambda_1 + o(\epsilon^2)$. However, if $\lambda_m \gg \lambda_1$, then the difference $R - \lambda_1$ can become very large affecting the approximation adversely. Suppose $\lambda_m / \lambda_1 = M \gg 1$, then $R \approx \lambda_1 (1 + \epsilon^2 M)$, and therefore, $R - \lambda_1 \approx \lambda_1 \epsilon^2 M \neq o(\epsilon^2)$.

The above analysis is restricted to a single mode approximation. The case of an approximation involving several continuum modes $\psi_1, \psi_2, \ldots$ can be treated similarly. Again for simplicity, we assume that there are only two modes to be used in the approximation (i.e. $p = 2$) and that each mode is corrupted by a small amount whose contribution comes from the m-th mode, $m \gg 2$. Expressing this mathematically, we have

$$\psi_1 = \mathbf{u}_1 + \epsilon \mathbf{u}_m, \quad \psi_2 = \mathbf{u}_2 + \epsilon \mathbf{u}_m. \tag{4.15}$$

Assuming $\mathbf{u}_1, \mathbf{u}_2, \mathbf{u}_m$ to be mass normalised, the transformation matrix $\mathbf{T}$ as in equation (4.6) takes the form

$$\mathbf{T} = [(\mathbf{u}_1 + \epsilon \mathbf{u}_m) | (\mathbf{u}_2 + \epsilon \mathbf{u}_m)]. \tag{4.16}$$

Substituting this into the expressions following equation (4.10), the 2×2 matrices are obtained as

$$\overline{\mathbf{K}} = \begin{bmatrix} (\lambda_1 + \epsilon^2 \lambda_m) & \epsilon^2 \lambda_m \\ \epsilon^2 \lambda_m & (\lambda_2 + \epsilon^2 \lambda_m) \end{bmatrix}, \quad \overline{\mathbf{M}} = \begin{bmatrix} (1 + \epsilon^2) & \epsilon^2 \\ \epsilon^2 & (1 + \epsilon^2) \end{bmatrix}. \tag{4.17}$$

The eigenvalues μ can be obtained in closed form from the following quadratic equation

$$A\mu^2 + B\mu + C = 0 \tag{4.18}$$

where $A = (1 + 2\epsilon^2)$, $B = -[(1 + \epsilon^2)(\lambda_1 + \lambda_2) + 2\lambda_m \epsilon^2]$ and $C = \lambda_1 \lambda_2 + \epsilon^2 \lambda_m (\lambda_1 + \lambda_2)$. Solving this quadratic we have

$$\mu_{1,2} = \frac{[(1 + \epsilon^2)(\lambda_1 + \lambda_2) + 2\epsilon^2 \lambda_m] \pm \sqrt{(1 + \epsilon^2)^2 (\lambda_1 - \lambda_2)^2 + 4\epsilon^4 [\lambda_m^2 - \lambda_m (\lambda_1 + \lambda_2) + \lambda_1 \lambda_2]}}{2(1 + \epsilon^2)}. \tag{4.19}$$

When ϵ is small but λ_m is large, i.e. when $\epsilon \to 0$ and $\lambda_m \gg \lambda_2 > \lambda_1$ then

$$\mu_{1,2} = \left(\frac{\lambda_1 + \lambda_2}{2}\right), \quad \left(\frac{\lambda_1 + \lambda_2}{2} + \epsilon^2 \lambda_m\right). \tag{4.20}$$

This confirms that the two approximate eigenvalues μ_1 and μ_2 do not resemble the actual eigenvalues λ_1 and λ_2 in the circumstances. When we implemented the method outlined in section 4.2, we observed that the errors in the estimation of approximate eigenvalues μ were often very large. To understand this further we present the following sensitivity analysis to study the rate of change of the approximate eigenvalues with respect to change in the parameter ϵ. To do this, we view the eigenproblem (4.10) as one that depends on the parameter ϵ. In that case, the eigenvalues have the functional relationship $\mu_i = \mu_i(\epsilon)$. Fortunately, we can estimate the derivative of an eigenvalue exactly when an eigenproblem depends on a parameter [29]. The expression for the eigenderivative is given in the present context by

$$\frac{\partial \mu_i}{\partial \epsilon} = \frac{\mathbf{a}_i^T \left[\partial \overline{\mathbf{K}}/\partial \epsilon - \mu_i \partial \overline{\mathbf{M}}/\partial \epsilon\right] \mathbf{a}_i}{\mathbf{a}_i^T \overline{\mathbf{M}} \mathbf{a}_i}. \tag{4.21}$$

Since we know the functional dependences $\overline{\mathbf{K}}(\epsilon)$ and $\overline{\mathbf{M}}(\epsilon)$ explicitly via equation (4.17), differentiation leads to

$$\frac{\partial \overline{\mathbf{K}}}{\partial \epsilon} = 2\epsilon\lambda_m \mathbf{1}, \quad \frac{\partial \overline{\mathbf{M}}}{\partial \epsilon} = 2\epsilon \mathbf{1} \tag{4.22}$$

where the 2×2 matrix $\mathbf{1}$ contains 1's everywhere. We now divide the above sensitivity relationship by (μ_i/ϵ) and define the non-dimensional ratio σ_i as the *relative sensitivity* for the i-th mode to obtain

$$\sigma_i = \frac{(\partial \mu_i/\partial \epsilon)}{(\mu_i/\epsilon)} = \frac{2\epsilon^2 \left(\frac{\lambda_m}{\mu_i} - 1\right) g}{(1 + \epsilon^2)} \tag{4.23}$$

where

$$g = \frac{\mathbf{a}_i^T \mathbf{1} \mathbf{a}_i}{\mathbf{a}_i^T \mathbf{a}_i}.$$

Note that the number g is bounded in the range $0 < g < 2$ since g is a Rayleigh's quotient associated with the matrix $\mathbf{1}$ and since the eigenvalues of $\mathbf{1}$ are 0 and 2. As $\epsilon \to 0$, both $\overline{\mathbf{M}}$ and $\overline{\mathbf{K}}$ become diagonal so that $\mathbf{a}_i$ is either $[0 \quad 1]^T$ or $[1 \quad 0]^T$. For these vectors, $g = 1$. Hence for $\epsilon \ll 1$

$$\sigma_i \approx \frac{2\epsilon^2 \left(\frac{\lambda_m}{\mu_i} - 1\right)}{(1 + \epsilon^2)}. \tag{4.24}$$

As in the previous cases of equation (4.14) and (4.19), the smallness of ϵ^2 alone does not guarantee accuracy of the approximation: we require smallness of the term $\epsilon^2 \lambda_m$.

Since the approximation method we have proposed uses the physical reasoning that the overall mode shapes must resemble those of a continuum, it is very difficult to control the contributions (however small) from higher modes. The case of cellular structures is a particularly difficult one because it requires building a very large model meaning that the eigenvalues of the complete structure span a large range, i.e. $\lambda_1 \ll \lambda_N$. This increases the chances of contributions coming from the high frequency end of the spectrum.

Having identified the difficulty, we now propose a way to help the situation by filtering the components corresponding to high frequencies from the assumed modes $\boldsymbol{\psi}$ before they are used either in the Rayleigh's quotient (as in one mode approximation) or before they are used in the variational formulation of equations (4.4) through to (4.10). We propose to remove the high frequency eigenmodes from the trial vectors by the use of inverse power iterations. When the power method of determining the dominant eigenvalue of a matrix is used, the method works by progressively enriching the iterated vector in favour of the large eigenvalue side of the spectrum. The contribution from the small eigenvalue side gradually becomes smaller as the iterations proceed. Since our aim is to determine the lowest few natural frequencies and the corresponding modes, we need to iterate with the inverse matrix. Fortunately, we do not need to compute the inverse explicitly. All we need to do now is to cast the original eigenproblem (2.11) in the following form

$$\frac{1}{\lambda}\mathbf{K}\boldsymbol{\psi} = \mathbf{M}\boldsymbol{\psi}. \tag{4.25}$$

The iterations at the r-th step become

$$\mathbf{K}\boldsymbol{\psi}_i^{(r)} = \mathbf{M}\boldsymbol{\psi}_i^{(r-1)} \tag{4.26}$$

where the superscript refers to the iteration number. The above set of algebraic equations needs to be solved for $\boldsymbol{\psi}_i^r$. The first vector $\boldsymbol{\psi}_i^{(0)}$ is the continuum mode presented in section 4.2. In our numerical implementations, we found just one iteration to be sufficient. In spite of extra calculations involved in solving (4.26) and those involved in mapping (4.3), an overall saving in the total number of floating point operations was observed in our implementations.

§4.4 Numerical examples and discussions

We now present two numerical implementations of the scheme of using continuum modes for calculations of natural frequencies and normal modes for the first few modes. In the first instance we undertake a cantilever beam made of cellular material. Then we present

calculations for two cellular beams joined at right angle: we will refer to this structure as the L-beam (figure 4.5).

§4.4.1 Example 1: the cantilever beam

Consider the cantilever beam shown in figure 3.12. The geometric data for the beam were presented in table 3.4. The cell walls are modelled using two node Euler-Bernoulli beam elements for the finite element calculations. We are interested in the low frequency dynamics which justifies the use of thin beam theory.

The continuum modes are obtained from the finite element analysis of a single fixed-free beam having the same macroscopic dimensions as the cellular beam. A small size finite element model having twelve elements with cubic interpolation is used to calculate the continuum modes. Mapping on the lines of equation (4.3) is achieved using equations (4.1) and (4.2). The first ten continuum modes are chosen as the basis modes after pre-conditioning using equation (4.26). An in-house code was developed in MATLAB [72] for predicting the natural frequencies and the mode shapes using both the approximate method and the full scale model.

Table 4.1 shows the first ten natural frequencies as calculated by solving the full scale eigenproblem (2.11) and by using the approximation of pre-conditioned continuum modes presented in this chapter. The accuracy of the calculation is quite remarkable. The first nine modes show an error less than 1%.

Mode no.	Natural frequency (Hz)	Approximate frequency (Hz)	Relative error(%)
1	4.79	4.79	-4.89×10^{-7}
2	29.40	29.40	-5.51×10^{-6}
3	80.50	80.50	-4.21×10^{-4}
4	102.51	102.51	-4.78×10^{-4}
5	143.82	143.83	-3.96×10^{-3}
6	213.35	213.41	-2.69×10^{-2}
7	317.00	317.68	-2.14×10^{-1}
8	324.64	324.82	-5.77×10^{-2}
9	393.06	394.01	-2.41×10^{-1}
10	493.45	526.98	-6.80

Table 4.1: Comparison between the natural frequencies as calculated from the full model (equation 2.11) and the approximation based on pre-conditioned continuum modes for the cellular beam in figure 3.12.

Comparing mode shapes quantitatively is not as straightforward as comparing natural frequencies because of non-uniqueness of eigenmodes up to an arbitrary scaling.

MAC (Modal Assurance Criterion) is frequently used to correlate the experimental mode shapes with those obtained by the finite element method [28]. In this chapter, we use this established method to correlate the mode shapes obtained from the proposed approximation with finite element simulated modes.

The MAC matrix $\mathbf{W}$ has the entries given by [28]

$$W_{rs} = \frac{(|\mathbf{u}_r^T \boldsymbol{\psi}_s|)^2}{(\|\mathbf{u}_r\|)^2(\|\boldsymbol{\psi}_s\|)^2}. \tag{4.27}$$

The diagonal terms of the matrix represent the correlation between two eigenvectors associated with the same mode, whereas the off-diagonal terms reflect the correlation between the cross eigenvectors. For best correlation, the value of W_{rs} will be 1, whereas the value of W_{rs} will be zero for no correlation. A grey scale with black colour for $W_{rs} = 1$ and white colour for $W_{rs} = 0$ is used. The intermediate shades indicate the correlation proportionately.

The relative magnitudes of the quantity W_{rs} in figure 4.1 reflect the correlation between the *original* assumed continuum modes without pre-conditioning with the finite element modes. Similarly, figure 4.2 is plotted with W_{rs} calculated on the basis of the proposed reduced order model after pre-conditioning and the finite element modes. Note the improvement in the correlation due to the pre-conditioning and the application of Rayleigh's variational principle.

As a second method to compare the two eigenvectors [28], an eigenvector obtained from the reduced order model is plotted against the corresponding eigenvectors from the full scale model in figure 4.3. If the points fall around the straight line passing through the origin at an orientation of 45^o, a good correlation is indicated. The pair of two eigenvectors associated with the first, eighth, ninth and the tenth mode are plotted in figure 4.3.

The plot shows an excellent correlation for the first mode pair. The correlation up to the eighth mode is found to be very good. The ninth mode does not correlate so well. In the case of the tenth mode, the approximate mode is poorly correlated with the eigenvector of the full-scale model. The natural frequency predicted based on the approximate mode is about 7% higher than the corresponding finite element value. Considering that only ten modes are used in the calculation, and the correlation of the tenth assumed mode is poor with the corresponding actual mode, the accuracy is surprisingly good. More number of modes must be included in the basis for improving the last mode.

The flop counts for the full scale problem are compared with those of the reduced

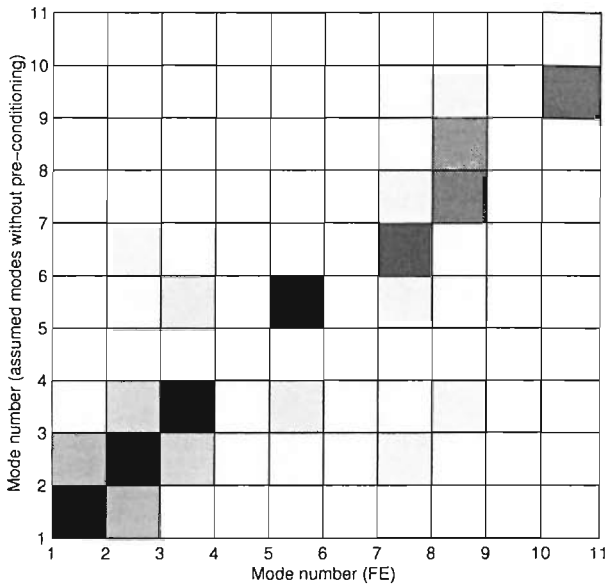

Figure 4.1: MAC plot correlating the continuum assumed modes and the finite element modes. The dark blocks on the diagonal indicate good correlation for the first few modes; yet the predicted frequencies based on these assumed modes are very inaccurate.

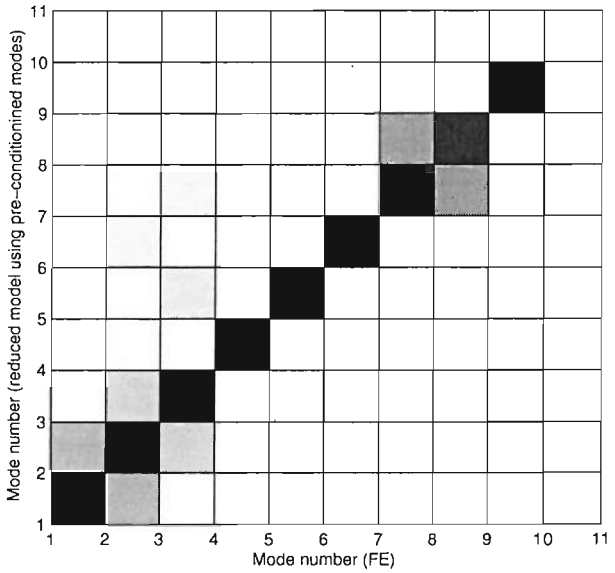

Figure 4.2: MAC plot representing correlation between the two sets of eigenvectors as calculated by the finite element and the reduced order model. The dark blocks on the diagonal show excellent correlation up to the eighth mode. The correlation for the ninth mode is not so good, whereas the tenth mode shows poor correlation.

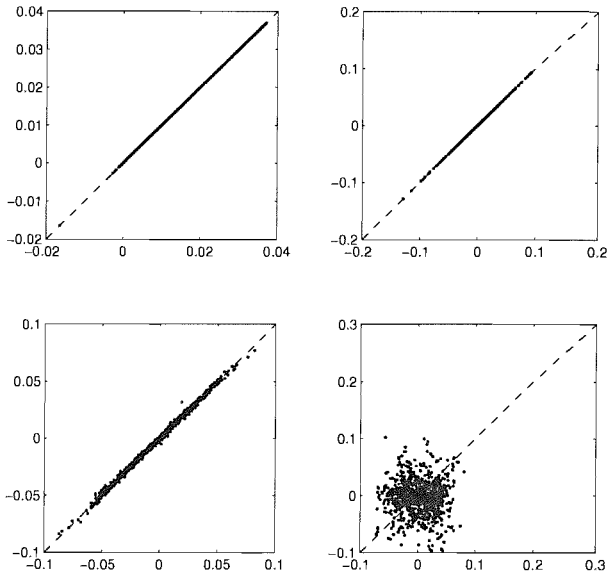

Figure 4.3: The straight line correlation plot for the first (top left), eighth (top right), ninth (bottom left) and the tenth (bottom right) mode respectively. Note the degradation in the correlation with the mode number.

order problem in table 4.2. The full scale model is of size 3444 × 3444, whereas the continuum mode based reduced order model is of size 10 × 10. In view of this, only ten modes were extracted while solving the full-scale problem (2.11) using a sparse solver in MATLAB.

Two other models were generated by replacing the microstructure of the present example by different cellular topologies. The degrees-of-freedom of the models were 1431 and 4962 respectively. The basis continuum modes used in example 1 were used for these models as the external dimensions of the beam were the same. Therefore, the continuum modes need to be generated only once for structures with the same overall dimensions but filled with various cellular topologies. This is another advantage of the method leading to further computational savings in such cases. However, flops required for the generation of the continuum modes were included in the comparison for all the reduced order models.

Table 4.2 shows that the total flops required for the approximate method in the case of example 1 is only 9.58% of that for the whole model. Break-up of flops indicates that the generation of full $\mathbf{K}$ and $\mathbf{M}$ is much cheaper, it requires flops less than 1% when compared to the full model calculations. Table 4.2 also indicates that the savings will be a lot more for structures with higher degrees-of-freedom. Sometimes, a single mode calculation is very economical when we use the assumed mode directly into the

Rayleigh's quotient. We implemented this for the first mode and the approximation matched the value obtained from the full scale calculation within 0.000001%.

Degrees of freedom		Floating point operations: Generation of of **K** & **M**	Floating point operations: Calculations of frequencies & modes	Floating point operations: Total calculations	% of full scale calculations
1431	reduced model	1.20×10^5	6.74×10^6	6.86×10^6	11.39%
1431	full model	1.20×10^5	6.01×10^7	6.03×10^7	100%
3444 Example 1 (Section 4.4.1)	reduced model	3.14×10^5	2.08×10^7	2.11×10^7	9.58%
3444	full model	3.14×10^5	2.20×10^8	2.20×10^8	100%
4962	reduced model	4.54×10^5	3.37×10^7	3.42×10^6	7.49%
4962	full model	4.54×10^5	4.56×10^8	4.57×10^8	100%

Table 4.2: Comparison of the floating point operations for the full-scale problem (equation 2.11) and the approximation using the pre-conditioned continuum modes for both the models. Note that calculations of eigenvalues and eigenvectors for the reduced model include all the stages starting from the generation of the pre-conditioned assumed modes up to the prediction of the approximate frequencies and modes.

The first five modes of vibration of the beam are presented in figure 4.4. The eigenvectors are calculated using the approximate method. The first three modes resemble those of a solid fixed-free beam. These three modes are primarily bending modes. The fourth mode resembles the first axial mode in tension-compression for a fixed-free elastic rod with axial degrees-of-freedom. The fifth mode is the fourth mode in the bending series. The approximate method has predicted both the bending and the axial modes accurately. The figures broadly justify the idea of using the continuum modes as the assumed modes for the cellular structures.

§4.4.2 Example 2: the L-beam

The second example of an L-beam is shown in figure 4.5. To generate the structure of this shape filled with cellular material, a large block of Voronoi cells was created. Then a structure of the required L-shape was cut out of this rectangular block. Cell walls having very small length were created during the model generation process. They were eliminated in a similar way as was done for the cantilever beam. About 3% of the cell walls needed deleting from the mesh. The thickness of the cell walls was chosen such that the minimum t/l ratio is 1/3. The distribution of lengths thus generated indicates that only 7.4% elements have t/l ratios greater than 1/10 with 2.3% elements have t/l

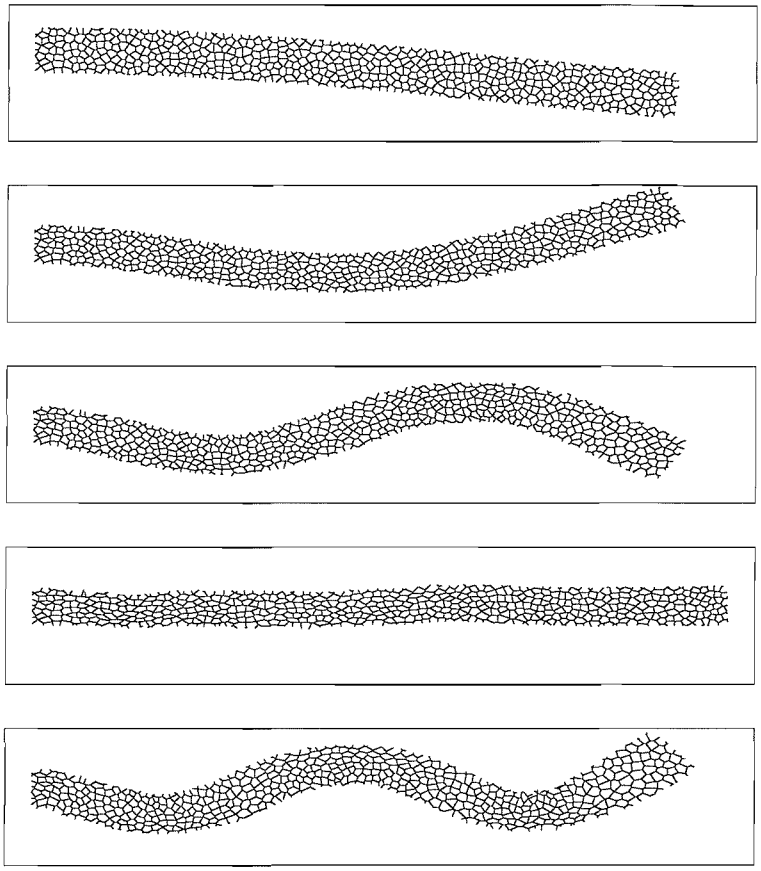

Figure 4.4: The first five mode shapes of the cantilever beam shown in figure 3.12. The deflected shape of the first mode resembles the first flexural mode of a solid fixed-free beam. The second, the third and the fifth modes resemble the second, third and the fourth flexural modes of a cantilever respectively. In contrast, the fourth mode is primarily an axial mode.

ratio greater than 1/5. Therefore, about 92.6% of the cell walls have a t/l ratio less than 1/10. Hence, the shear effect can be neglected for most cell walls. The geometric data for the L-beam are presented in table 4.3. The two arms of this L-beam have a L/D ratio about 8.5. The area fraction of the cellular solid calculated using equation (2.20) is about 0.025. The continuum modes were calculated from a finite element analysis of the L-shaped skeleton.

Table 4.4 shows a comparison of the natural frequencies as determined from equation (2.11) with those calculated on the basis of the pre-conditioned continuum modes. The agreement is excellent again, with frequencies well within 1% up to the eighth mode. To assess the accuracy of the modes obtained via the reduced order model, MAC matrix $\mathbf{W}$ is calculated to correlate the reduced order modes and the finite element modes. The MAC plot for the L-beam is shown in figure 4.6. The figure indicates excellent

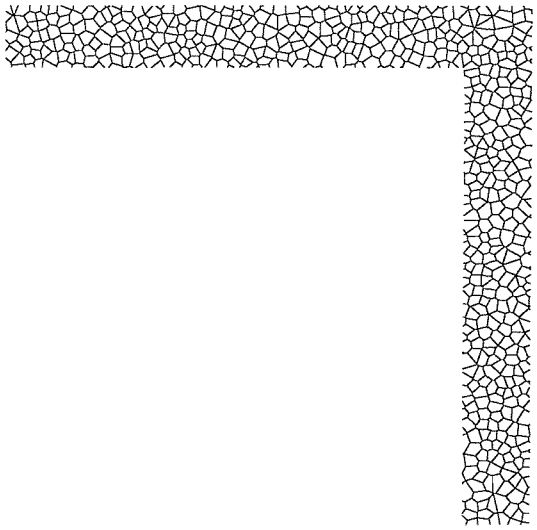

Figure 4.5: An L-beam composed of irregular cells. Note that the left-most and the bottom-most boundary are fixed.

External length of each arm of the model	1250 mm
Internal length of each arm of the model	1100 mm
Overall depth perpendicular to the length direction D	150 mm
Length of the cell wall material $\sum_i l_i$	27171.2 mm
Thickness of the cell walls t	0.33 mm
Number of nodes	1279
Number of elements	1696

Table 4.3: Geometric data for the L-beam shown in figure 4.5.

correlation up to the eighth mode. The ninth and the tenth mode show poor correlation as expected.

The size of the eigenvalue problem is reduced to 10×10 from 3837×3837 for this example. The total floating point operations involved in the approximate method (3.74×10^7) is less than 10% of the operations required for the full model (3.93×10^8). Therefore, substantial computational saving is achieved for such complex structure. Similar to the previous example, only ten modes of the full model were calculated using sparse solver.

The L-beam with identical arms will have degenerate modes of multiplicity two if the beams have only bending degrees-of-freedom. This is because the corner will act as a pin joint with only rotations allowed and the system will have two coincident natural frequencies. Each of these corresponds to a beam fixed at one end and pinned at the other. When axial degrees-of-freedom are allowed and when two arms are not identical

Mode no.	Natural frequency (Hz)	Approximate frequency (Hz)	Relative error(%)
1	4.25	4.25	-1.86×10^{-4}
2	6.54	6.54	-9.26×10^{-4}
3	11.87	11.88	-1.01×10^{-2}
4	12.85	12.85	-8.54×10^{-3}
5	14.75	14.76	-8.52×10^{-3}
6	18.24	18.25	-2.84×10^{-2}
7	25.41	25.44	-1.27×10^{-1}
8	30.14	30.22	-2.51×10^{-1}
9	39.55	41.18	-4.13
10	39.96	42.22	-5.66

Table 4.4: Comparison of the natural frequencies as calculated from the full model (equation 2.11) and the approximation using the pre-conditioned continuum modes for the L-beam shown in figure 4.5.

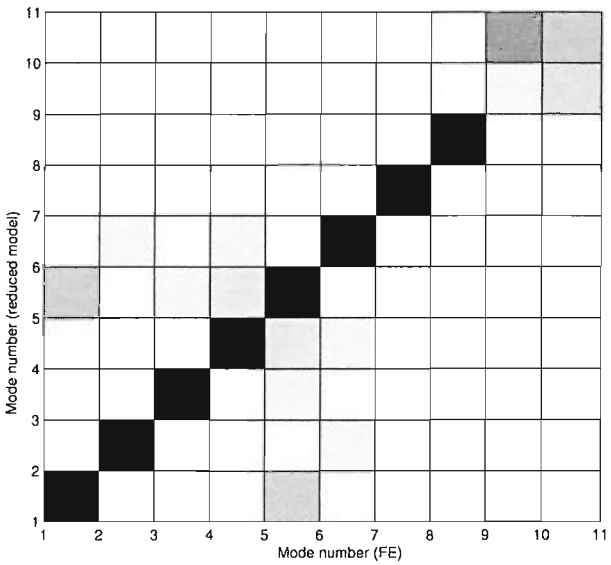

Figure 4.6: MAC plot representing correlation between the modes calculated by the finite element and the approximate method of the L-beam structure. The dark blocks on the diagonal show excellent correlation up to the eighth mode. The ninth and the tenth modes show poor correlation.

(as in case of cellular arms) the degeneracy is broken and we expect to obtain frequencies in doublets. Each pair originates from one set of degenerate modes.

When we look at the frequencies of the cellular L-beam (see table 4.4), we find a similar pattern but the frequencies are not that close. For example, the ratio of the first and the second frequencies is 1.54. The third and the fourth are the closest having a ratio equal to 1.08, whereas the fifth and the sixth possess a ratio of 1.24. The originally degenerate modes have split quite far because the two arms of the L-beam

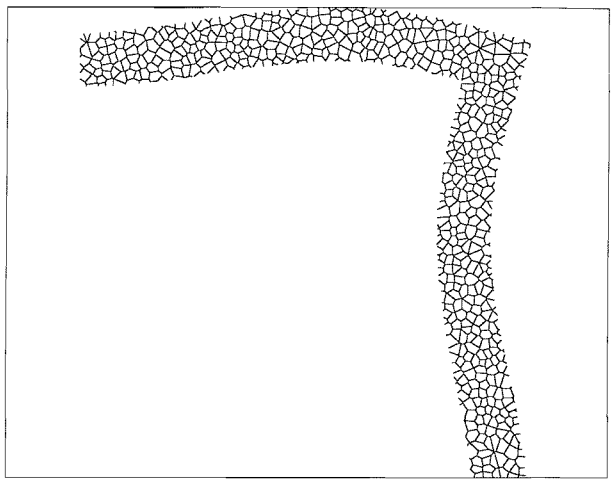

Figure 4.7: The first mode of free vibration of the L-beam.

possess different microstructure. As a result, their individual natural frequencies are not the same.

Figures (4.7) to (4.11) show the first five natural modes of the L-beam. The mode shapes as obtained from the full scale finite element analysis using equation (2.11) and those obtained from the reduced order model almost coincide. Therefore, the mode shapes are displayed based on the eigenvectors calculated for the full model. The overall mode shapes of the cellular L-beam are similar to the corresponding modes of a solid L-beam.

The first two modes are overall bending modes (see figures 4.7 and 4.8). The third and the fourth mode resemble each other (see figures 4.9 and 4.10). The horizontal arm is in the stretching-compression mode of vibration and the vertical arm is in flexural vibration in the case of the third mode. The opposite happens for the fourth mode where the stretching-compression mode of vibration is observed in the vertical arm and the flexural mode in the other. The fifth mode (see figure 4.11) is primarily a bending mode with each arm corresponding to the second mode of vibration for a fixed-pinned beam.

Cellular metals are often used as the core for sandwich constructions. To model such composites, one could take two alternative routes. While the core can be modelled in a manner similar to that used for illustrations in this chapter, the external plates could be modelled using additional elements (beams for planar models of foams; and plates for three dimensional geometry). If the external plates are not isotropic (as often is the case), the relevant anisotropy (usually orthotropy) can be accounted for by appropriately

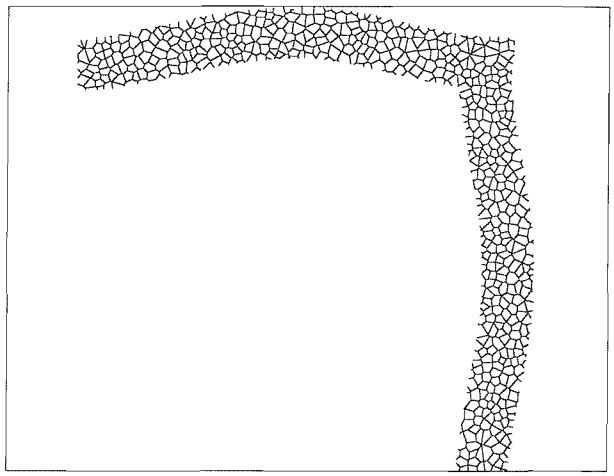

Figure 4.8: The second mode of vibration. This mode is also a flexural mode, similar to the first mode, but the phase of vibration in the two limbs of the structure is opposite of the mode presented in figure 4.7.

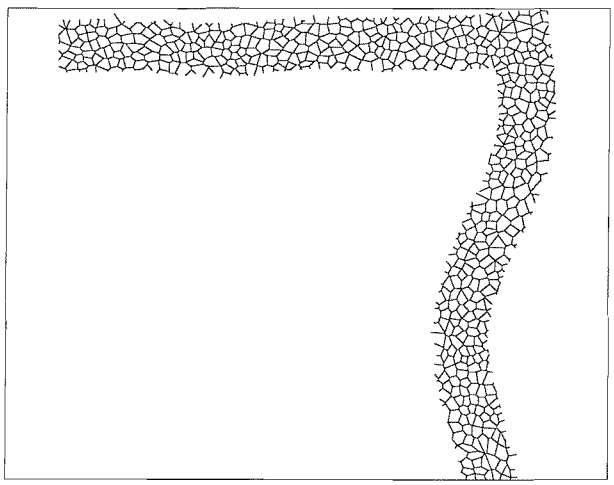

Figure 4.9: The third mode of vibration. The horizontal arm is in stretching-compression mode of vibration whereas the vertical arm is in flexural vibration.

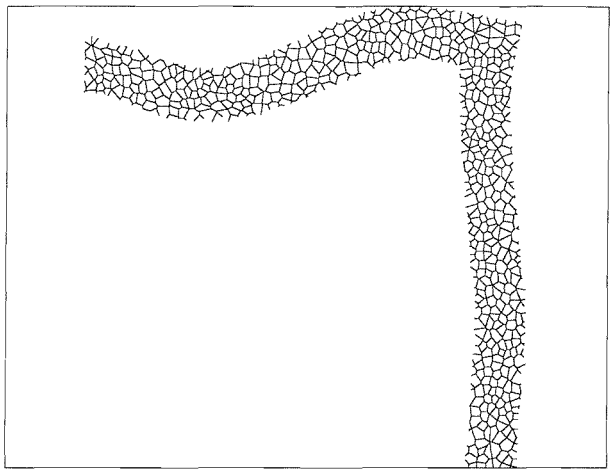

Figure 4.10: The fourth mode of vibration. This mode is similar to the third mode, the difference being that the vertical arm is in stretching-compression mode of vibration in this mode. The horizontal arm is in flexural mode of vibration.

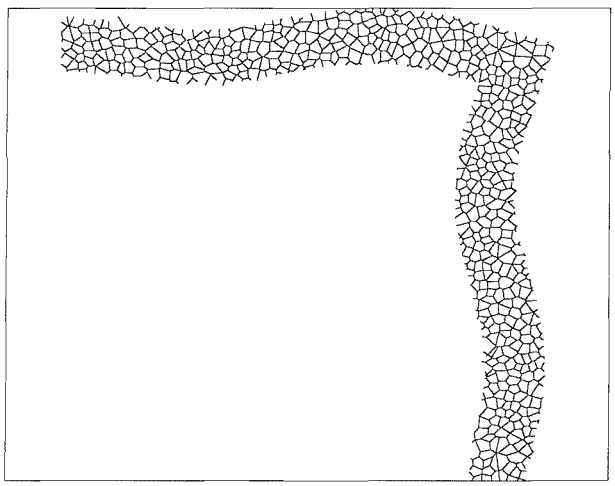

Figure 4.11: The fifth mode of vibration. It is primarily a bending mode with each arm corresponding to the second mode of vibration for a fixed-pinned beam.

choosing the elements that represent the face-plates. An alternative to this approach could be to use analytical models that combine the face-plate geometry and properties with those of the core– the core being represented by an effective medium. In this case, the shear modulus of the core will be of great importance. We have not undertaken the task of modelling such composites since the main objective of this chapter is to present an approximation method and not to model cellular composites.

§4.5 Conclusions

A realistic representation of cellular structures requires modelling structures with a number of cells. As a result, the eigenvalue problem associated with the free-vibration is large, and hence, computationally demanding. An approximate method was presented in this chapter to overcome this difficulty. The proposed method can be used for approximately calculating the first few natural frequencies and the associated modes for the cellular structures with substantial computational saving. The method is based on the assumption that macroscopically cellular structures behave as a homogeneous continuum for low frequency dynamics. Assumed modes based on the continuum modes were used as basis in this method. The frequencies and the mode shapes were predicted accurately using Rayleigh's variational principle.

A direct use of the assumed modes for the approximation leads to large errors. It was shown to be due to the presence of small high frequency components in the assumed modes. A method based on inverse power iterations was used to pre-condition the assumed modes successfully. Further, a sensitivity analysis was performed to study the effect of an arbitrarily chosen vector on Rayleigh's approximation. We found that even small errors in the trial vector can ruin the predictions unless care is taken in pre-conditioning the assumed continuum modes.

Two examples were given for planar structures to demonstrate the working of the method. Structures made of irregular cells were analysed. A significant model-order reduction was achieved by the proposed method without compromising the accuracy. The method may be applicable for more complex structures.

Chapter 5

Frequency response calculations of cellular structures using continuum modes

§5.1 Introduction

In the previous chapter, the natural frequencies were accurately predicted using the continuum modes as the basis functions. An accurate prediction of the natural frequencies alone does not guarantee an accurate prediction of the frequency response. This is because the frequency response functions combine the natural frequency and the mode shape information. An indication of the prediction of mode shapes came in the last chapter from the MAC plots between the mode shapes of the complete model and those of the reduced order model. In this background, we explore the applicability of the model order reduction by the use of continuum modes for frequency response calculations. To bring realism into the calculations, damping is included in the model.

Equations of motion for the reduced order model will be derived in the next section when the forcing is harmonic. The application of Lagrange's equations will lead to a reduced order system with smaller size stiffness, inertia and damping matrices in addition to the reduced order forcing vector. This will lead to an approximate frequency response function matrix. Since only a few continuum modes are used as the basis for model order reduction, we expect good predictions only in the low frequency band of the response.

The problem of small contributions from exceptionally high frequency modes into the assumed modes is again found to pose difficulty. Therefore, the set of basis modes

were pre-conditioned using inverse power iterations in the same way as were done in the previous chapter.

§5.2 Development of the reduced order model using the continuum modes

The full scale model of cellular structures was constructed in a manner similar to the previous sections. Therefore, it is assumed that the stiffness matrix $\mathbf{K}$, the mass matrix $\mathbf{M}$, and the force vector $\mathbf{f}$ are given. Further, it is assumed that viscous damping matrix $\mathbf{C}$ of the whole model is available to us. We will start with the Lagrange's equation of motion for the full model, $\mathbf{M}\ddot{\mathbf{q}} + \mathbf{C}\dot{\mathbf{q}} + \mathbf{K}\mathbf{q} = \mathbf{f}$, equation (2.9).

If $\mathbf{f}$ is harmonic force in the form $\mathbf{f} = \hat{\mathbf{f}}e^{j\omega t}$, then the response $\mathbf{q}$ can be expressed as $\mathbf{q} = \hat{\mathbf{q}}e^{j\omega t}$. Substituting $\mathbf{f}$ and $\mathbf{q}$ in equation (2.9) and simplifying, we obtain

$$\hat{\mathbf{q}} = (-\omega^2\mathbf{M} + j\omega\mathbf{C} + \mathbf{K})^{-1}\hat{\mathbf{f}} = \mathbf{H}(\omega)\hat{\mathbf{f}} \tag{5.1}$$

where,

$$\mathbf{H}(\omega) = (-\omega^2\mathbf{M} + j\omega\mathbf{C} + \mathbf{K})^{-1} \tag{5.2}$$

is the frequency response function matrix of the whole structure. The size of $\mathbf{H}(\omega)$ matrix is $N \times N$ for each value of the driving frequency ω. Hence, the evaluation of $\mathbf{H}(\omega)$ is computationally exhaustive if N is large. In many practical cases, response for a particular degree-of-freedom is required. In those cases, the response $\mathbf{q}$ can be obtained by solving the set of linear algebraic equations, in the form $(-\omega^2\mathbf{M} + j\omega\mathbf{C} + \mathbf{K})\hat{\mathbf{q}} = \hat{\mathbf{f}}$, [modified form of equation (5.1)], without explicitly inverting the whole matrix $\mathbf{H}(\omega)$. Even this response calculation is computationally expensive for structures with large N.

In order to reduce the computational expense associated with the response calculations, a reduced order model with p number of pre-conditioned assumed modes will be built, where $p \ll N$. The method of obtaining the continuum modes is described in Chapter 4 which uses kinematic mapping of the cheaply calculated continuum free vibration modes onto the joints of the cells in a cellular model. When these modes were employed in model order reduction directly, the method performed poorly due to the presence of small contributions from high frequency modes. Therefore, filtering of these undesirable modes was carried out using inverse power iterations as in case free vibration calculations.

Let us assume that the motion of the structure at any time t can be approximated

by the superposition of p number of assumed modes ψ as

$$\phi(t) = a_1\psi_1 + a_2\psi_2 + ... + a_n\psi_p, \quad p \ll N \tag{5.3}$$

where, a_1, a_2, ..., a_p are time-dependent generalised co-ordinates of the structure. This expansion can be expressed by the following transformation

$$\boldsymbol{\phi} = \mathbf{Ta} \tag{5.4}$$

where, $\mathbf{T}$ is the transformation matrix of size $N \times p$, whose columns are the assumed modes $\psi_i, i = 1, 2, ..., p$

$$\mathbf{T} = [\psi_1|\psi_2|...|\psi_p] \tag{5.5}$$

and $\mathbf{a}$ is a column of unknowns a_1, a_2, ..., a_p. Note that the transformation matrix $\mathbf{T}$ has a structure similar to that of the modal matrix but it contains only p number of modes. In addition, these p modes are only approximate unlike the modal matrix where they are exact.

The kinetic energy $T(t)$ and the potential energy $V(t)$ of the whole structure can be expressed as

$$T(t) = \frac{1}{2}\dot{\boldsymbol{\phi}}^T\mathbf{M}\dot{\boldsymbol{\phi}}, \quad V(t) = \frac{1}{2}\boldsymbol{\phi}^T\mathbf{K}\boldsymbol{\phi}. \tag{5.6}$$

Substituting the transformation (5.4) in the above expressions of T and V and simplifying, we obtain

$$T(t) = \frac{1}{2}\dot{\mathbf{a}}^T\overline{\mathbf{M}}\dot{\mathbf{a}}, \quad V(t) = \frac{1}{2}\mathbf{a}^T\overline{\mathbf{K}}\mathbf{a} \tag{5.7}$$

where, $\overline{\mathbf{M}} = \mathbf{T}^T\mathbf{MT}$ and $\overline{\mathbf{K}} = \mathbf{T}^T\mathbf{KT}$. The matrices $\overline{\mathbf{K}}$ and $\overline{\mathbf{M}}$ will be referred to as the reduced stiffness and the inertia matrices respectively because of their reduced size $p \times p$.

Damping, assumed to be derivable from the Rayleigh's dissipation function, can be expressed similarly as (2.6),

$$\mathcal{F} = \frac{1}{2}\dot{\boldsymbol{\phi}}^T\mathbf{C}\dot{\boldsymbol{\phi}}. \tag{5.8}$$

Using transformation (5.4), this expression reduces to

$$\mathcal{F} = \frac{1}{2}\dot{\mathbf{a}}^T\overline{\mathbf{C}}\dot{\mathbf{a}}. \tag{5.9}$$

where $\overline{\mathbf{C}}$ is the reduced damping matrix of size $p \times p$. If $\overline{\mathbf{Q}}$ is the generalised viscous damping force for the reduced model, then it can be derived from the Rayleigh's dissipation function as

$$\overline{Q}_r = -\frac{\partial\mathcal{F}}{\partial\dot{a}_r}, \quad r = 1, 2, ..., p. \tag{5.10}$$

The variation of the non-conservative work done by all other forces other than the viscous forces (for the full model) is expressed as

$$\delta W_{nc} = \sum_{r=1}^{N} f_r \delta \phi_r. \tag{5.11}$$

Substituting for ϕ_r from equation (5.4) and simplifying we obtain

$$\delta W_{nc} = \sum_{r=1}^{N} f_r \left(\sum_{s=1}^{p} T_{rs} \right) \delta a_s. \tag{5.12}$$

If $\overline{\mathbf{f}}$ is the vector of the generalised forces corresponding to the reduced model of the structure producing the generalised displacements $\mathbf{a}$, then the variation of the non-conservative work done is given by

$$\delta W_{nc} = \sum_{s=1}^{p} \overline{f}_s \delta a_s. \tag{5.13}$$

Since the virtual work done is the same for both the systems, we obtain,

$$\overline{f}_s = \sum_{r=1}^{N} f_r T_{rs}, \quad s = 1, 2, ..., p. \tag{5.14}$$

Lagrange's equation of motion in terms of the new set of generalised co-ordinates and generalised forces, a_i and $\overline{f}_i$, can be written as

$$\frac{d}{dt}\left(\frac{\partial L}{\partial \dot{a}_i} \right) - \frac{\partial L}{\partial a_i} + \frac{\partial \mathcal{F}}{\partial \dot{a}_i} = \overline{f}_i, \quad i = 1, 2, ..., p, \tag{5.15}$$

where $L = T - V$ is the Lagrangian of the structure.

Substituting expressions of (5.7) into equation (5.15), we obtain the following set of equations of motion in the matrix form

$$\overline{\mathbf{M}}\ddot{\mathbf{a}} + \overline{\mathbf{C}}\dot{\mathbf{a}} + \overline{\mathbf{K}}\mathbf{a} = \overline{\mathbf{f}}. \tag{5.16}$$

If the generalised force $\overline{\mathbf{f}}$ is of the form $\overline{\mathbf{f}} = \hat{\mathbf{f}}_{red} e^{j\omega t}$, then the generalised response $\mathbf{a}$ can be expressed as $\mathbf{a} = \hat{\mathbf{a}} e^{j\omega t}$. Substituting for $\overline{\mathbf{f}}$ and $\mathbf{a}$ in equation (5.16), we have

$$\hat{\mathbf{a}} = (-\omega^2 \overline{\mathbf{M}} + j\omega \overline{\mathbf{C}} + \overline{\mathbf{K}})^{-1} \hat{\mathbf{f}}_{red}, \tag{5.17}$$

which is similar to the previous expression (5.1). Hence, the approximate frequency response function matrix is given by

$$\overline{\mathbf{H}}(\omega) = (-\omega^2 \overline{\mathbf{M}} + j\omega \overline{\mathbf{C}} + \overline{\mathbf{K}})^{-1}. \tag{5.18}$$

The coefficient matrices $\overline{\mathbf{M}}$, $\overline{\mathbf{K}}$ and $\overline{\mathbf{C}}$ are of size $p \times p$, which is much smaller than the original size of $N \times N$ if we are interested in a frequency band spanned by the first few frequencies. Hence, the calculation of $\overline{\mathbf{H}}(\omega)$ needs much less computational effort than evaluating $\mathbf{H}(\omega)$. The displacement field at each node of the cellular structure $\boldsymbol{\phi}$ can be calculated from equation (5.3) after evaluating the values of the a's by solving (5.17).

§5.2.1 Proportional Damping

It is extremely difficult to measure the damping of individual cell walls. In the absence of any damping model for the constituent parts, proportional or classical damping has been used. Expressing the damping matrix as a linear combination of the stiffness matrix and the mass matrix, we have

$$\mathbf{C} = \alpha\mathbf{M} + \beta\mathbf{K}. \tag{5.19}$$

Substituting $\mathbf{C}$ and $\boldsymbol{\phi}$ into (5.8) and simplifying the expression for Rayleigh's dissipation function becomes

$$\mathcal{F} = \frac{1}{2}\dot{\mathbf{a}}^T(\alpha\overline{\mathbf{M}} + \beta\overline{\mathbf{K}})\dot{\mathbf{a}}. \tag{5.20}$$

Comparing this with equation (5.9), the reduced order damping matrix is obtained as

$$\overline{\mathbf{C}} = \alpha\overline{\mathbf{M}} + \beta\overline{\mathbf{K}}. \tag{5.21}$$

A commonly encountered difficulty while using the Rayleigh damping model is the lack of a rational approach to obtain the damping coefficients α and β. In this dissertation, calculations based on *prescribed* values of the damping ratio at the terminal points of the frequency band of interest are presented. This specification leads to two algebraic equations for the two unknowns α and β.

The eigenvectors $\mathbf{u}$ for any structure can be calculated solving the eigenvalue problem, $\mathbf{K}\mathbf{u}_r = \lambda_r\mathbf{M}\mathbf{u}_r$, equation (2.11). The eigenvectors are stacked to obtain the modal matrix as $\mathbf{U} = [\mathbf{u}_1|\mathbf{u}_2|....|\mathbf{u}_N]$. If the eigenvectors are orthonormal then, they satisfy the following relationships

$$\mathbf{U}^T\mathbf{M}\mathbf{U} = \mathbf{I}, \quad \mathbf{U}^T\mathbf{K}\mathbf{U} = \text{diag}[\omega_r^2] \quad r = 1, 2, ..., N. \tag{5.22}$$

$\mathbf{U}^T\mathbf{C}\mathbf{U}$ is a diagonal matrix for proportional damping and is given by

$$\mathbf{U}^T\mathbf{C}\mathbf{U} = \text{diag}[2\zeta_r\omega_r] \tag{5.23}$$

where, ζ_r is the damping ratio for the r-th mode. Using (5.19), and the orthogonality conditions, (5.22), we obtain

$$\mathbf{U}^T\mathbf{C}\mathbf{U} = \alpha\mathbf{I} + \beta\text{diag}[\omega_r^2] \quad r = 1, 2, ..., N. \tag{5.24}$$

Equating the right side of the two expressions in equations (5.23) and (5.24), we obtain the frequency dependence of the damping ratio as

$$\zeta_r = \frac{\alpha}{2\omega_r} + \frac{\beta\omega_r}{2} \quad r = 1, 2, ..., N. \tag{5.25}$$

If the value of ζ is specified at the two extremes of a frequency band, then we obtain two equations for the unknowns α and β. Solving for these unknowns determines the two parameters required in the Rayleigh damping model.

Carrying out algebra on the lines of equations (5.22) through to (5.25) we obtain the expression for the damping ratios for the reduced model as

$$\overline{\zeta}_r = \frac{\alpha}{2\overline{\omega}_r} + \frac{\beta\overline{\omega}_r}{2}, \quad r = 1, 2, ..., p \tag{5.26}$$

where $\overline{\zeta}_r$ and $\overline{\omega}_r$ denote the damping ratio and the natural frequency corresponding to the r-th mode of the reduced model. The above expression is used here for the determination of the damping ratios as predicted by the reduced order model. This expression shows that the quality of estimates for the damping ratio depends upon the accuracy of the natural frequencies predicted by the reduced order model.

§5.3 A numerical example and discussions

The cantilever beam shown in figure 3.12 is taken up in this section to illustrate the continuum model based calculations of the frequency response functions. The global stiffness matrix $\mathbf{K}$ and the global inertia matrix $\mathbf{M}$ of the beam are calculated as before. Continuum modes were calculated in section 4.4 for the approximate free vibration calculation for the beam. These continuum modes were evaluated from the finite element analysis of the single fixed-free beam having the same macroscopic dimensions as the cellular beam. The assumed modes were calculated from these modes through mapping on the lines of equation (4.3) using equations (4.1) and (4.2). These assumed modes were chosen as the basis modes after pre-conditioning using equation (4.26). The first ten assumed modes are used here for calculation of the approximate response. The undamped response is considered in the next section, followed by the damped response in the subsequent section.

§5.3.1 Undamped response

A harmonic force $\hat{\mathbf{f}}e^{j\omega t}$ is applied to a node near the neutral axis since it is practically not possible to find a node on the neutral axis when irregular cells are present. Coefficient matrices and the force vector for the reduced model $\overline{\mathbf{K}}$, $\overline{\mathbf{M}}$ and $\overline{\mathbf{f}}$ are calculated using equations (5.7) and (5.14). The unknowns a_r are determined by solving equation (5.17) without explicit inversion. The complete displacement field is obtained by the transformation (5.3) after substituting the values of a_r. The driving point and the transfer

receptances of the reduced order model are compared with those obtained from the full scale finite element simulations.

The vertical displacement of a point is calculated due to a harmonic vertical load acting upon it. The amplitude of the driving point receptance calculated from the full scale model is compared with the calculations based on the reduced order model in figure 5.1. The frequency band chosen here contains ten modes of the finite element model. The point response shows similar features as is observed in the case of a homogeneous continuum. The finite height of the peaks is due to the finite resolution of the frequency stepping. The figure shows an excellent agreement– the error being less than 1% up to the ninth mode. The response curve starts deviating progressively after the ninth peak. The tenth frequency estimated by the reduced model is higher by 7% than the corresponding value calculated by the full scale finite element analysis. The accuracy of the tenth frequency can be improved by including more number of basis modes instead of including only ten. However, when the wavelength approaches the cell size, inclusion of more number of basis modes cannot predict the response well as the method fails.

It is expected that the overall motion of the structure will be primarily vertical when the load is applied vertically. This can lead to missing modes that are associated with non-vertical motion. Figure 5.1 shows the axial mode between the third and the fourth peaks at 102.51 Hz missing. On the other hand the eighth peak in this figure corresponds to an axial mode which is possibly due to small bending axial mode coupling afforded by the irregular microstructure.

There is an anti-resonance between any two resonances in figure 5.1. This is characteristic of a driving point response. At the anti-resonance, the displacement of the driving point is zero. This can be viewed as a constraint applied to the system. It is known from the Rayleigh's principle that if a constraint is applied to a system keeping everything is the same, the natural frequencies of the system are increased. Let λ_1, λ_2,..., λ_N be the natural frequencies of the system. Similarly, suppose that μ_1, μ_2,..., μ_{N-1} are the frequencies corresponding to the constrained system. Then from the inclusion theorem we have,

$$\lambda_1 \leq \mu_1 \leq \lambda_2 .... \lambda_{N-1} \leq \mu_{N-1} \leq \lambda_N. \tag{5.27}$$

Since anti-resonances are resonances of a constrained system, it follows that resonances and anti-resonances interlace for driving point response.

The driving point receptance due to *axial* loading is presented next. Figure 5.2 shows the comparisons of the amplitude of the point receptance as calculated from the full scale

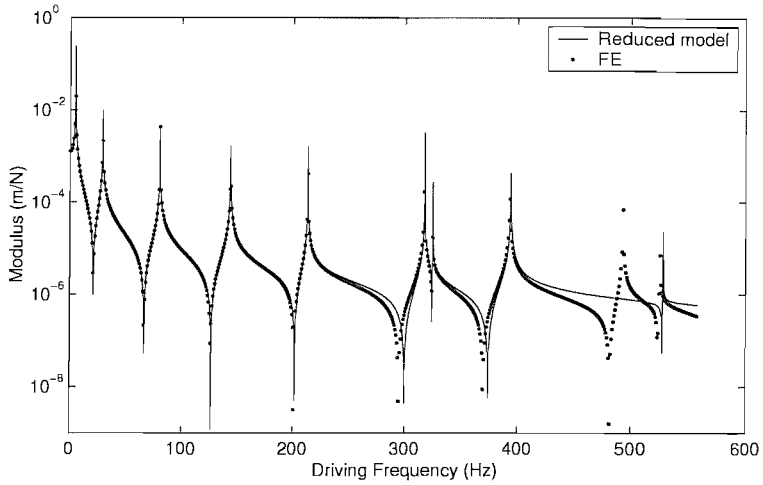

Figure 5.1: Driving point receptance as calculated from the finite element analysis using the full scale model compared with that of the reduced order model. Response is calculated due to a harmonic vertical load acting at a boundary node. Note that the peak associated with the first *axial* mode between the third and the fourth peaks is missing. The agreement is excellent up to the ninth mode. Anti-resonances are observed between any two resonance peaks as expected.

finite element analysis and the reduced order model. The agreement is generally good. Note that the axial mode missing in figure 5.1 at 102.51 Hz is the dominant peak now. Peaks associated with the axial modes are more pronounced now. Small resonance peaks associated with the flexural modes are observed in addition to the axial modes. This can be attributed to small coupling introduced by the irregularity.

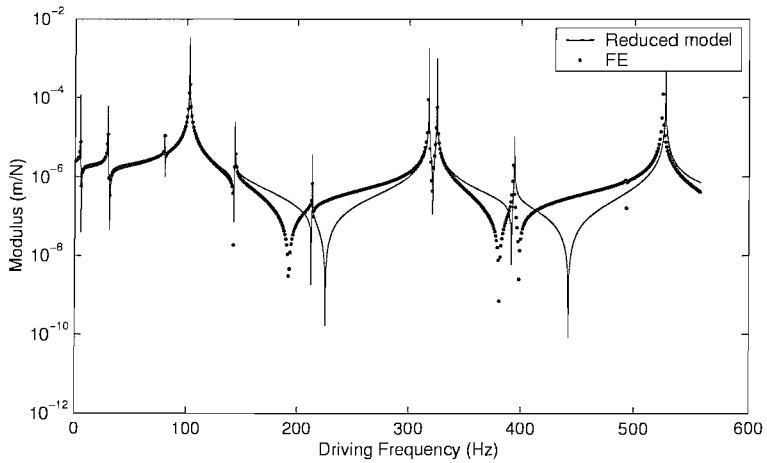

Figure 5.2: Undamped driving point response when a harmonic axial load acts at a boundary node. The response is evaluated from the full scale model as well as the reduced order model. Sharp resonance peaks are observed at the frequencies corresponding to the axial modes. The first axial mode missing in figure 5.1 is prominent now.

The transfer receptance is calculated next when the driving point is unchanged and the response point is a cell junction close to the centre of the sample (co-ordinates 30.56 mm, 5.36 mm). Driving as well as response are in the vertical direction. The transfer response is shown in figure 5.3. Again the full scale calculations are compared with the proposed approximation based on the continuum modes. The agreement is again very satisfactory up to the ninth mode.

Resonance peaks are observed at the frequencies corresponding to the flexural modes just as they were observed in the point receptance. The resonance associated with the first axial mode is missing again. In the case of the point receptance, resonances and anti-resonances were observed alternately. Such a pattern of response is not observed now. For example, no anti-resonance is observed between the first and the second or the second and the third resonance peaks. The transfer receptance, when the driving as well as the response directions are changed to axial, is shown in figure 5.4. The quality of match between full scale calculations and the continuum modes based approximation is again very good.

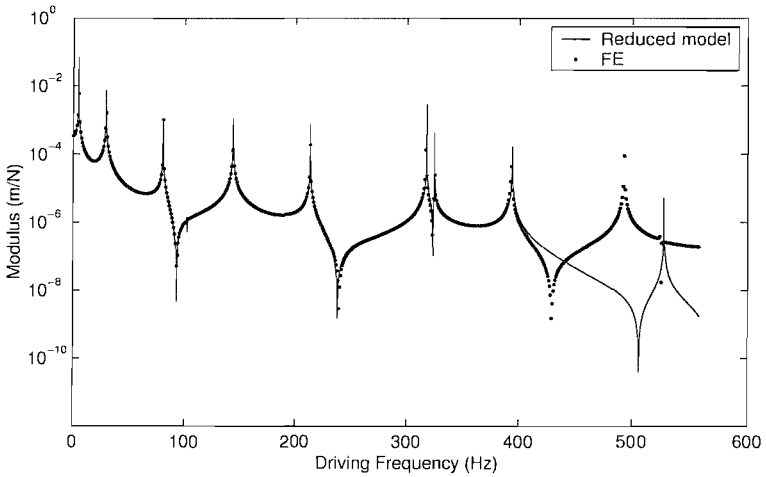

Figure 5.3: Undamped transfer receptance for the full scale model and the reduced order model due to a vertical load applied at the right hand boundary node. Note the absence of the anti-resonances between the resonance peaks in many cases. This a characteristic of transfer receptance.

The response at a point of the structure is plotted so far. Now, the spatial response the structure as estimated by the reduced model will be compared with that from the full model. The FDAC (Frequency Domain Assurance Criteria) is used here for correlating the response vectors $\boldsymbol{\phi}$ and $\mathbf{q}$ in the frequency domain. The plot is similar to the MAC plot used in sections 4.4.1 and 4.4.2 for comparing the eigenvectors. In the present case,

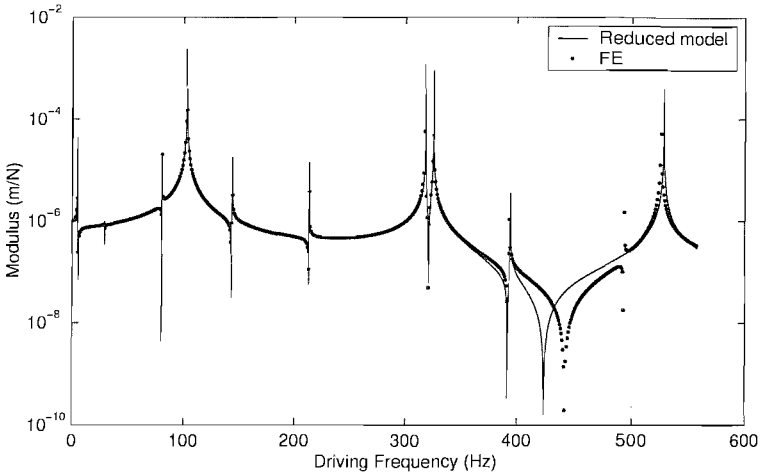

Figure 5.4: Undamped transfer receptance plotted on the lines of figure 5.3. The driving direction is axial now.

it is impossible to compare the vectors at all the possible values of the driving frequency. Hence, the response functions are calculated at some representative frequencies only. In this thesis, the calculations are performed for all the natural frequencies and the mid-points between two adjacent modes on the frequency axis. The frequency band considered here has the first ten modes of the full scale model. Therefore, 20 pairs of vectors, ϕ and $\mathbf{q}$ are generated for the FDAC plot.

The FDAC matrix $\mathbf{F}$ has the entries given by [28]

$$F_{rs} = \frac{|\mathbf{q}_r^T \boldsymbol{\phi}_s|^2}{(\mathbf{q}_r^T \mathbf{q}_r^*)(\boldsymbol{\phi}_s^T \boldsymbol{\phi}_s^*)}. \tag{5.28}$$

The asterisk denotes the complex conjugate. In the absence of damping, the response vectors are real. Figure 5.5 shows the relative magnitudes of F_{rs} for the pair of response vectors on a suitable grey-scale. The dark diagonal cells on this plot show excellent correlation between the spatial response as calculated by the full scale model and that as calculated by the reduced order model.

In order to compare the computational savings, the number of floating point operations involved in both the approximate method and the finite element method are calculated when a vertical load is applied at a boundary node. A frequency interval of of 0.16 Hz is considered which involves calculation of the response vector (3444 × 1) 3500 times. The total floating point operations required for calculations using the reduced model and the finite element model are 2.61×10^8 and 2.63×10^{10} respectively. This indicates that the flops for the reduced model are only 1% of those required for the full scale model. Note that the flop counts for the reduced model includes the generation of

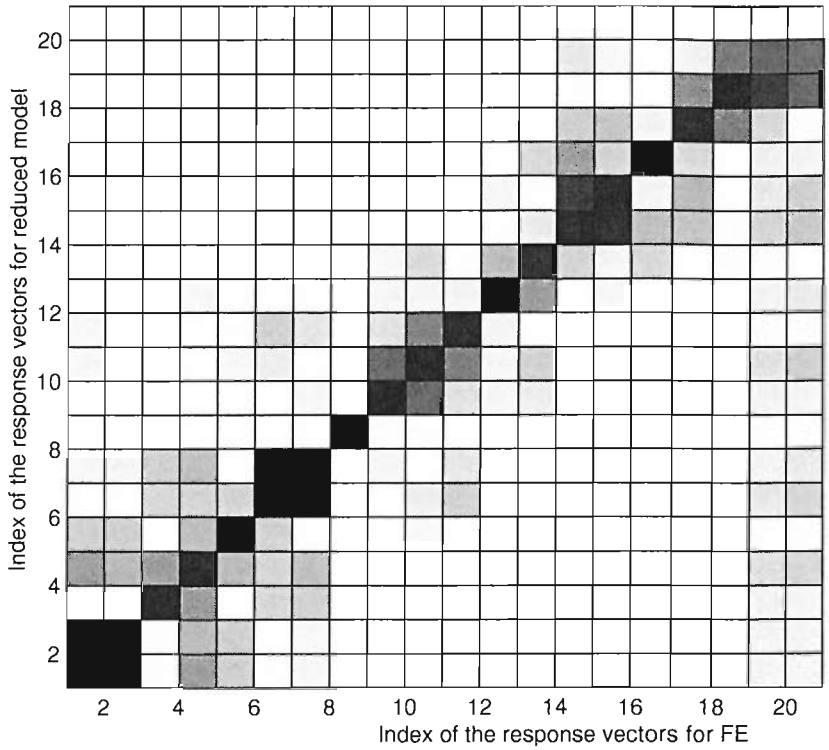

Figure 5.5: FDAC plot representing correlation between the response vectors as calculated by the finite element simulations and the reduced model. The dark blocks on the diagonal show excellent correlation up to the ninth mode.

the assumed modes, the modes of the skeleton and preconditioning etc. The assembly of the coefficient matrices is included in both the cases.

§5.3.2 Damped response

The model analysed in the previous section is taken up now when damping is included in the model via Rayleigh damping. It is unclear how the damping ratios will be predicted when the model order reduction scheme proposed in Chapter 4 is employed. Potentially, a mismatch in the effective damping ratio can seriously affect response near the resonances. To investigate these issues, numerical results from the damped model are presented in this section.

The value of the damping ratio ζ is taken as 1% for the first and the tenth mode. The values of the constants α and β are then calculated by solving the two simultaneous equations using (5.25) for this chosen value of ζ. The values of α and β evaluated as above are 0.596 s^{-1} and 6.39×10^{-6} s respectively. The reduced damping matrix $\overline{\mathbf{C}}$ is then generated as $\alpha\overline{\mathbf{M}} + \beta\overline{\mathbf{K}}$. The response is calculated using equation (5.17).

The point receptance is presented in figure 5.6 when a vertical point load is applied to a node close to the centre line. The agreement is excellent agreement up to the ninth mode. This shows that the reduced damping matrix accurately captures the damping behaviour of the full scale model. The seventh mode is an axial mode which is also reproduced by the reduced order model since the basis modes include the axial continuum mode. Again, anti-resonances are observed between any two resonance peaks– a characteristic of driving point response. The phase is also reproduced accurately by the reduced order model.

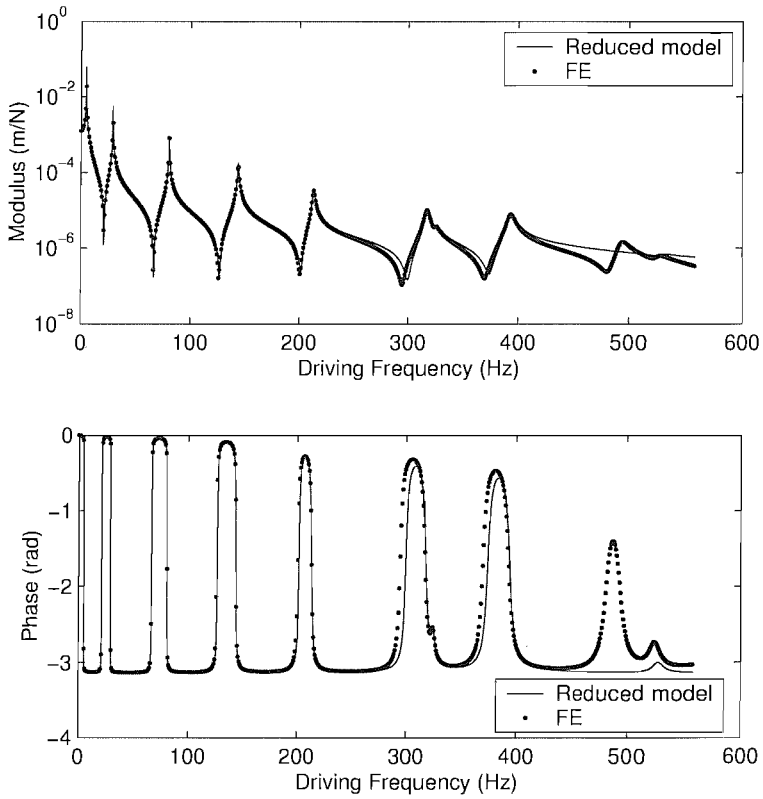

Figure 5.6: Driving point receptance due to a vertical load acting at a boundary node. Damping is included in the model. The response curves have the similar features as was observed in figure 5.1, with the difference is that the resonance peaks are now reduced due to damping.

Equations (5.25) and (5.26) are used to determine the damping ratios for the full scale and the reduced model respectively. These values of ζ are plotted in figure 5.7. The figure shows that the damping ratios are well predicted by the reduced model up to the ninth mode.

The driving point response is shown in figure 5.8 when the loading and response measurement are axial. The response calculated from the full scale model matches

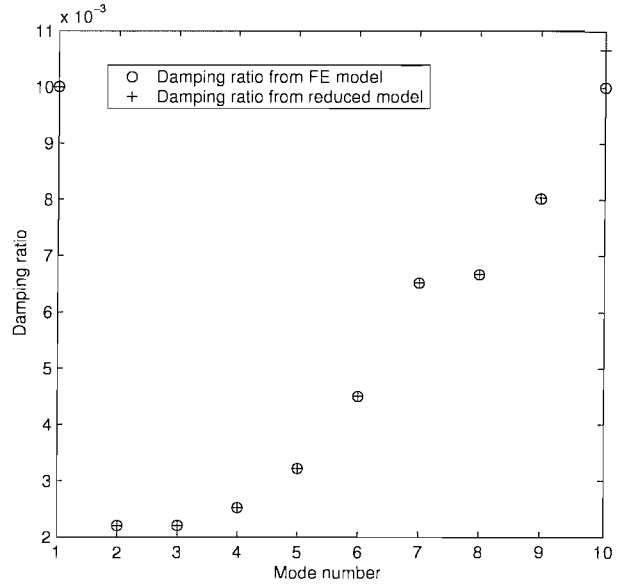

Figure 5.7: A plot of the damping ratio (ζ_r) against mode number. The ratios estimated on the basis of the reduced model are very accurate except for the last mode.

closely with the continuum mode approximation for a reasonable band of frequencies. The match is less satisfactory than the case of bending because of the lack of axial continuum modes in the frequency band under consideration. Again the height of the peaks are matched fairly accurately showing a good agreement in the damping ratio for the respective modes. The phase shows a generally good agreement too. The magnitude and the phase of the approximate transfer response calculations also match well with the finite element calculations (see figure 5.9).

The FDAC matrix $\mathbf{F}$ is generated for both the response vectors $\mathbf{q}$ and ϕ for the comparisons of the damped response of the whole structure. The response functions are calculated at the same frequencies as was evaluated in the undamped case. Note that both the vectors are complex in this case because of damping. The FDAC matrix $\mathbf{F}$ is plotted in figure 5.10. The dark blocks on the diagonal show good correlation except the last mode.

The total floating point operations required for the full scale and the reduced model calculations are 1.03×10^{11} and 9.99×10^{8} respectively. Therefore, flops for the reduced model are less than 1% than that required for the full model. The computational savings will be even greater when more number of response functions are to be calculated and when the size of the problem is larger.

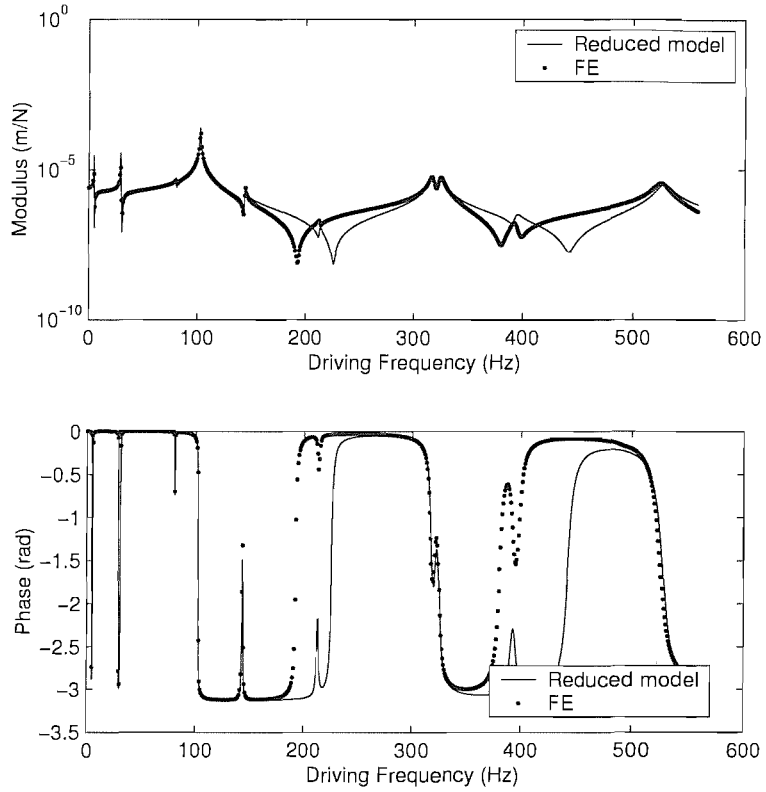

Figure 5.8: Driving point receptance due to harmonic axial load when damping is included in the model.

§5.4 Conclusions

A method was proposed for the estimation of frequency response of cellular structures. The main motivation was to reduce the computational expense associated with the response calculations for such structures without compromising the accuracy. The pre-conditioned continuum modes were used as the basis for the model order reduction. The response of the whole structure was predicted using the reduced order model.

A proportional damping model was proposed to include the effect of damping. The damping co-efficients associated with the stiffness and the inertia matrices were calculated for a frequency bandwidth when the value of the damping ratio was prescribed for the two extremes of the band.

The response predicted by the proposed method was compared with that calculated from the full scale model. The comparisons showed good agreement for the damped as well as the undamped cases. The reduced order model predicts fairly accurate damping ratios. Without comprising the accuracy significantly, substantial computational saving was achieved when continuum modes are used for model order reduction. The limitation

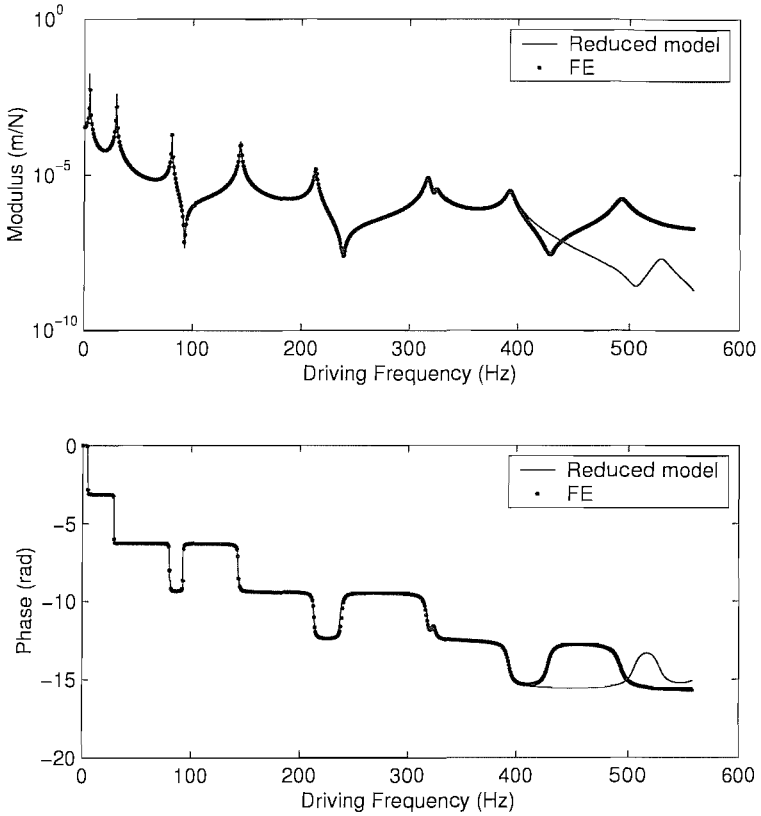

Figure 5.9: Comparison of the transfer receptance when the load is vertical. Damping is included in the model.

of the proposed model order reduction is that it is suitable only for the low frequency dynamics.

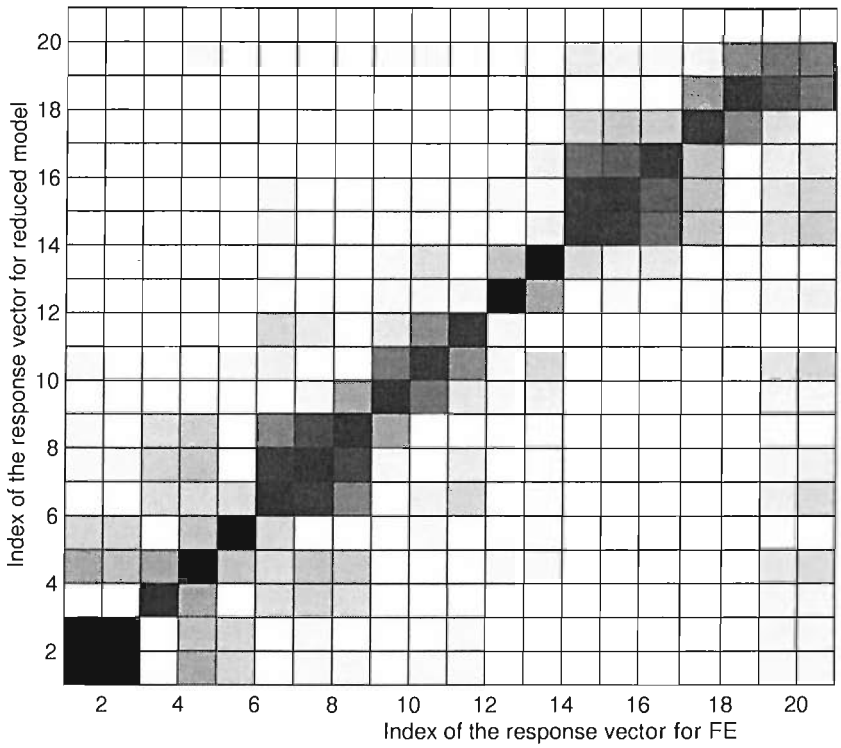

Figure 5.10: FDAC plot representing correlation between the damped response vectors. The dark blocks on the diagonal show excellent correlation up to the ninth mode.

Chapter 6

Experimental determination of the effective modulii of metallic foams and their dependence on mode number

§6.1 Introduction

An experimental study on the dynamic behaviour of metallic foams is undertaken in this chapter. Given the overall dimensions of a sample (say a thin rectangular bar), the effective Young's modulus can be worked out by using the well known frequency formula for beams in bending. If we assume that a piece of metal foam indeed behaves as an equivalent continuum, then the value of the modulus must be calculated the same from all the modes of vibration. To ensure that the higher order effects such as the shear correction, rotary inertia etc. are kept out of consideration, geometrical differences were eliminated by performing experiments on solid samples of the same external dimensions as those of the metallic foam sample. It may be recalled that the effects are dominated by geometry; i.e. a slender sample will increasingly mimic an Euler-Bernoulli beam behaviour. Having performed experiments on metallic foam samples as well as solid samples, a mode by mode comparison will be made for the effective Young's modulus. To achieve this, all the values will be normalised with respect to the measured fundamental frequency– this provides an opportunity to study the modal separation for metallic foams experimentally and to compare it with that of a solid sample.

Among the previous experimental investigations on cellular matter, only those related to the mechanics of metallic foams are cited here. Simone et al. [91] studied the effect of imperfections on the elastic modulus and strength of Alporas^{TM} foam. McCullough et al. [70] performed static tensile and compressive test for calculating the uni-axial stress-strain behaviour of Alulight^{TM}. Ramamurthy et al. [83] studied the variability of the elastic modulus, the plastic strength, and the energy absorption in Alporas on foam density. However, experimental studies on the dynamic behaviour of metallic foams has received little attention. Dynamic experiments have been used in the past for evaluating the elastic constants of ceramic and dental materials [4, 56, 94]. The present work is perhaps the first attempt to determine the Young modulus as well as the Poisson's ratio of metallic foams. Certainly, a mode by mode variation of the effective modulus has not been reported previously.

Commercially available closed cell metallic foam Alulight^{TM} was chosen for the experimental work. This choice was guided by the feasibility of performing dynamic experiments. Open cell foams were kept out of consideration from the experimental work because of their low effective density and high internal damping they are not suitable for meaningful observations. In addition, instrumentation using accelerometers on open cell foams is difficult.

The approach of obtaining modulii from vibration experiments has several advantages over static testing. Firstly, the frequencies are obtainable for very low amplitudes of vibration which is desirable for eliminating any geometric or material non-linearities. Secondly, the natural frequencies reflect the overall elastic behaviour unlike static tests in which local structural details may dominate. Thirdly, experimental determination of the Poisson's ratio from static experiments is much more difficult compared to that from the dynamics experiments. Finally, the objective of this work is to examine the validity of the effective medium theories in dynamics which requires estimation of the modulii for various excitation frequencies. This can come only from a vibration experiment. In the next section, the experimental set up and the general experimentation method are described. This is followed by the determination of the elastic modulii and a study on the modal separation in section 6.3. Conclusions are drawn in section 6.4.

UNIVERSITY OF SOUTHAMPTON LIBRARY

§6.2 The experimental procedure

The experimental set up is shown in figure 6.1. The figure shows a sample horizontally suspended. The suspension cords were chosen sufficiently long to ensure that the oscil-

lation frequency associated with the free swing as a rigid body was much smaller than the structural frequencies of interest. When the frequency of the rigid body swing is much smaller than the fundamental structural frequency, the sample can be practically considered to be in free-free conditions. Suspension by a cord has the advantage over soft supports (e.g. sponge) that it is practically lossless and the suspension stiffness can be altered easily by changing the cord length. In many cases a vertical suspension of the samples was also employed (not shown in the figure).

Impulse using an instrumented hammer was the preferred method of excitation. The primary interest was in measuring the natural frequencies of the test samples. An elaborate scheme for modal identification was avoided since the quantities of interest were fairly basic. For example, complete mode shapes were not determined, but information regarding mode shapes was inferred using simple means such as placing the accelerometer at various locations to locate the nodes and the anti-nodes. The samples chosen here were in the form of a beam with length/depth ratio greater than 10. The beam was hung freely in a vertical or in a horizontal position as it was found to be convenient. Any clamping of the structure was avoided since it is difficult to realise this boundary condition in the laboratory.

Excitation and sensor locations were chosen to be the end points in many cases. This ensures that no modes are missed out because the free ends are anti-nodes for all the modes for a rectangular bar. On many occasions, the location of the excitation and/or sensing was altered to identify the nodes and anti-nodes of specific modes. The fact, that one would get a large response when a driving point measurement is made at an anti-node and a negligible response near a node, was used to identify the mode types in the measured frequency response functions. This strategy was also used to separate the bending modes from the torsional modes. Torsional modes were further confirmed by checking the phase at the opposite edges of a face.

To ensure that the measured response actually represents a driving point measurement, the excitation and the accelerometer locations were kept as close as possible. The data logging equipment and the software convert the analog data to the digital form after suitable amplification and compute the Fast Fourier Transform (FFT) of forcing as well as the response. The ratio of the FFTs of the response to that of forcing gives the frequency response function (FRF).

The impulse hammer used to excite the samples was PCB make ICP^{TM} (Integrated circuit– piezoelectric, model no. 086C01). The weight of the hammer is 25 gm and the

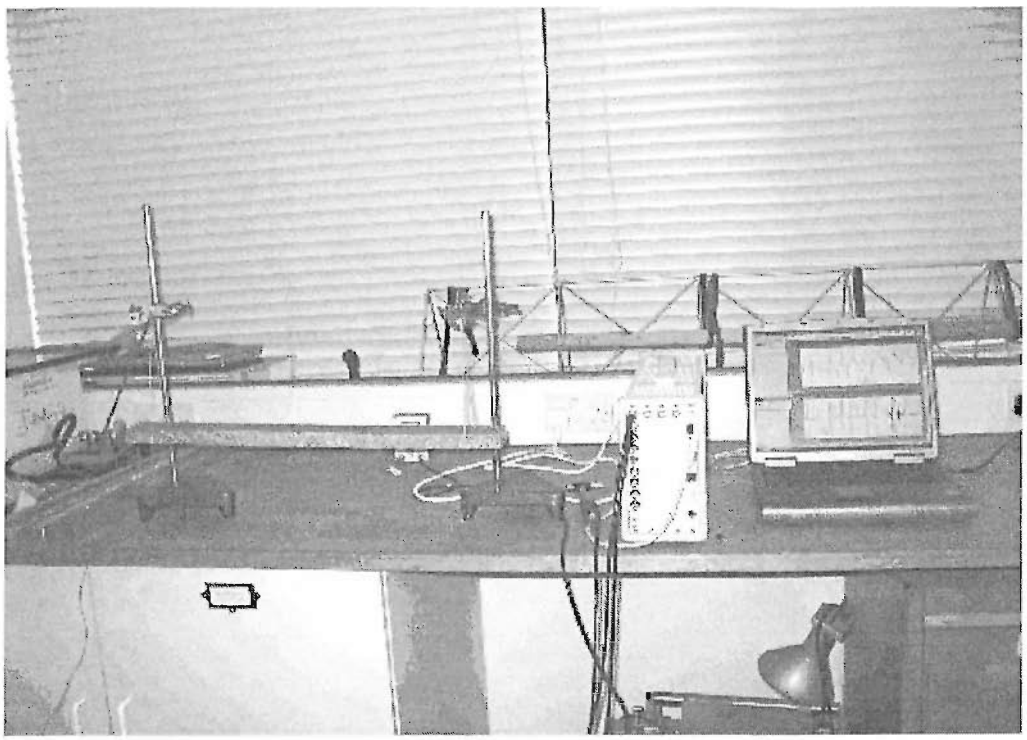

Figure 6.1: The experimental set-up. The beam is suspended horizontally using two cords, which simulate the free-free boundary condition. The data-logger and the visual display unit (laptop) are also shown.

sensitivity is 11.2 mV/N. To keep a balance between the low weight and the sensitivity of the transducer, PCB make ICP^{TM} accelerometers (model no. 352C22) were used. An accelerometer weighs 0.5 gm and has a sensitivity of 9.30 mV/g. Petro wax adhesive was used for mounting the accelerometers on the foam surface. The first resonant frequencies of the hammer and the accelerometer are 35 kHz and 50 kHz respectively. This ensured that data up to 20 kHz band can be captured safely. A 8-channel data-logger, Dataphysics Signalcalc Mobilyzer, was used for the experiment. It supplied the 4mA current needed to operate each ICP^{TM}.

In a practical measurement, in addition to bending and torsional modes, the axial modes also appear. To confirm this type of mode, the beam was excited axially. The resonance peaks corresponding to the axial modes then become pronounced. This excitation method gives a series of modes in axial extension and compression from which the effective modulii can be deduced.

Figure 6.2 shows two different positions of excitation on a beam having a rectangular cross-section. For position 1, i.e. when the beam is excited near the midpoint, the tor-

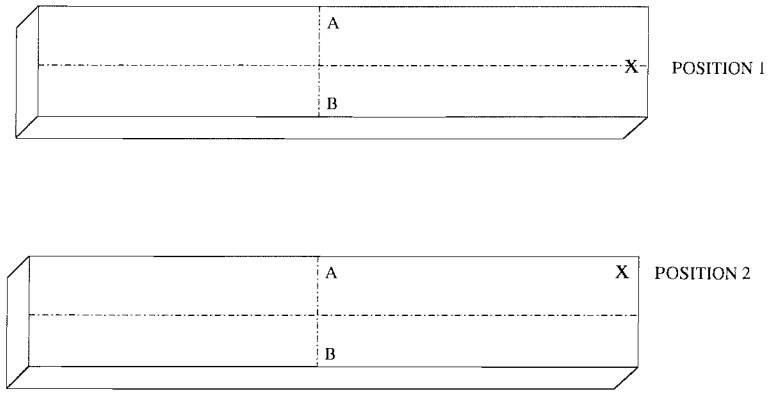

Figure 6.2: The positions 1 and 2 of the excitation. Position 1 is suitable for exciting the flexural modes while position 2 is suitable for torsional modes.

sional modes are excited along with the bending and the axial modes; but the resonance peaks corresponding to the torsional modes are small. When the driving point measurement is shifted to position 2 (see figure 6.2), the torsional modes are pronounced. Torsional modes were further confirmed by making phase measurements when the driving point and the sensing point are different. The motion is in-phase at the opposite edges of the face for bending modes whereas it is out-of-phase for torsional motion. Additional features of the torsional mode were used for confirmation of the mode type: for example, the fundamental torsional mode has an anti-node at the centre-line AB.

§6.3 Results and discussions

A macrograph of the a specimen of Alulight foam is shown in figure 6.3. As can be seen from this figure, the cells do not have any particular shape and they are randomly distributed. The average cell size for Alulight foams is reported elsewhere as 4.2 mm [3]. The average ratio of the length of the major axis and minor axis of cells has been reported to be close to 1 [3]. Therefore, macroscopically we do not expect any directional preference in the elastic properties.

The geometrical parameters of the two samples of the foam are shown in table 6.1. The length/depth ratio for each beam is about 25. The cross-section of the beam is rectangular, with the overall depth/width ratio approximately being 2.44. The samples used for experimental work were the longest possible. This was dictated by the manufacturer's constraints.

FRFs are calculated from the measurements of the applied impulse and the acceleration. A typical impulse and its FFT are shown in figure 6.4. Double impacts were

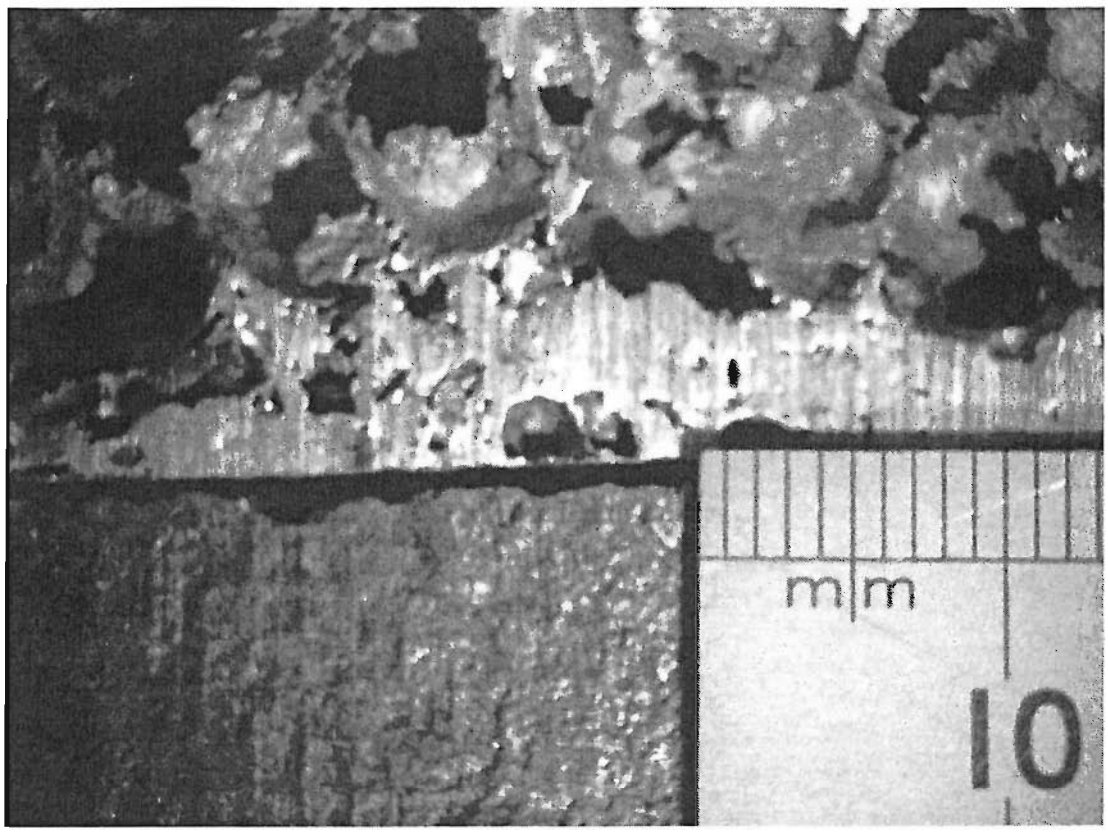

Figure 6.3: A macrograph of a sample of Alulight foam.

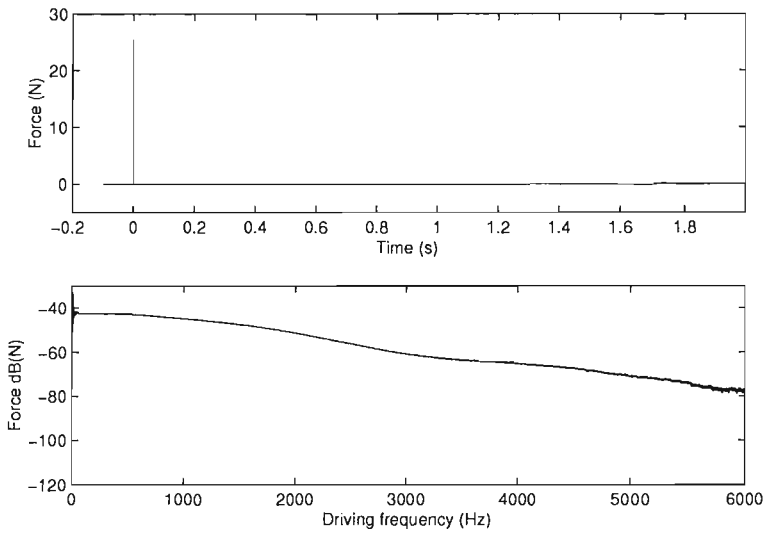

Figure 6.4: A typical experimental impulse and the magnitude of its FFT are shown.

Sample 1	
Length of the beam L	625 ± 1 mm
Overall depth in the transverse direction D	24.1 ± 0.1 mm
Width of the beam B	60.4 ± 0.1 mm
Density of the foam ρ^*	370.54 ± 0.007 kg/m^3
Volume fraction of the foam ρ^*/ρ_s	0.137
Sample 2	
Length of the beam L	625 ± 1 mm
Overall depth in the transverse direction D	24.1 ± 0.1 mm
Width of the beam B	59.5 ± 0.1 mm
Density of the foam ρ^*	338.35 ± 0.007 kg/m^3
Volume fraction of the foam ρ^*/ρ_s	0.130
Young's modulus of the cell wall material aluminium E_s	70 GPa (assumed)
Poisson's ratio of aluminium ν_s	0.33 (assumed)
Density of aluminium ρ_s	2700 kg/m^3 (assumed)

Table 6.1: Geometric data for the two samples of rectangular bars made of Alulight.

avoided by taking proper care while hitting the sample. Each impulse and its FFT were checked to avoid the effects of double impact. Further, frequency response plots which are free from noise were used for the averaging process. Since the Nyquist frequency is half the sampling frequency, the sampling frequency was chosen as 2.56 times the maximum frequency. The resolution of the spectral lines in the frequency is 0.25 to 0.5 Hz. No windowing was used in this case as the primary interest was in the FRF for the whole frequency band. Figures 6.5 and 6.6 show typical plots of the amplitude and the phase of the accelerance obtained due to the excitation at positions 1 and 2 respectively. The noise in the band of DC to the first clear resonance peak in figures 6.5 and 6.6 is attributed to the soft suspension used.

The measurements in figures 6.5 and 6.6 are driving point measurements. Note the alternating resonances and anti-resonances on the frequency axis. This is a characteristic feature of measurements when the excitation point coincides with the sensing point. The phase changes agree with the corresponding magnitude plots since we expect a phase of $+\pi$ associated with a resonance (or a pole of the transfer function) and a phase of $-\pi$ with an anti-resonance (a zero of the transfer function). The initial phase just below the first structural resonance is the accumulated phase from the internal resonances of the soft suspension.

The torsional modes are excited in addition to the bending modes when the position of making the driving point measurements is changed from the centre line on a face to an edge. This is seen when we compare the peaks in figure 6.5 with those in figure

6.6. The torsional modes that are barely visible in figure 6.5 become pronounced in figure 6.6. They are located at 973 Hz, 1708 Hz, 2511 Hz, 3407 Hz and 4260 Hz. When driving point measurements were taken at the lengthwise centre of the beam, the first and the third torsional modes were found to be missing from the response (not shown here). This is expected since these structural modes have a node at the centre of the bar. There is a mode very close to the torsional mode at 2511 Hz in figure 6.6. This mode was confirmed to be the fundamental axial mode. This was identified by making a driving point measurement when excitation and measurement degrees-of-freedom are axial degrees-of-freedom at the ends. FRFs for such excitation are shown in figures 6.7 and 6.8. Figure 6.8 is an average of 15 FRFs shown in figure 6.7. The fundamental peak is found at 2495 Hz. An average FRF for the axial excitation of a solid aluminum sample is shown in figure 6.9. When figure 6.8 is compared with figure 6.9, we note that the frequencies are approximately multiples of the fundamental frequency for the solid bar whereas aluminum foam bar shows that the second, the third, the fourth etc. modes are at frequencies less than double, three times or four times the fundamental frequency. The less pronounced but clearly present modes at frequencies below the fundamental axial mode in figure 6.8 are the bending and the torsional modes.

§6.3.1 Extraction of elastic modulii from experimentally measured natural frequency data

Once the types of modes in a measured FRF has been identified (e.g. bending, torsional or axial), the elastic modulii can be determined by using the frequency equation for the relevant mode type. The bending modes yield the Young's modulus using the formula

$$E^* = \omega_r^2 (L/c_r)^4 \rho^* A/I \tag{6.1}$$

where, c_r takes the values of 4.73, 7.853, 10.996, 14.137, 17.279, ..., $(2r+1)\pi/2$ [8]. Note that the value of E^* as calculated from above will depend on the mode number r in the bending series. If the beam were infinitesimally thin so that shear correction and rotary inertia are negligible, this value will be identical for all the modes (within the limits of errors in the experimentation). However, any systematic departure from a constant value can be attributed to two factors: (i) that the beam does not behave as an ideal Euler-Bernoulli beam, and (ii) that the aluminium foam sample does not behave as a continuum. To distinguish these two factors, and to understand the effect of the latter, the strategy of comparing experiments with experiments were employed. When samples made of solid non-porous material are tested in the laboratory, any departure from a

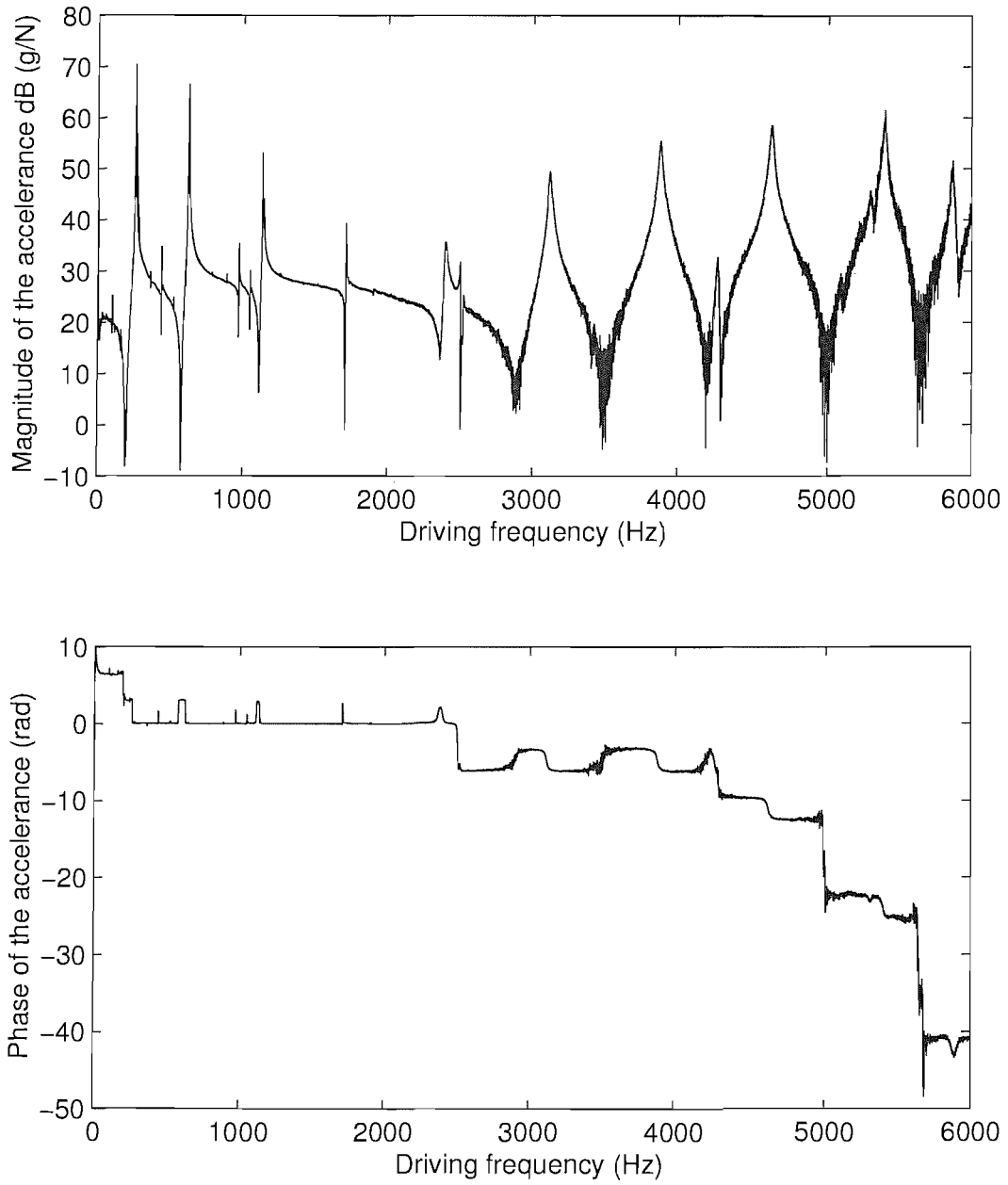

Figure 6.5: The magnitude and the phase of the accelerance FRF for the driving point excitation at position 1. The resonances and the anti-resonances are observed. The noise before the first resonance peak is mainly due to the soft suspension.

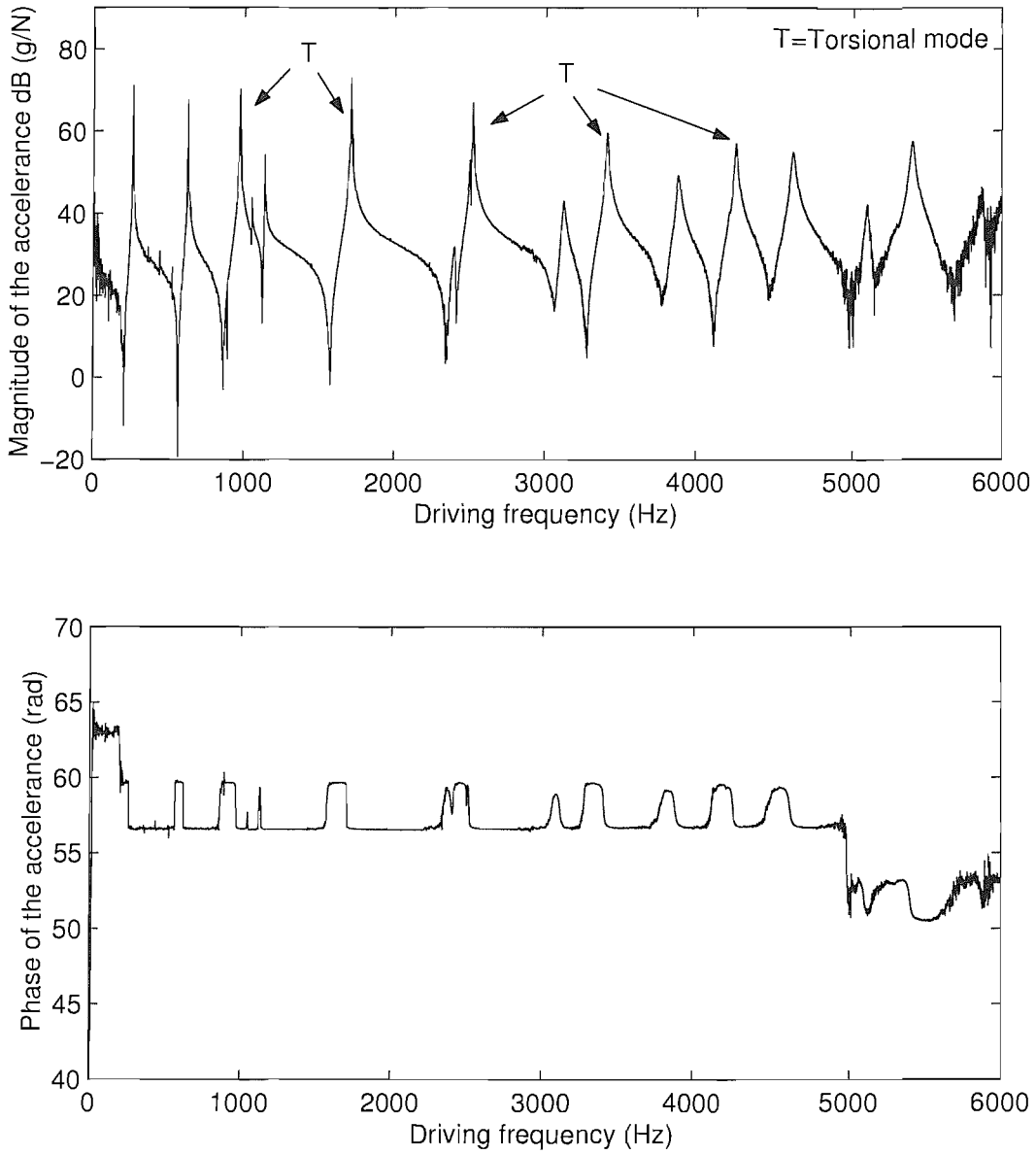

Figure 6.6: Driving point FRF when the beam is excited at position 2 instead of 1. The torsional modes which were not clear in the previous figure are distinct now. The first five peaks are found to be at 973 Hz, 1708 Hz, 2511 Hz, 3407 Hz and 4260 Hz respectively.

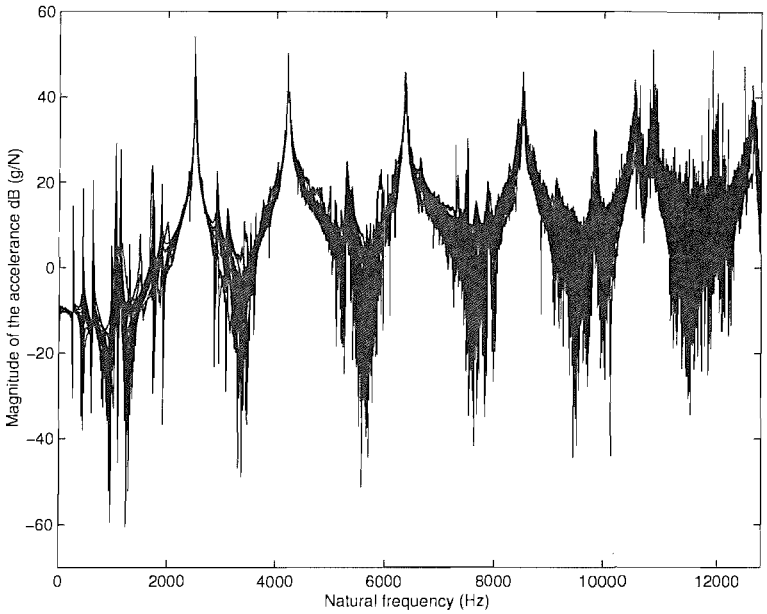

Figure 6.7: Fifteen driving point FRFs for the axial excitation, superimposed on each other.

constant value of the experimentally estimated values of the Young's modulus indicates the differences in modelling using a simple formula such as (6.1). These differences approximately depend on the geometry (e.g. thick beams require greater care in modelling) and the mode number (since the higher the mode number, the smaller the characteristic length in the axial direction rendering the same beam effectively thicker at high mode numbers). When the external dimensions of the aluminium foam samples are matched with those of a solid sample, the difference in the trend for modal frequencies and elastic constants determined therefrom will be due to the second factor mentioned above i.e. due to the porous nature of the matter being tested. The results in this section are presented with this general philosophy.

On the lines of equation (6.1), the Young's modulus can be calculated from an axial vibration mode using the formula

$$E^* = \omega_r^2 (L/c_r)^4 \rho^* \tag{6.2}$$

where, r is the mode number in the axial vibration series. c_r takes the value $r\pi$ for the r-th mode. Apart from the bending and axial vibration modes, the most commonly encountered mode type for a bar is torsional. Since these natural frequencies depend on the shear modulus, the (effective) shear modulus of the material can be calculated from

$$G^* = \frac{\omega_r^2 L^2 \rho^* I_p}{c_r^2 J} \tag{6.3}$$

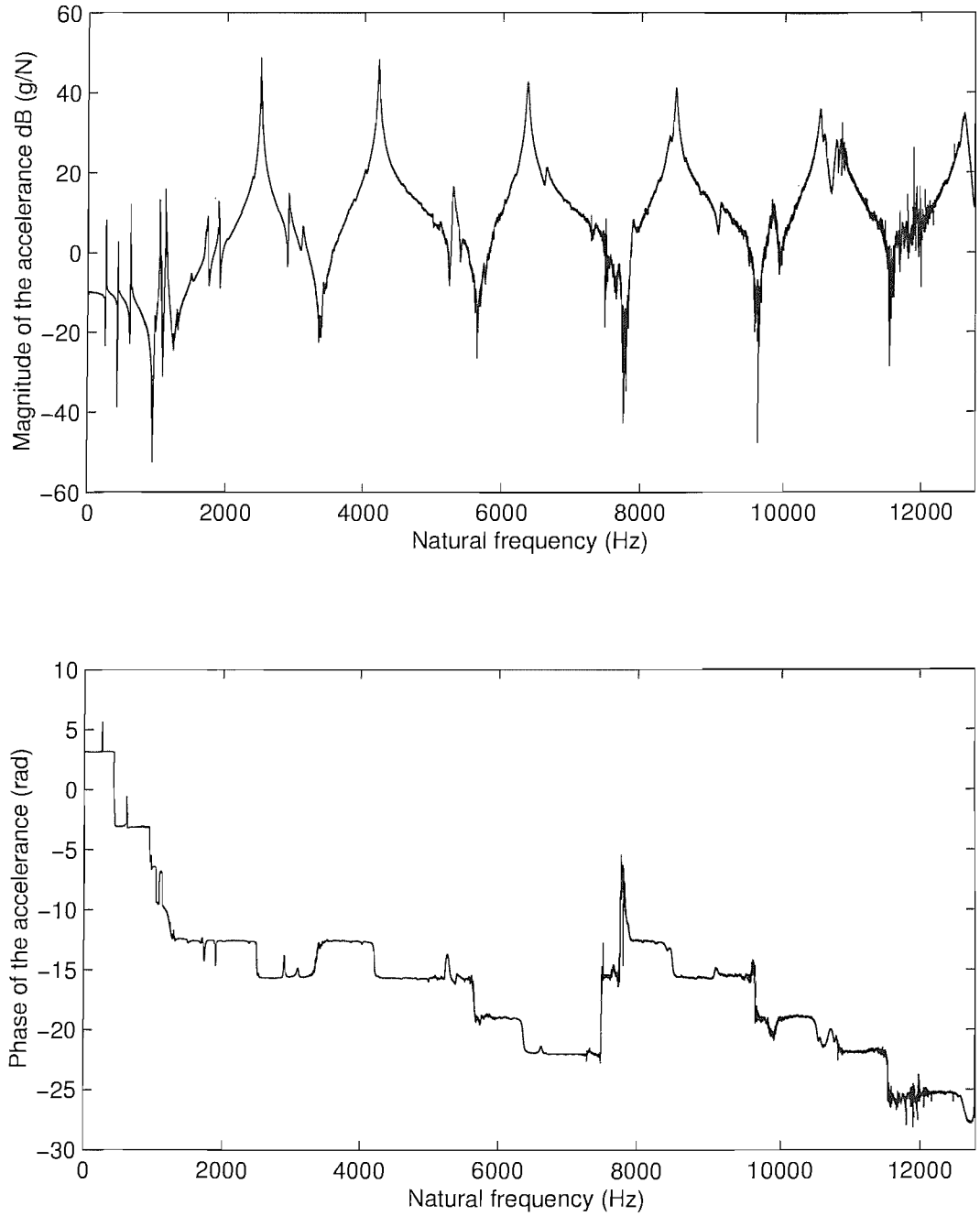

Figure 6.8: The average FRF of the fifteen FRFs for the axial excitation shown in figure 6.7. Six resonance peaks associated with the axial modes are pronounced now.

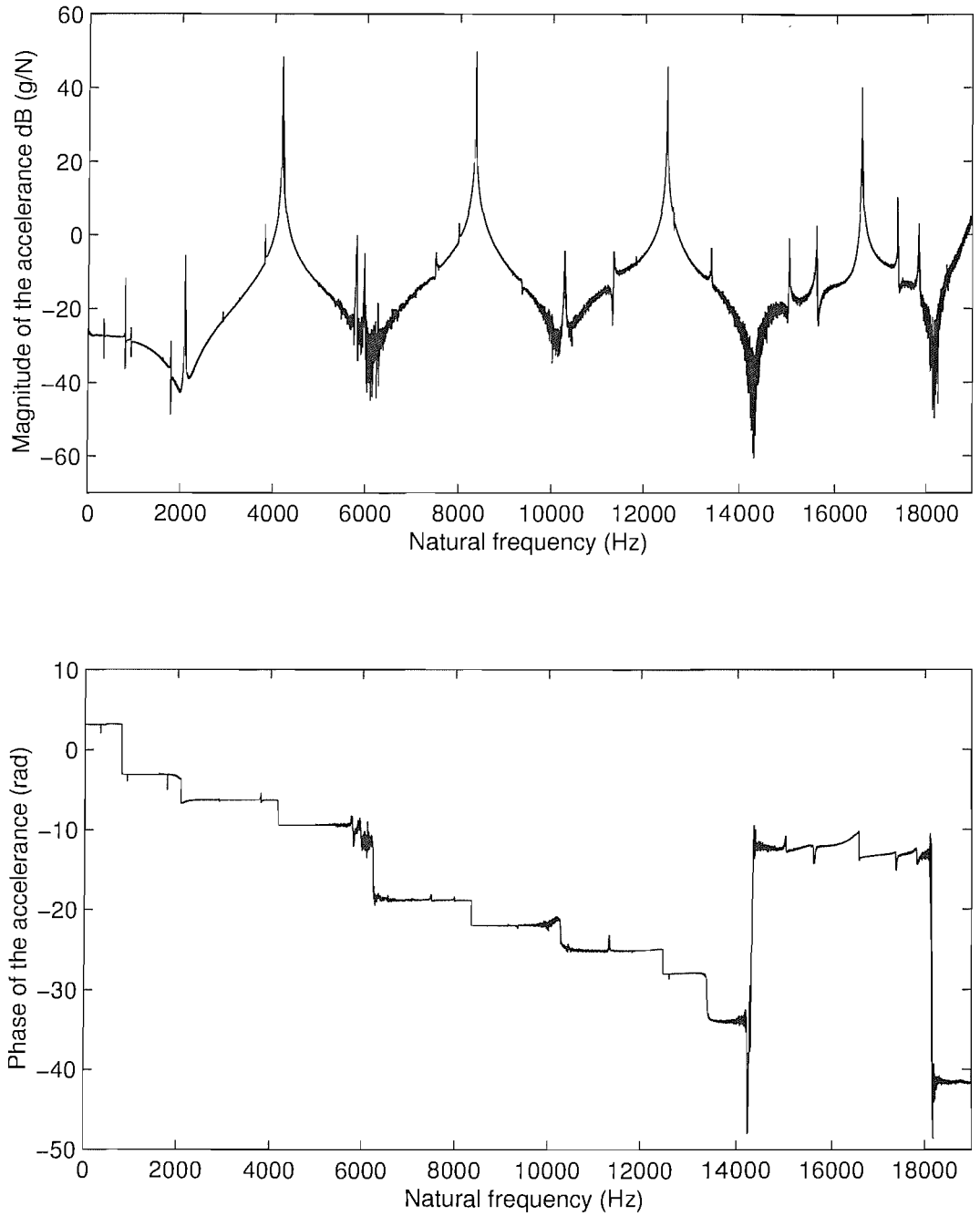

Figure 6.9: An average FRF for the axial excitation of a solid aluminium rectangular bar. The sample has the same external dimensions as those of the metal foam sample.

where, ω_r is the r-th torsional frequency, I_p and J are the polar second moment of area and the torsional constant of the cross-section respectively. c_r takes the value $r\pi$ for the r-th mode. This formula ignores warping, and this effect can be eliminated by comparing the mode number dependent values when (6.3) is employed to the torsional modes of a bar of solid material.

The value of the Poisson's ratio can be calculated by making use of the experimentally determined values of the Young's modulus and the shear modulus

$$\nu^* = \frac{1}{2}\frac{E^*}{G^*} - 1. \tag{6.4}$$

The bounds on the relative error in determining the values of E^*, G^* and ν^* are given by

$$\left|\frac{dE^*}{E^*}\right| \leq 2\left|\frac{d\omega}{\omega}\right| + 2\left|\frac{dL}{L}\right| + \left|\frac{d\rho^*}{\rho^*}\right|, \qquad \left|\frac{dG^*}{G^*}\right| \leq 2\left|\frac{d\omega}{\omega}\right| + 2\left|\frac{dL}{L}\right| + \left|\frac{d\rho^*}{\rho^*}\right| + \left|\frac{dI_p}{I_p}\right| + \left|\frac{dJ}{J}\right|. \tag{6.5}$$

and

$$\left|\frac{d\nu^*}{\nu^*}\right| \leq \left|\frac{dE^*}{E^*}\right| + \left|\frac{dG^*}{G^*}\right|. \tag{6.6}$$

The value extracted on the basis of the first axial mode and the first torsional vibration mode are tabulated in table 6.2. These values are based on the first axial frequency equal to 2495 Hz for sample 1, 2423 Hz for sample 2 and the first torsional frequency equal to 973 Hz for sample 1 and 937.5 Hz for sample 2. In the same table, estimates available in the literature (section 1.2.3) for modulii of foams are presented for comparison. These estimates account for volume fraction only.

Elastic Constants	Experiment Sample 1	Experiment Sample 2	Christensen [12]	Gibson et al. [35]	Simone et al. [91]
E^*/E_s	0.0516 ± 0.0002	0.0461 ± 0.0002	0.083	0.052	0.0458
ν^*	0.39 ± 0.058	0.40 ± 0.058	0.249	0.33	–

Table 6.2: Comparisons of the experimental results with theoretical predictions.

§6.3.2 Degradation of the effective elastic modulii of metallic foams with mode number

The modal series provides a set of natural frequencies given the geometry and the properties. For slender geometries such as a bar, the ratio of frequencies in this series is independent of the material properties. Therefore, the effect of porosity on the modal series can be effectively studied by considering two different samples, one made of porous metal and another made of solid metal. If the external dimensions are the same, then

any deviation in the modal series normalised with respect to the fundamental can be attributed to the porosity.

The strategy of testing beams made out of metal foams along with identical beams of solid material has the advantage that any higher order effects due to Timoshenko shear correction or rotary inertia or, possibly, three dimensional effects are accounted for. Therefore, we do not have to make corrections by the use of a sophisticated theory; instead results from one set of experiments can be compared with those from another set of experiments. To make sure that the variability of microstructure does not affect the generic conclusions about porosity related behaviour, two samples of metal foam were tested.

The first ten flexural frequencies of the beam made of solid aluminium as well as those made of metal foam are presented in the top half of figure 6.10. For each sample, the frequencies have been normalised with respect to the experimentally measured fundamental structural frequency of the sample. In this way, all the normalised frequencies have the fundamental as unity and the higher modes show the ratio with respect to this value. The plot, therefore, shows a relative separation of modes on the frequency scale for solid matter as well as porous matter having the same external dimensions. If the effective medium theory were valid for the entire range of frequencies, we would expect that the three trends to be close to each other within the limits of experimental errors. On the contrary, we note a systematic departure from the trend for the solid bar. In both cases of porous metal, the higher modes show a progressive softening. The plot also indicates that deviation in modal separation cannot be attributed to the randomness in porosity because this would have resulted in random deviations on either side of the trend for the homogeneous solid. The observation that the deviations are small for low mode numbers and *systematically* increase with increase in the mode number indicates that the non-continuum behaviour is pronounced at higher frequencies. This is in agreement with our observations on two-dimensional simple beams models in Chapter 2 and Chapter 3. A possible explanation is the existence of additional rotational freedom in case of cellular matter: traditional elasticity does not account for this degree of freedom. Therefore, the experimental as well as numerical observations suggest the cellular media may be modelled as Cosserat continua.

The breakdown of the effective medium theory for higher modes can be presented by calculating effective Young's modulus for different resonant modes. This calculation is summarised in the bottom half of figure 6.10. If we had an infinitesimally thin rod,

an application of the Euler-Bernoulli beam bending formula would extract a value of Young's modulus that is independent of mode number. Using the normalisation with respect to the value of the fundamental frequency, this trend will be seen as a horizontal line staying at the value of unity. When finite sized solid bars are tested in the laboratory but thin beam formula is used (admittedly inappropriately) to calculate the effective Young's modulus, we would obtain a mode number dependent value for the Young's modulus. The experimentally obtained values of Young's modulus for the solid aluminium bar obtained in this manner are shown in figure (6.10) using the diamond markers. This mode number dependent value shows that there is a progressing softening with respect to the Euler-Bernoulli theory which can be attributed to the shear correction, rotary inertia, and other higher order effects. Experimentally measured values for Alulight beams (shown using circles and dots for the two samples) exhibit additional flexibility. The difference between the values for the solid beam and that for the metal foam beam is about 20% for the second mode. We attribute this deviation to the porosity of the material. The relative reduction in the values of Young's modulus is more pronounced for higher mode numbers.

The free-free torsional vibration frequencies of slender rods are in the ratio 1:2:3:4 etc. This is closely demonstrated by the experimentally measured modal frequencies of the solid aluminium bar shown using diamond markers in figure 6.11 (the top figure). The modal frequencies have been normalised with respect to the fundamental so that all the graphs start at unity for mode number 1. The shear modes calculated from these modal frequencies is plotted against the mode number in the bottom part of figure 6.11. Any departure from the diamond marker is due to the cellular nature of metallic foams. Note that both the samples show a reduced value of the shear modulus at higher mode numbers compared to the value derived from the fundamental natural frequency.

The natural frequencies normalised with respect to the fundamental frequency for axial vibration are shown in the top figure of 6.12. The experimentally measured points (shown using the diamond markers) show a ratio close to 1:2:3:4– the expected ratio for slender rods. In contrast, the points corresponding to the metallic foam samples fall below the diamond markers consistently. The same trend is observed for the dependence of the effective Young's modulus on the mode number (bottom figure in 6.12).

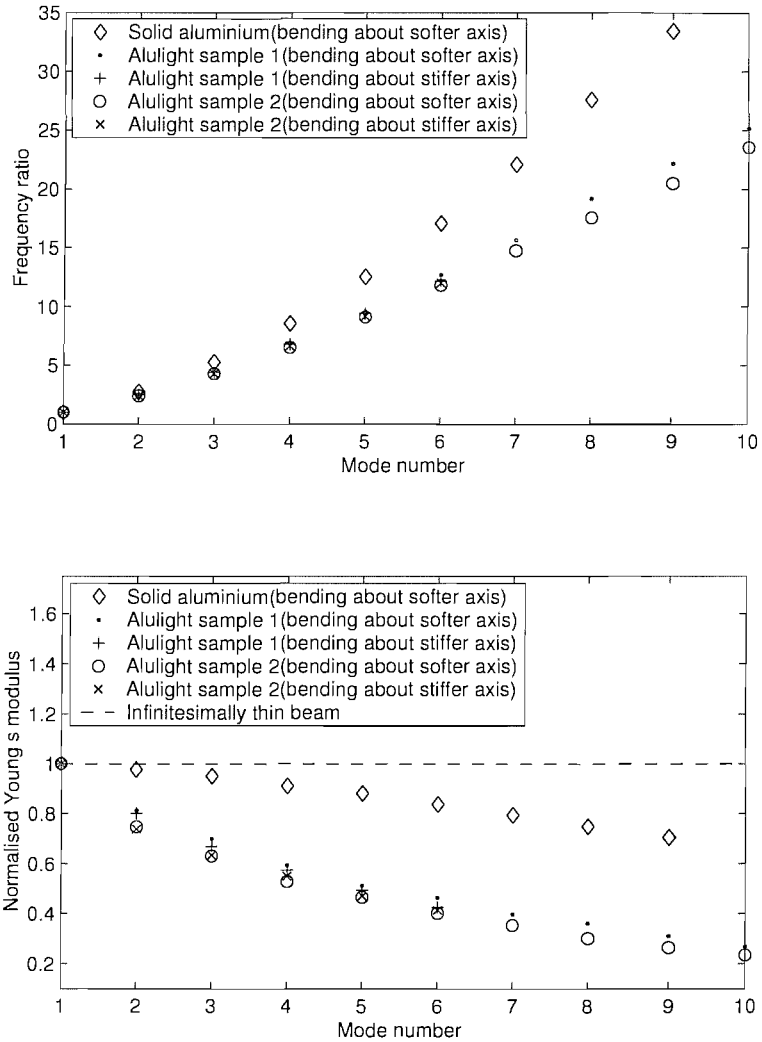

Figure 6.10: The top figure shows the bending frequencies of two Alulight samples (about both the axes) and aluminium plotted against the mode number. The frequencies are normalised with respect to the fundamental frequency of the respective series.

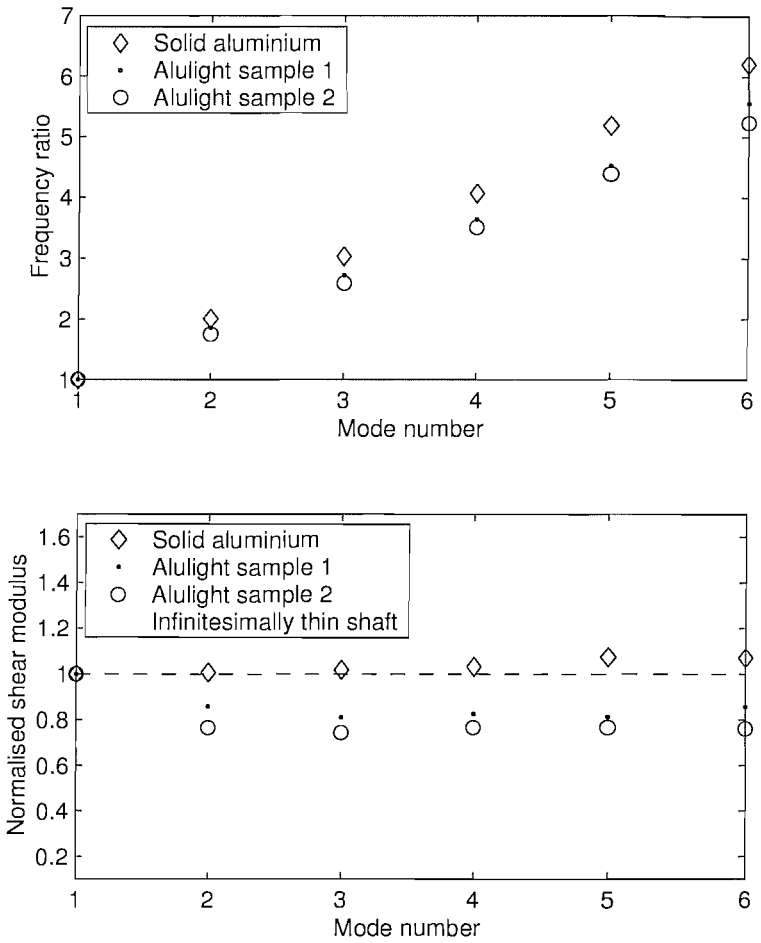

Figure 6.11: Comparisons of the torsional frequencies and the shear modulus with mode number for the Alulight foam and the solid. The solid shows little stiffening, whereas the two foam samples show reduction in the shear modulus.

§6.4 Conclusions

An experimental study on the vibration of bars of rectangular cross-section made of aluminium foams was undertaken. Vibration modes in axial motion, bending and torsion were identified to calculate the effective medium properties (the Young's modulus and the Poisson's ratio of the material).

The dependence of the effective Young's modulus on the mode number was experimentally examined. It was observed that this variation has a systematic trend that the effective modulus for the higher modes shows a relatively lower value than that for the fundamental frequency. The variation is gradual for bending modes whereas for the axial modes, the values are very different for the first two modes, but mode to mode difference is less pronounced beyond the second mode. To account for the effects associated with the finite-sizedness of the experimental sample and, therefore, to account

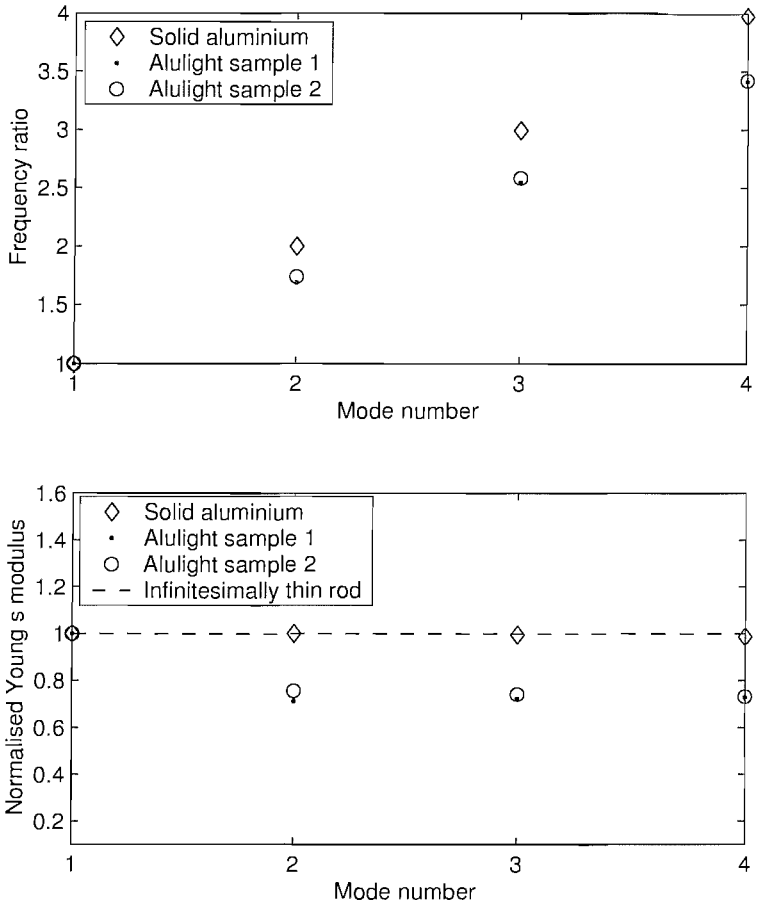

Figure 6.12: The plot of the frequency ratio and the the Young's modulus for the axial modes.

for the differences at the higher mode numbers because of the use of a simple beam or shaft formula, all the metallic foam modulii were compared with the modulii obtained from experiments on solid bars of the same external dimensions. In all the cases, it was observed that the Young's modulus for metallic foam samples shows relatively lower values at higher mode numbers compared to their solid counterparts.

The progressive softening of the Young's modulus with mode number was a general feature that was observed in many numerical simulations in Chapter 3. Therefore the experimental evidence supports this observation and suggests that the mode number dependence is probably due to the porous nature of the material. A likely reason is the presence of rotation related energy that classical continuum does not possess but the generalised Cosserat continuum does. The rotation is probably due to the rotation of joints which is perhaps unimportant for the fundamental frequency but gains importance at higher mode numbers.

The general observation in this chapter and earlier in the thesis that a constant value

of Young's modulus is not applicable for all the modes of vibration has important implications to the structural dynamics of cellular material. It clearly suggests that effective medium theories are inappropriate for high frequency vibration of cellular matter.

Chapter 7

Conclusions and future work

A summary of the conclusions appeared at the end of each chapter is presented now. This is followed by a section on the possible future work.

§7.1 Concluding remarks

The validity of the effective medium theories was examined numerically when applied to statics and dynamics of cellular beams. Beams made of hexagons and triangles were considered due to the availability of the closed form expressions of their effective Young's modulii. It was found that the value of the Young's modulus, derived for an infinite lattice under macroscopic tension-compression, can be used for bending at the bulk level when the overall depth in the transverse direction is much greater than the cell size. The first few natural frequencies of a cellular beam can be predicted using the effective medium calculations based on Euler-Bernoulli's beam theory. When Timoshenko's shear correction was used, the natural frequencies were even more accurate than the Euler-Bernoulli based calculations. For low frequencies, the overall mode shapes of the cellular structure resemble to those of a homogeneous continuum. For orthotropic beams, effective medium calculations using the value of Young's modulus in the axial direction yields more accurate results than using the value in the transverse direction.

The effective medium theory will be equally applicable for real three dimensional beams made of hexagonal foams, triangular foams etc. For such real structures, imperfections can affect the macroscopic elastic properties considerably. Hence, utmost care must be taken while using the effective properties. Detailed modelling and analysis may be preferred for irregular foams having a number of localised variations in the shape and size of cells.

The statistics of the modal spacing and the modal density for the cellular beams were compared with those of a plane stress problem whose Young's modulus is chosen to match the fundamental frequency of the cellular beam. Three regions of modal spacing were identified. It was found that the effective medium theory breaks down in regime 2 when the wavelength approaches the depth of the beam. For all the cellular topologies studied here, the modal density gradually increases as compared to that of a continuum. This rise is perhaps attributed to the porosity of the cellular medium. In this regime, various topologies start exhibiting features intrinsic to them. For example, structure made of square cells show the presence of thickness-shear modes.

As the wavelength approaches the cell size, the cell walls exhibit local resonance. In this frequency range, the presence of a number of cell walls resonating together causes an abrupt increase in the modal density. This sudden rise in the modal density is most distinct in the case of the triangles as each cell wall behaves as an independent member, whereas coupling between the cell walls in the other topologies affect the sharp rise. In the case of the irregular cells, the modal separation first decreases and then increases. The decrease is attributed to the presence of boundary cell walls. It was shown that for a triangular network, the deformation mechanism of a cell wall changes from axial to bending at the first resonant frequency. An approximate method to estimate of the cell wall resonant frequency for the triangular lattice was presented. However, the calculation of the first resonant frequency is not that straightforward for other topologies, because the deformations of the cell walls are primarily bending dominated for all mode numbers. Further, there are difficulties in simulating the end conditions of the cell walls embedded in a lattice.

A large eigenvalue problem needs to be solved for the free vibration calculations of cellular structures, even when only the first few frequencies are required. A method was developed to save computations by avoiding the solution of the full scale eigenproblem. The so-called continuum modes were used as the basis modes for the method. It was found that the Rayleigh's variational principle fails to predict the correct frequencies even when the assumed modes were very close to true modes. The reasons for this failure was traced. A sensitivity analysis was carried out to show that the presence of small mode components associated with exceptionally high frequencies can corrupt the modes. Inverse power iterations were used to eliminate these unwanted frequency components successfully. Two structural examples were given to illustrate the working of the method. Substantial computational saving without significant loss of accuracy

was reported.

The method based on the continuum modes was extended to frequency response calculations. Illustrative examples were presented. The damping ratios were accurately predicted by the reduced order model. While an overall good agreement with the full scale calculations was observed, it is admitted that the method is not suitable for moderately high frequency vibration calculations.

The Young's modulus and the Poisson's ratio of Alulight^{TM} were obtained experimentally by measuring the fundamental frequencies associated with the axial and the torsional modes. It was found that the Young's modulus as calculated from higher modes is always less than that extracted on the basis of the fundamental natural frequency. This trend was common to all the mode types but was most pronounced for bending modes. The above conclusions account for the limitations posed by one-dimensional theories– the experimentally observed softening with mode number is much less for homogeneous bars of the same external dimensions.

A general conclusion that arises out of this work is that effective medium theories are approximately applicable to low frequency dynamics. They become increasingly inappropriate to capture the behaviour with increase in the mode number. This affords new challenges to high frequency dynamics and noise transmission.

The main contributions of this thesis are as follows:

- Beams made of cellular material can be replaced by an appropriate homogeneous continuum for static bending as well as for low frequency dynamics (Chapter 2).

- With the increase in the mode number, a cellular beam ceases to behave as a continuum. Then, the dynamics of a cellular beam becomes topology-dependent, which is reflected by presence of a variety types of localised modes and a varying modal separation as well (Chapter 3).

- A method is proposed for the approximate free vibration calculations of the cellular structures using assumed modes based on a continuum to achieve computational economy with good accuracy (Chapter 4).

- A sensitivity analysis to show that an approximation based on the Rayleigh's variational principle can yield inaccurate results due to the presence of very small modal contributions associated with very high frequency in the trial vector, despite the trial vector being very close to the exact eigenvector. The use of inverse power iterations to pre-condition the assumed modes was successfully employed (Chapter

4).

- The extension of the proposed model order reduction method to estimate the frequency response (Chapter 5).
- Experimental investigation of the departure of the continuum behaviour of metallic foams by a carefully designed experiment (Chapter 6).

§7.2 Future work

There are several aspects of the structural dynamics of cellular media that need further study. They are itemised below:

- The modelling of foam-filled sandwich constructions is a practical problem. The structural dynamics of these constructions is a problem closely related to the main theme of this work.
- It would be interesting to check if the general conclusions drawn from two dimensional models presented in this dissertation hold for three dimensional models too.
- The present work indicated the sensitivity of the cellular topologies on the dynamic behaviour of the cellular materials. The dependence of the geometrical parameters such as thickness of the cell walls was also presented. As the next step, the effect of the shape and the size of a cell on the overall dynamics can be studied. This will be useful in identifying a suitable foam topology, and then optimising its properties e.g. mass, stiffness etc., as required for specific applications.
- Experimental measurements in the high frequency regimes could be undertaken. Asymptotic formula for modal density as a function of the real part of mobility can perhaps be used for the purpose.
- The issue of computational economy for moderately high frequency is unresolved. Perhaps the Statistical Energy Analysis (SEA) is a suitable tool for problems such as noise transmission.
- Instead of the proportional damping, hysteretic damping of the cell wall material can be included by evaluating the strain and the associated stress in the cell wall. In that case, the stiffness matrix will be complex. The limitation is that the equation of motion can only be written and solved in the frequency domain.

- Experimental studies on damping mechanisms in cellular solids are very limited.

References

[1] Abd El-Sayed, Jones F. K. and Burgess I. W. (1979), A theoretical approach to the deformation of honeycomb based composite materials, Composites 10, 209-214.

[2] ABAQUS User's Manual (2000), Version 6.1, Hibbit, Karlsson & Sorensen Inc.

[3] Andrews E. W. and Gibson L. J. (2001), The influence of cracks, notches and holes on the tensile strength of cellular solids, Acta Mater. 49, 2975-2979.

[4] ASTM (1994) Standard test method for dynamic Young's modulus, shear modulus, and Poisson's ratio for advanced Ceramics by impulse excitation method of vibration, Annual Book of ASTM standards 15.02 Designation C 1259, 1-9.

[5] Baker W. E., Togami T. C., Weydert J. C. (1998), Static and dynamic properties of high-density metal honeycombs, Int. J. of Impact Engg. 21, 149-163.

[6] Banhart J., Baumeister J. and Weber M. (1996), Damping properties of aluminium foams, Mater. Sci. Eng. A 205, 221-228.

[7] Bazant Z. P. and Christensen M. (1972), Analogy between micropolar continuum and grid frameworks under initial stress, Int. J. Solids Struct. 8, 327-346.

[8] Blevins R. D. (1995), Formulas for natural frequency and mode shape, Krieger Publishing, Melbourne, FL, 2nd Ed.

[9] Chang C. C. and Ebcioglu I. K. (1961), Effect of cell geometry on the shear modulus and on density of sandwich panel cores, Trans. ASME D Dec, 513-518.

[10] Choi J. B. and Lakes R. S. (1995), Analysis of elastic modulus of conventional foams and of re-entrant foam materials with negative Poisson's Ratio, Int. J. Mech. Sci. 37, 51-59.

[11] Christensen R. M. (2000), Mechanics of cellular and other low-density materials, Int. J. Solids Struct. 37, 93-104.

[12] Christensen R. M. (1986), Mechanics of low density materials, J. Mech. Phys. Solids 34(6), 563-578.

[13] Chen C., Lu T. J. and Fleck N. A. (1999), Effect of imperfections on the yielding of two dimensional foams, J. Mech. Phys. Solids 47, 2235-2272.

[14] Chen C., Lu T. J. and Fleck N. A. (2001), Effect of inclusions and holes on the stiffness and strength of honeycombs, Int. J. Mech. Sci. 43, 487-504.

[15] Chung J. and Waas A. M. (2000), The in-plane elastic properties of circular cell and elliptical cell honeycombs, Acta Mech. 144, 29-42.

[16] Cosserat E. F. (1909), Theorie des Corps Deformables, Paris.

[17] Cowper G. R. (1966), The shear coefficient in Timoshenko's beam theory, J. Appl. Mech., 335-340.

[18] Cowin S. C. (1985), The relationship between the elasticity tensor and the fabric tensor, Mech. Mater. 4, 137-147.

[19] Dement'ev A. G. and Tarakanov O. G. (1970), Effects of cellular structure on the mechanical properties of platic foams, Mekhanika Polimerov 4, 594-602; translation Pol. Mech. 6, 519-525.

[20] Dement'ev A. G. and Tarakanov O. G. (1970), Model analysis of the cellular structure of plastic foams of the polyurethane type, Mekhanika Polimerov 5, 859-865; translation Pol. Mech. 6, 744-749.

[21] Deshpande V. S., Ashby M. F. and Fleck N. A. (2001), Foam topology bending versus stretching dominated architectures, Act. Mat. 49(6), 1035-1040.

[22] Egli E. (1972), Indentation of foamed plastic, J. Cell. Plast. 8, 245.

[23] Evans A. G., Hutchinson, J. W. and Ashby M. F. (1998), Cellular metals, Current Opinion in Solid State & Materials Science 3, 288-303.

[24] Evans K. E. (1991), Molecular network design, Nature 53, 124.

[25] Evans K. E. (1992), Design of doubly curved sandwich panels, Comp. & Struct. 17, 95-111.

[26] Easterling K. E., Harryson R., Gibson L. J. and Ashby M. F. (1982), On the mechanics of balsa and other woods, Proc. R. Soc. London A383, 31-41.

[27] Eringen A. C. (1999), Microcontinuum field theories, I. Foundations and solids, Springer, New York, 1968.

[28] Ewins D. J. (2000), Modal Testing, Theory, Practice and Applications, Baldock Herts, Research Studies Press, 2nd ed.

[29] Fox R. L. and Kapoor M. P.,(1968), Rate of change of eigenvalues and eigenvectors, AIAA J 6, 2426-2429.

[30] Friswell M. I., Garvey S. D. and Penny J. E. T. (1995), Model reduction using dynamic and iterated IRS techniques, J. Sound and Vibration 186(2), 311-323.

[31] Garboczi E. J. and Day A. R. (1995), An algorithm for computing the effective linear elastic properties of heterogeneous materials : 3-D results for composites with equal phase Poisson ratios, J. Mech. Phys. Solids 43, 1349-1362.

[32] Gent A. N. and Thomas A. G. (1959), The deformation of foamed elastic materials, J. App. Polymer Sci. 1, 107-113.

[33] Gibson L. J., Ashby M. F., Schajer G. S. and Robertson C. I. (1982), The mechanics of two dimensional cellular materials, Proc. R. Soc. London A382, 25-42.

[34] Gibson L. J., Easterling K. E. and Ashby M. F. (1981), The structure and mechanics of cork, Proc. R. Soc. London A377, 99-117.

[35] Gibson L. J. and Ashby M. F. (1997), Cellular Solids : Structure and Properties, Cambridge, UK : Cambridge Univ.Press, 2nd ed.

[36] Gibson L. J. and Ashby M. F. (1982), The mechanics of three dimensional cellular materials, Proc. R. Soc. London A382, 43-59.

[37] Gibson L. J. (2000), Mechanical Behaviour of Metallic Foams, Annu. Rev. of Mater. Sci. 30, 191-227.

[38] Gibson L. J. (1981), The elastic and plastic behaviour of cellular materials, PhD thesis, Cambridge University.

[39] Grediac M. (1993), A finite element study of the transverse shear in honeycomb cores, Int. J. Solids Struct. 30, 1777-1788.

[40] Grenestedt J. L. (1998), Influence of wavy perfections in cell walls on elastic stiffness of cellular solids, J. Mech. Phys. Solids 46, 29-50.

[41] Grenestedt J. L. (1999), Effective elastic behaviour of some models for 'perfect' cellular solids, Int. J. Solids Struct. 36(10), 1471-1501.

[42] Grenestedt J. L. and Tanaka K. (1998), Influence of cell shape variations on elastic stiffness of closed cell cellular solids, Scripta Mat. 40(1), 71-77.

[43] Grenestedt J. L. and Bassinet F. (2000), Influence of cell wall thickness variations on elastic stiffness of closed cell cellular solids, Int. J. Mech. Sci. 42(7), 1327-1338.

[44] Gulati S. T. (1975), Effects of cell geometry on thermal shock resistance of catalytic monoliths, paper 750171, Automotive Engineering Congress and Exhibition Society of Automotive Engineers, Detroit, Michigan, 1-9.

[45] Guo X. E. and Gibson L. J. (1999), Behaviour of intact and damaged honeycombs: a finite element study, Int. J. Mech. Sci. 41, 85-105.

[46] Guyan R. J. (1965), Reduction of stiffness and mass matrices, AIAA J 3(2), 380.

[47] Han S. M., Benaroya H. and Wei T. (1999), Dynamics of transversely vibrating beams using four engineering theories, J. Sound and Vibration 225(5), 935-988.

[48] Han F. S., Zhu Z. G. and Liu C. S. (1997), Nonlinear internal friction character of foamed aluminum, Scripta Mater. 37(9), 1441-1447.

[49] Harris C. M., Shock and Vibration Handbook, McGraw-Hill Book Company, 3rd ed., 1988.

[50] Hashin Z. and Shtrikman S. (1963), A Variational approach to the theory of elastic behaviour of multiphase materials, J. Mech. Phys. Solids 11, 127-140.

[51] Hilyard N. C. (1982), Mechanics of cellular plastics, Applied Science, Barking.

[52] Hohe J. and Becker W. (2000), A mechanical model for two dimensional cellular sandwich cores with general geometry, Comput. Mater. Sci. 19, 108-115.

[53] Hohe J. and Becker W. (2001), An energetic homogenisation procedure for the elastic properties of general sandwich cores, Compos. B 32, 185-197.

[54] Hohe J. and Becker W. (2002), Effective stress-strain relations for two-dimensional sandwich cores: Homogenisation, material models and properties, ASME Appl. Mech. Rev. 55(1), 61-87.

[55] Hollister S. J. and Kikuchi N. (1994), Homogenisation theory and digital imaging: A basis for studying the mechanics and design principles of bone tissue, Biotech Bioengineering 43, 586-596.

[56] Hunt H. E. M. (1993), The mechanical strength of ceramic honeycomb monoliths as determined by simple experiments, Trans. Inst. Chem. Eng. 71A, 257-266.

[57] Hyun S. and Torquato S. (2000), Effective elastic and transport properties of regular honeycombs for all densities, J. Mat. Res. 15(9), 1985-1993.

[58] Kahle E. and Woodhouse J. (1994), The influence of cell geometry on the elasticity of softwood, J. Mater. Sci. 29, 1250-1259.

[59] Kanakkant S. V. (1973), Mechanical anisotropy of open cell foams, J. Cell. Plast. 9, 50-53.

[60] Kelsey S., Gellatly R. A. and Clark B. W. (1958), The shear modulus of foil honeycomb core, Aircraft Engineering 30, 294-302.

[61] Lord Kelvin (Thompson W.) (1887), On the division of space with minimum partitional area, Phil. Mag. 24, 503-514.

[62] Ko W. L. (1965), Deformations of foamed elastomers, J. Cell. Plast. 1, 45-50.

[63] Lakes R. S. (1987), Foam structures with negative Poisson's ratio, Science 235, 1038-1040.

[64] Lakes R. S. (1991), Deformation mechanisms in negative Poisson's ratio materials:structural aspects, J. Mat. Sci. 26, 2287-2292.

[65] Lakes R. S. (1983), Size effects and micromechanics of a porous solid, J. Mat. Sci. 18, 2572-2580.

[66] Chen C. P. and Lakes R. S. (1996), Micromechanical analysis of dynamic behaviour of conventional and negative Poisson's ratio foams, J. Engg. Mater. Tech. (ASME) 118, 285-288.

[67] Lederman J. M. (1971), The prediction of the tensile properties of foams, J. App. Polymer Sci. 15, 693-703.

[68] Li K., Gao X. L. and Roy A. K. (2003), Micromechanics model for three dimensional open cell foams using a tetrakaidecahedral unit cell and Castigliano's second theorem, Comp. Sci. Tech. 63, 1769-1781.

[69] Liu C. S., Zhu Z. G., Han F. S. and Banhart J. (1999), Study of nonlinear properties of foamed Al, Phil. Mag. A 80(5), 1085-1092.

[70] McCullough K. Y. G., Fleck N. A. and Ashby M. F. (1999), Uni-axial stress-strain behaviour of Aluminium alloy foams, Acta Mater. 47(8), 2323-2330.

[71] Masters I. G. and Evans K. E. (1996), Models for the elastic deformation of honeycombs, Comput. Structs 35(4), 403-422.

[72] MATLAB User's Manual (1995), Version 5.3, The Mathworks, Inc.:Natick, MA.

[73] Meirovitch L. (1975), Elements of vibration analysis, McGraw-Hill Book Company, Ist ed.

[74] Menges G. and Knipschild F. (1975), Estimation of mechanical properties for rigid polyurethane foam, Polymer Eng. Sci. 15, 623-627.

[75] Nilsson E. and Nilsson A. C. (2002), Prediction and measurement of some dynamic properties of sandwich structures with honeycomb and foam cores, J. Sound and Vibration 251(3), 409-430.

[76] O'Callahan J. (1989), A procedure for an improved reduced system (IRS) model, Proceedings of the 7th International Modal Analysis Conference, Orlando, Fl, U.S.A., 1537-1543.

[77] Overacker D. W., Cuitiono A. M. and Langrana N. A. (1998), Effects of morphology and orientation on the behaviour of two-dimensional foams and application in an re-entrant anchor model, Mech. Mat. 29(1), 43-52.

[78] Overacker D. W., Cuitiono A. M. and Langrana N. A. (1998), Elastoplastic micromechanical modelling of two-dimensional irregular convex and nonconvex (re-entrant) hexagonal foams, ASME J. Appl. Mech. 65, 748-757.

[79] Patel M. R. and Finnie I. (1970), Structural features and mechanical properties of rigid cellular plastics, J. Mater. 5, 909-932.

[80] Penzien J. and Didriksson T. (1964), Effective shear modulus of honeycomb cellular structures, AIAA J 2, 531-535.

[81] Prakash O., Bichebois P., Brechet Y., Louchet F. and Embury J. D. (1996), A note on the deformation behaviour of two-dimensional model cellular structures, Phil. Mag. 73(3), 739-751.

[82] Progelhof R. C. and Throne J. L. (1979), Young's modulus of uniform density thermoplastic foams, Polymer Eng. Sci. 19, 493-499.

[83] Ramamurthy U. and Paul A. (2003), Varaiability in mechanical properties of a metal foam, Acta Mater. 52, 869-876.

[84] Roberts A. P. and Garboczi E. J. (2000), Elastic modulii of model random three dimensional closed cell cellular solids, Acta Mater. 49(2), 189-197.

[85] Roberts A. P. and Garboczi E. J. (2002), Elastic properties of model random three dimensional open cell cellular solids, J. Mech. Phys. Solids 50, 33-55.

[86] Scarpa F., Panayiotou P. and Tomlinson G. (2000), Numerical and experimental uniaxial loading on in-plane auxetic honeycombs, J. Strain Analysis 35(5), 383-388.

[87] Scarpa F. and Tomlinson G. (2000), Theoretical characteristics of the vibration of sandwich plates with in-plane negative Poisson's ratio values, J. Sound and Vibration 230(1), 45-67.

[88] Shames I. R. and Dym C. L. (1995), Energy and finite element methods in structural mechanics, Wiley International Eastern Ltd. Ist ed.

[89] Silva M. J., Hayes W. C. and Gibson L. J. (1995), The effects of non-periodic microstructure on the elastic properties of two dimensional cellular solids, Int. J. Mech. Sci. 37(11), 1161-1177.

[90] Silva M. J. and Gibson L. J. (1997), The effects of non-periodic microstructure and defects on the compressive strength of two-dimensional cellular solids, Int. J. Mech. Sci. 39(5), 549-563.

[91] Simone A. E. and Gibson L. J. (1998), Effects of solid distribution on the stiffness and strength of metallic foams, Acta Mater. 46(6), 2139-2150.

[92] Simone A. E. and Gibson L. J. (1998), The effects of cell wall curvature and corrugations on the stiffness and strength of metallic foams, Acta Mater. 46(11), 3929-3935.

[93] Simone A. E. and Gibson L. J. (1998), Aluminium foams by produced liquid state processes, Acta Mater. 46(9), 3109-3123.

[94] Spinner S. and Tefet W.E. (1961), A method for determination of mechanical resonance frequencies and for calculating elastic moduli from those frequencies, Proc. ASTM. 61, 1221.

[95] Timoshenko S. and Young D. H. (1962), Elements of strength of materials, D. Van Nostrand Company, INC, 4th ed.

[96] Torquato S., Gibiansky L. S., Silva M. J. and Gibson L. J. (1998), Effective mechanical and transport properties of cellular solids, Int. J. Mech. Sci. 40(1), 71-82.

[97] Torquato S. (1991), Random heterogeneous media: microstructure and improved bound on effective properties, Appl. Mech. Rev. 44(2), 37-76.

[98] Turner C. H. and Cowin S. C. (1987), Dependence of elastic constants of anisotropic porous material upon porosity and fabric, J. Mat. Sci. 22, 3178-3187.

[99] Van derBurg M. W., Shulmeister V., Van der Giessen E. and Marissen V. J. (1997), On the linear elastic properties of regular and random open cell foam models, J. Cell. Plast. 33, 31-54.

[100] Voigt W. (1887), Theoretische studien uber die elasticitatsverhaltnesse der krystalle, Abh Ges Wiss Gottingen.

[101] Wang X. L. and Stronge W. J. (1998), Micropolar theory for two dimensional stresses in elastic honeycomb, Proc. R. Soc. London 455, 2091-2116.

[102] Wang X. L. and Stronge W. J. (2001) Micropolar Theory for a periodic force on the edge of elastic honeycomb, Int. J. of Engg. Sci. 39, 821-850.

[103] Warren W. E. and Kraynik A. M. (1987), Foam Mechanics: The linear elastic response of two dimensional spatially periodic materials, Mech. Mat. 6, 27-37.

[104] Warren W. E. and Kraynik A. M. (1988), The linear elastic properties of open cell foams, ASME J. Appl. Mech. 55, 341-346.

[105] Warren W. E. and Kraynik A. M. (1991), The nonlinear elastic properties of open cell foams, ASME J. Appl. Mech. 59, 376-381.

[106] Warren W. E. and Kraynik A. M. (1997), Linear elastic behaviour of a low density Kelvin foam with open cells, ASME J. Appl. Mech. 64, 787-794.

[107] Kraynik A. M. and Warren W. E. (1994) The elastic behaviour of low density cellular plastics, Low density cellular plastics, Hilyard N. C. and Cunningham A. C., Chapman and Hall, London 187-225.

[108] Weaire D. and Phelan R. (1994), A counterexample to Kelvin's conjecture on minimal surfaces, Phil. Mag. Letts. 69, 107-110.

[109] Weaire D. and Phelan R. (1994), Stress and strain in liquid and solid foams, Adv. Phy. 43, 685-738.

[110] Xia Y. and Lin R. (2004), A new iterative order reduction (IOR) method for eigensolutions of large structures, Int. J. Numer. Meth. Engg. 59, 153-172.

[111] Zhu H. X., Hobdell J. R. and Windle A. H. (2001), Effects of cell irregularity on the elastic properties of 2D Voronoi honeycombs, J. Mech. Phys. Solids 49, 857-870.

[112] Zhu H. X., Knott J. F. and Mills N. J. (1997), Analysis of elastic properties of open cell foams with tetrakaidecahedral cells, J. Mech. Phys. Solids 45, 319-343.

[113] Zhu H. X., Hobdell J. R. and Windle A. H. (2001), Effects of cell irregularity on the elastic properties of open cell foams, Acta. Mater. 48, 4893-4900.

[114] Zhu H. X., Thorpe S. M. and Windle A. H. (2001), The geometrical properties of irregular two dimensional Voronoi tessellations, Phil. Mag. A 81(12), 2765-2783.